Experimental Characterization of Skin-Friction Drag Reduction on Superhydrophobic Surfaces in High-Reynolds Number Flows

by

James Warren Gose

A dissertation submitted in partial fulfillment
of the requirements for the degree of
Doctor of Philosophy
(Naval Architecture and Marine Engineering)
in The University of Michigan
2018

Doctoral Committee:

> Professor Steven L. Ceccio, Co-Chair
> Professor Marc Perlin, Co-Chair
> Professor Michael P. Schultz, United States Naval Academy
> Associate Professor Anish Tuteja

James W. Gose

jgose@umich.edu

ORCID iD: 0000-0001-6569-2376

I dedicate this work to Alli, my loving wife,

and my family whom have always believed in me.

ACKNOWLEDGEMENTS

This dissertation and body of work could not have been completed without the support of many individuals. First, I would like to think my Doctoral Committee. I want to thank my committee co-chairs, Professors Steven Ceccio and Marc Perlin. Steve and Marc, you were always willing to go the extra mile to help me in and out of the laboratory, and challenge me intellectually. To you both, thank you for helping me grow as a researcher, scholar, and individual. Additionally, I want to thank my other committee members, Professors Anish Tuteja and Michael Schultz. Anish and Mike, thank you for letting me take over your labs throughout my career, supporting my efforts with additional effort from your other mentees, and providing critical and constructive feedback when needed.

I want to thank the Naval Architecture and Marine Engineering Department staff and faculty for always being available and sympathetic to my needs as a student and blossoming researcher. Additionally, I thank the Marine Hydrodynamics Laboratory staff, past and present, for their contributions to my efforts and assisting to make

my experimental objectives possible. Moreover, I thank all of the students that have labored long hours next to me in constructing experimental apparatuses and collecting numerous data sets.

I want also to thank my family for their constant support and encouragement. Dad, mom, and Dusti, your constant presence and championing of my dreams year after year as I pursued the 'next' opportunity has kept me on an even keel. I would not have made it this far in my academic career without you.

Last but not least, I thank my wife, Allison Christine Gose, for her tireless and unwavering care and devotion to me and my goals. Alli, you were always there when I needed you most, and this is for what I am most grateful. I love you.

TABLE OF CONTENTS

LIST OF FIGURES

LIST OF TABLES

ABSTRACT

American marine vessels used more than seven billion gallons of fossil fuels in 2012, and approximately 60 to 70 percent of this fuel is expended to overcome resistance due to skin-friction. Hence, considerable efforts have been devoted to reduce skin-friction using both passive and active methods of skin-friction reduction. The efficacy and practicality of these skin-friction reduction methods has often been limited, restricting their use; therefore, the search continues for effective and economically viable means of friction drag reductions.

Superhydrophobic surfaces (SHSs) have been shown to reduce skin-friction for laminar boundary layers. It is our goal to investigate their efficacy for turbulent flows. A SHS is characterized as a low surface energy material that, when in contact with a water drop maintains high contact angle and low resistance to rolling. These attributes are ascribed to the difference in interfacial energy between the water and solid surface of the SHSs and the solid-surface interface of the SHS - a base of micro- and nano-scale features, which act to trap pockets of air in the surface. These air pockets result in a heterogeneous three-phase interface that may reduce the wetted area between the water and solid surface, and consequently, have the potential to alter the no-slip boundary condition at the water and air interface, resulting in a reduced local shear stress. Therefore, SHSs have the potential to provide a passive and potentially more attractive alternative to the traditional means of active drag reduction.

In this dissertation, we experimentally examined the viability of SHSs for skin-friction drag reduction for turbulent boundary layers (TBL). To do so, we developed

composite, sprayable SHSs that can be designed and applied to areas significantly greater than one square meter. These SHSs are mechanically robust and can withstand the extreme shear and pressure fluctuations experienced beneath turbulent boundary layers. The SHSs were spray applied to a test panel and placed in a specially designed fully-developed, turbulent flow facility designed by the author. The coefficient of friction was inferred using the streamwise pressure drop along the SHSs and velocity measurements of the mean flow through the channel. The experimental test data showed more than 50% sustained skin-friction drag savings for height-based Reynolds numbers ranging from $10,000 \leq Re_H \leq 40,000$ and friction Reynolds number ranging from $300 \leq Re_\tau \leq 1,000$. Measurements of near-zero pressure-gradient TBL flow over similar SHSs were also conducted at a U.S. Naval Academy flow facility. The TBL experiments were conducted with a free-stream speed of 1.26 m/s, corresponding to a Re_τ of 1,600. Near-wall velocity indicated that greater than 10% reduction in the total stress at the wall could be achieved.

The skin-friction measurements were coupled with a topological evaluation of the SHSs to develop insights regarding the surface characteristics relevant to the skin-friction in turbulent flows. The results showed that the skin-friction in TBLs produced by SHSs is highly dependent on the surface's roughness characteristics and resistance to wetting. More specifically, the essential SHSs characteristics were their non-dimensional roughness k^+, the presence of large, unwanted asperity features, and the areal wetted fraction ϕ_s the surface experienced at the mean pressures of the flow. These findings resulted in the development of a scaling model, along with design guidance that can be implemented for a given Reynolds number.

CHAPTER I

Introduction

The fuel used to overcome hydrodynamic resistance of marine vessels is significant. For example, in 2012, the U.S. alone used over seven billion gallons of fossil fuels to power marine vessels according to the U.S. Department of Transportation (2012). Marine fuel consumption is predicted to double between 2010 and 2030 and nearly 70% of the global shipping fuel demand is for containerships, bulk carriers, general cargo vessels, and tankers (*Argyros et al.*, 2014). Nearly 60% to 70% of this fuel will be expended to overcome skin-frictional drag on the wetted surface of vessels (*Mäkiharju et al.*, 2012). Hence, methods that can effectively reduce the friction drag on marine vessels could have enormous worldwide economic and environmental impact. Current technologies, such as riblet, polymer, or air-layer drag reduction have all been considered for hydrodynamic drag reduction, as recently reviewed by *Ceccio* (2010); *Perlin and Ceccio* (2014); *Perlin et al.* (2016). Riblets are poor at reducing drag outside of a very limited design speed range and active methods of friction drag reduction, such as air or polymer injection, require significant mass and energy input (*Bidkar et al.*, 2014; *Bushnell*, 1991; *Garcia-Mayoral and Jimenez*, 2011). Therefore, there remains a need to develop passive methods to significantly reduce skin-friction drag in hydrodynamic flows at high Reynolds numbers.

Researchers have consistently shown that superhydrophobic surfaces (SHSs) can

effectively lower frictional drag in laminar flow (*Jung and Bhushan*, 2010; *Zhao et al.*, 2007; *Watanabe and Udagawa*, 2001; *Rothstein*, 2010; *Gruncell et al.*, 2013; *Busse et al.*, 2013; *Bhushan and Jung*, 2011; *Bixler and Bhushan*, 2013b,a,c; *Jing and Bhushan*, 2013; *Srinivasan et al.*, 2015). However, the extension of frictional drag reduction to wall-bounded turbulent flows has not been straightforward (*Bidkar et al.*, 2014; *Jung and Bhushan*, 2010; *Zhao et al.*, 2007; *Watanabe and Udagawa*, 2001; *Daniello et al.*, 2009; *Woolford et al.*, 2009; *Aljallis et al.*, 2013; *Henoch et al.*, 2006; *Park et al.*, 2014). Both the efficacy and mechanism of these potentially drag-reducing surfaces have been previously debated (*Zhao et al.*, 2007; *Aljallis et al.*, 2013; *Schultz and Flack*, 2007; *Ünal et al.*, 2012; *Golovin et al.*, 2016).

The present work discusses in detail recent contributions to the design and experimental characterization of SHS drag reduction in both internal and external turbulent flows. Specifically, this work examines (1) the approach taken to fabricate SHSs over areas greater than one square meter using a composite spray application, (2) the physical properties that enable a SHS to reduce drag in turbulent flow and (3) the characterization of scalable, mechanically robust SHSs that are able to significantly alter the friction in turbulent flows, at some of the highest Reynolds numbers evaluated to-date. The material addressed here-in was developed in conjunction with a group of researchers contributing to a proposal funded by the Office of Naval Research (ONR) Multidisciplinary University Research Initiatives (MURI) program, entitled, "*Passive and Active Friction Drag Reduction of Turbulent Flows over Super-Hydrophobic Surfaces*". Moreover, this could not be presented in its present form without pivotal contributions from Kevin Golovin, Mathew Boban, and Julio Barros, as well as my committee members, Steven Ceccio, Marc Perlin, Michael Schultz, and Anish Tuteja. The majority of this work stems from three conference papers (*Gose et al.*, 2016a,b, 2017a) and three journal publications (*Golovin et al.*, 2016; *Gose et al.*, 2017b, 2018), of which, the latter two are in review, as well as, many review meetings and conference

presentations.

1.1   Background and Motivation

When liquid flows over a solid surface, the usual boundary condition assumed is that the velocity of the liquid must match the velocity of the solid (*Rothstein*, 2010). This is typically referred to as the 'no-slip' boundary condition. However, SHSs possess a fraction of air at the solid-liquid interface, which can have a non-zero interfacial velocity. In 1823, Navier first proposed a slip velocity, u_s, and suggested that the local shear rate at the wall was proportional to u_s (*Navier*, 1823). This can be described by,

$$u_s = \lambda_x \left| \frac{du}{dy} \right|, \quad v_s = \left| \frac{dv}{dy} \right|, \quad w_s = \lambda_z \left| \frac{dw}{dy} \right| \tag{1.1}$$

where u, v, and w are the velocity components in the streamwise (x), wall-normal (y) and spanwise (z) directions, and λ_i is the slip length along direction i. SHSs can produce slip at the liquid-gas, interface through the incorporation of entrapped air. This is schematically depicted in *figure* 1.1, for a two-dimensional flow over an idealized SHS, where λ_x represents the local slip length in the streamwise direction. Because less energy is lost to frictional dissipation, a non-zero streamwise slip velocity indicates a local reduction in drag at the solid-liquid interface, while a non-zero spanwise slip velocity, w_s, generally results in a local net drag increase as shown by *Woolford et al.* (2009); *Min and Kim* (2004); *Jelly et al.* (2014). Nevertheless, for flow over heterogeneous, randomly rough surfaces, such as those investigated in this work, local regions of slip in an otherwise no-slip flow cannot be used to characterize or predict SHS drag reduction. Instead we must consider an effective slip length λ_{eff}, which has been discussed in detail by *Lauga and Stone* (2003) for flow inside a round pipe with a patterned slip/no-slip boundary conditions, and experimentally evaluated by others
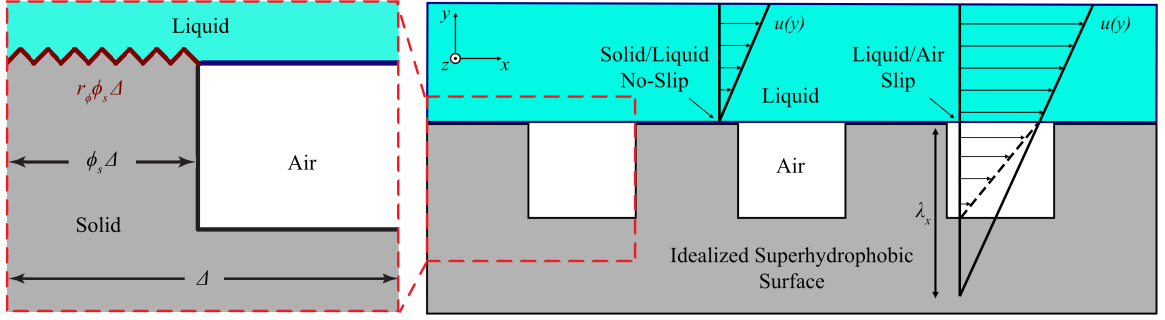
Figure 1.1: The correlation between the details of the surface texture and heterogeneous three-phase interface that can form on a idealized superhydrophobic surface comprised of macro-sized and nano-sized features. Above the solid surface, the velocity of the flow at the wall must go to zero to match the speed of the solid. However, over the air pocket (between micro-sized features separated by a distance $\Delta/2$), the velocity can be non-zero, creating a local slip velocity u_s and a corresponding local slip length λ_x (right). On the upper, horizontal surface of the micro-sized features there are smaller features that are wetted by the liquid water (marked in dark red) (left). This wetted region can be described by $r_\phi \phi_s \Delta$, where r_ϕ and ϕ_s are the ratio of the wetted surface area to its projected surface area and the areal fraction of the surface that is wetted by the liquid, respectively.

(*Gogte et al.*, 2005; *Ou and Rothstein*, 2005; *Joseph and Tabeling*, 2005; *Lee et al.*, 2008). For laminar flows, the drag-reducing ability of SHSs has been confirmed and related to the effective slip, both experimentally and computationally; see the recent review by *Rothstein* (2010). Moreover, effective slip length has a strong dependence on the area fraction of air, and diminishingly small solid fractions for structured SHSs have previously shown laminar friction drag reduction as high as 99% can be achieved (*Kim and Kim*, 2002).

However, the ability of SHSs to afford drag reduction in turbulent flow is not well-characterized (*Bidkar et al.*, 2014; *Jung and Bhushan*, 2010; *Zhao et al.*, 2007; *Watanabe and Udagawa*, 2001; *Henoch et al.*, 2006; *Daniello et al.*, 2009; *Woolford et al.*, 2009; *Aljallis et al.*, 2013; **?**; *Park et al.*, 2014). Whereas small, micro-fabricated surfaces have shown drag reduction anywhere from 10% (*Srinivasan et al.*, 2015; *Woolford et al.*, 2009) to 50% (*Daniello et al.*, 2009; *Henoch et al.*, 2006), large, scalable

SHSs have resulted in drag increase (*Zhao et al.*, 2007; *Aljallis et al.*, 2013; *Bidkar et al.*, 2014; *Vajdi Hokmabad and Ghaemi*, 2016; *Ling et al.*, 2016) of around 10% to 30% drag reduction under certain conditions (*Bidkar et al.*, 2014; *Aljallis et al.*, 2013; *Vajdi Hokmabad and Ghaemi*, 2016; *Ling et al.*, 2016). In turbulent flow, there is an interaction between the near-wall region and the buffer region. The former, known as the viscous sublayer, is dominated by viscous shear stresses, while the latter is dominated by turbulent momentum transfer. This interaction may be modified when micro-features are added to a surface. Additionally, significant momentum transfer is expected in the viscous sublayer due to the presence of the disparate liquid-air and liquid-solid interfaces causing mixed slip/no-slip boundary conditions that can exist on textured surfaces. These near-wall flows are complex due to the many turbulent structures, eddies and vortices that dominate the momentum transfer in the buffer region (*White*, 2006). Moreover, while slip in the direction of flow can result in drag reduction, slip in the spanwise direction can increase the intensity of these turbulent structures, causing a drag increase (*Woolford et al.*, 2009; *Min and Kim*, 2004; *Jelly et al.*, 2014). As a result, surfaces that reduce drag in laminar flow, where these additional flow features are absent, are not guaranteed to continue reducing drag when exposed to turbulent flow.

1.2   Research Objectives

The preceding review is intended to highlight some of the areas of interest in SHS drag reduction, and to demonstrate a number of areas in which improvements may still be made. This discussion focuses on the theory, design, and application of mechanically robust and scalable SHSs; and the efficacy of the SHSs in various flow types, with emphasis on the following objectives:

1. Experimental investigation of robust and scalable SHSs for skin-friction drag

reduction in turbulent flows relevant to naval applications, i.e. high-Reynolds number flows

2. Establishing critical parameters associated with surface topology and wetting that may influence a SHS's ability to decrease (or increase) skin-friction in turbulent flow

3. Extending preliminary SHS findings concluded from previous works, as well as, preliminary experimental SHS characterization in fully-developed turbulent flow applications to higher Reynolds number flows, including external boundary layer flows

4. Constructing guidelines with regard to the development (and 'optimization') of superhydrophobic materials for specific 'high' speed flow applications

1.3 Dissertation Outline

The body of this dissertation has been organized into two introductory chapters, two technical approach chapters, two results chapters, and one chapter for conclusions and future work. In Chapter II, a thorough review of SHS wettability characterization and previous SHS drag reduction work is presented. Major findings from previous SHS drag reduction efforts are highlighted and placed in context for the following chapters. Additionally, Chapter II introduces much of the terminology to be used in the remainder of the dissertation. Chapters III and V describe the technical approaches for two of the experimental efforts undertaken in this work, including the SHS fabrication methods and a complete description of the flow facilities and equipment used to characterize the skin-friction reduction of the SHSs in turbulent flow. Moreover, Chapter III addresses, for the first time, characteristics of the flow facility that was specifically designed for this effort - a novel, high-aspect ratio (width/height), fully-developed turbulent flow facility, while Chapter V discusses the external turbulent

boundary layer facility. Chapter IV presents a detailed discussion of the results from the internal flow application, whereas Chapter VI provides the results and discussion for the external turbulent boundary layer application. Lastly, Chapter VII concludes the work with a summary of the findings, major contributions, and avenues for future research.

CHAPTER II

Biomimetic Superhydrophobic Surfaces for Drag Reduction

Superhydrophobic surfaces (SHSs) have been employed in numerous experimental applications and have received growing interest over the last two decades. Skin-friction drag reduction is only a small focus area for the application of SHSs; however, drag reduction is a significant economic and environmental concern wherever fluid flow is present. Friction loss arises from the shear stress between a solid surface and the fluid flowing flow along or around it, or between two fluids due to their differing viscosities. Likewise, internal friction within the same fluid causes additional losses due to its viscosity. In typical macro-scale flow applications, i.e. high-Reynolds number flows, the external scales are large compared to the molecular scales of the liquid, and thus, the fluid particles will assume the velocity of the solid (*White*, 2006). As shown previously in (1.1), *Navier* (1823) proposed that the tangential wall velocity could be directly related to the fluid slip and local wall-normal velocity gradients.

In most applications, the local slip length is on the order of the mean-free-path of the fluid molecule. For liquid water in macro-flows, the slip length is typically much less than 100 nm and of little consequence to friction reduction. However, in the presence of a surface treatment, such as a superhydrophobic coating, the velocity of the liquid at the wall may significantly differ from the wall. SHSs are known to entrap air

within their porous micro and/or nano-size structure. The presence of this air causes a reduced solid-liquid interaction and increased liquid-air interaction, which has been shown to generate a meaningful slip velocity at the wall, and correspondingly, provide a reduction in friction there. A recent literature review by *Rothstein* (2010) addresses much of the recent work related to slip on SHSs for hydrodynamic drag reduction. The above mechanism is generally accepted as the means of drag reduction in laminar flows; nevertheless, this may not be the case for turbulent flows. Here we discuss the requirements for generating a mechanically robust SHS that may be applied over large areas (> 1 m^2), maintain a high resistance to wetting, and provide meaningful skin-friction savings in turbulent flows, particularly for maritime applications.

2.1   General Superhydrophobic Surface Characterization and Application

Characterizing the wettability of a SHS is critical to predicting its drag reduction capability. SHSs are known for their low surface energy, resistance to wetting, and the effortless rolling of drops placed on them. More specifically, an effective superhydrophobic coating or material combines surface chemistry and surface geometry to modify its interaction with water, resulting in an apparent contact angle greater than 150° and low contact angle hysteresis $\Delta\theta^* \equiv \theta^*_{adv} - \theta^*_{rec}$, i.e. the difference between the advancing and receding contact angles. Although contact angle is not the only parameter for characterizing a SHS, and does not necessarily directly correlate to increased slip length or drag reduction in turbulent flows, it is commonly reported in the literature, and as such it is addressed here. Moreover, as we demonstrate in the following discussion, contact angle measurement may provide indicative insight to other critical properties of a SHS and its interaction with liquid flow. *Figure* 2.1 demonstrates the water repellency of one of the SHSs used in this effort, and again

schematically presents the concept of limited solid-liquid interaction for solid surface containing air pockets.

A drop of water placed on a superhydrophobic material maintains a high contact angle on the basis of two principles. First, for a chemically homogeneous, smooth surface, the equilibrium contact angle θ^Y is directly related to the tangential surface forces acting at the three-phase contact line of the solid, liquid, and gas. The hydrophobicity is enhanced if the surface energy is lowered (*Nakajima et al.*, 2001), following the relation given by *Young* (1805)

$$\cos \theta^Y = \frac{\gamma_{SG} - \gamma_{SL}}{\gamma_{LG}} \tag{2.1}$$

where γ_{SG}, γ_{SL}, and γ_{LG} represent the solid-gas, solid-liquid, and liquid-gas interfacial free energies. In reality, most surfaces are, in some sense, rough, which gives rise to the second principle of establishing a high contact angle.

Two distinct models were developed independently by *Wenzel* (1936) and *Cassie and Baxter* (1944) to describe the apparent contact angle on a rough surface using Young's original formulation of contact angle, shown in (2.1). First, Wenzel considered fully-wetted, rough surfaces characterized by a roughness parameter, r_ϕ, which is defined as the ratio of its actual roughness (typically defined as the arithmetic average of absolute values R_a or the root-mean-square R_{RMS}) to the geometric projected area over which the roughness is measured, where R_a is defined as shown in 2.2, where Z_i represents the height of each roughness feature present on the surface.

$$R_a = \frac{1}{n} \sum_{i=1}^{n} |Z_i| \tag{2.2}$$

This roughness parameter, r_ϕ is always greater than unity. The contact angle of this so-called Wenzel state is then defined as

$$\cos \theta^W = r_\phi \left(\frac{\gamma_{SG} - \gamma_{SL}}{\gamma_{LG}} \right) = r_\phi \cos \theta^Y \tag{2.3}$$

where θ^W is the apparent contact angle of a droplet in the Wenzel state. If the surface is instead partially-wetted (the so-called Cassie-Baxter state), consisting of a liquid-solid and liquid-gas interface, the apparent contact angle θ^* is instead defined by (2.4) as proposed by Cassie and Baxter, assuming a contact angle of 180° between air and water, which are the liquid and gas of interest here.

$$\cos \theta^* = r_\phi \phi_s \cos \theta^Y + (1 - \phi_s) \cos \pi \tag{2.4}$$

In (2.4), r_ϕ is again the ratio of actual wetted surface area to its projected surface area, ϕ_s is the areal fraction of the surface that is wet by the liquid, and $r_\phi \phi_s$ is the fraction of the solid surface in contact with the liquid. Thus, a large contact angle may be obtained by increasing r_s, decreasing ϕ_s, or both. In itself this is an intriguing concept when attempting to achieve skin-friction saving. Increasing the roughness of a surface beyond the hydraulically-smooth limit, which for external flows, is typically defined as five times the viscous length scale ($5 \, \delta_\nu \equiv 5 \, \frac{\nu}{u_\tau}$, where ν is the kinematic viscosity and u_τ is the friction velocity) (*Pope*, 2000) undeniably causes increased drag in turbulent flow. This increase in drag is due to additional momentum transfer between the viscous sublayer and the buffer & overlap layers, and an increase in the turbulent intensity of the flow near the surface. As such, the relative size of the features of a SHS must be designed carefully. The features should not only enhance the resistance to wetting, but also in the realm of drag reduction, the features themselves must be small enough so that they do not negatively influence the flow.

There are numerous examples in nature showing remarkably high contact angles ($> 170°$) and low contact angle hysteresis ($< 10°$). Some of these examples include

insects (*Gao and Jiang*, 2004), bird feathers (*Bormashenko et al.*, 2007; *Liu et al.*, 2008), plants (*Neinhuis and Barthlott*, 1997), and more (*Bhushan and Jung*, 2011). The most commonly cited SHS in nature is the lotus plant (*Barthlott and Neinhuis*, 1997), which is well-known for its self-cleaning properties. One of the most notable features of SHS is the presence of both nano and micro features (*Nakajima et al.*, 2001; *Feng et al.*, 2002). Several examples of SHSs in Nature are presented in *figure* 2.2.

In a recent review of SHS, *Ma and Hill* (2006) address the numerous fabrication methods for generating a composite surface of micron, submicron and nano-scale features that generally result in an increase in contact angle and a decrease in contact angle hysteresis. Surface features with multiple length scales may also result in a smaller ϕ_s during turbulent flow, and thus, a decrease in the shear force. Furthermore, the micro-scale features may provide the adequate length-scale and spacing needed to generate the larger slip necessary for providing skin-friction savings in high-Reynolds number flows, while the nano-scale features may enhance the surface's ability to resist wetting in the presence of the significant pressure perturbations that exist in a turbulent boundary layer.

Since the work of *Onda et al.* (1996), scientists have developed a myriad of new methods to create advanced SHSs in the laboratory that mimic the water repellent properties and hierarchal structures of the lotus leaf. For SHSs specifically related to drag reduction, these fabrication methods include lithography (*Ou et al.*, 2004; *Choi and Kim*, 2006; *Truesdell et al.*, 2006), and aerogel coatings (*Gogte et al.*, 2005; *Samaha et al.*, 2012), anodic oxidation (*Zhao et al.*, 2007), electrodeposition and chemical corrosion (*Zhao et al.*, 2007), plasma etching (*Öner and McCarthy*, 2000), thermal deposition (*Bhushan et al.*, 2009; *Koch et al.*, 2009), and spray deposition (*Bidkar et al.*, 2014; *Srinivasan et al.*, 2015). Although most of the early experimental investigations of SHS drag reduction focused on regularly patterned geometries in

small-scale, laminar flow applications, more recent investigations have included irregular SHSs in larger-scale flows. The latter are considerably less time consuming to produce and applicable in a wider range of settings, primarily due to their scalability, and as such are the primary focus of the work presented here. Examples of these types of engineered SHSs, as well as others, are shown in *figure* 2.3.

2.2   Previous Superhydrophobic Drag Reduction Efforts

As previously discussed, SHSs have been most successful at providing drag reduction in small-scale, internal laminar flows. *Watanabe et al.* (1999) first quantified 14% drag reduction for laminar flow through a 16 mm diameter pipe with a "highly water-repellent wall". Ou and Rothstein (*Ou et al.*, 2004; *Ou and Rothstein*, 2005) demonstrated 40% reduction in pressure drop and 20 mm slip length for laminar flow through micro-channels using micro-sized, structured channels. Other experimental and analytical studies have also examined and found similar results for drag reduction and liquid slip over SHSs in laminar flow (*Lauga and Stone*, 2003; *Gogte et al.*, 2005; *Joseph et al.*, 2006; *Truesdell et al.*, 2006; *Samaha et al.*, 2011; *Busse et al.*, 2013; *Srinivasan et al.*, 2013). Although the applicability of SHSs for drag reduction in laminar flow is generally well understood and accepted, the use of SHSs in turbulent flow is less understood, particularly in macro flow applications. Experimental application of SHSs for skin-friction savings in turbulent flow (*Balasubramanian et al.*, 2004; *Henoch et al.*, 2006; *Zhao et al.*, 2007; *Daniello et al.*, 2009; *Peguero and Breuer*, 2009; *Woolford et al.*, 2009; *Jung and Bhushan*, 2010; *Aljallis et al.*, 2011, 2013; *Bidkar et al.*, 2014; *Park et al.*, 2014; *Srinivasan et al.*, 2015; *Tian et al.*, 2015; *Zhang et al.*, 2015; *Vajdi Hokmabad and Ghaemi*, 2016) have shown mixed results in most investigations with quantifiable drag ranging from a net increase (*Zhao et al.*, 2007; *Aljallis et al.*, 2013; *Bidkar et al.*, 2014), as high as 50%, to savings of 75% (*Park et al.*, 2014) depending on the test conditions, characteristics of the surface texture

and wettability, or the ability of the surface to retain entrapped air pockets. *Daniello et al.* (2009) measured upwards of 50% drag reduction using micro-channel features in a turbulent flow channel for height-based Reynolds numbers between 10^3 and 10^4. *Daniello et al.* (2009) also noted that drag reduction was found to increase with feature size and spacing at a given Reynolds number. *Park et al.* (2014) showed 75% drag reduction for a 27 mm × 27 mm SHS, fabricated using photolithography, in a turbulent boundary layer ($Re \approx 2 \times 10^5$). Additionally, *Park et al.* (2014) demonstrated increasing savings with increasing liquid-gas interfacial area relative to the projected total projected area of the surface ($1 - \phi_s$), confirming that a small ϕ_s is desirable. This finding was recently verified by *Seo and Mani* (2016) in a numerical study which suggested the slip length on a SHS in turbulent flow is correlated directly to the inverse square-root of the solid fraction. Studies by *Aljallis et al.* (2011, 2013) showed drag savings of 30% in external, low-Reynolds number ($Re < 10^6$), transitional flow over a flat plate (≈ 1.2 m), and a drag increase at higher speeds ($Re > 10^6$). Aljallis et al. attributed the net increase in drag to wetting of the SHS, as the trapped air pockets were removed at higher speeds. The wetted SHS then caused additional drag due to roughness effects. *Zhao et al.* (2007) also noted a savings of approximately 9% for a low-Reynolds number turbulent boundary layer and an increase in drag at higher Reynolds number, which they attributed to an increase in near-wall disturbances that contributed to a higher momentum transfer. *Bidkar et al.* (2014) demonstrated that meaningful drag reduction (20 to 30%) can be obtained in a turbulent boundary layer flow ($1 \times 10^6 < Re < 9 \times 10^6$) if the non-dimensional surface roughness is one-tenth of the viscous sublayer thickness. Here the non-dimensional roughness k^+ is typically defined as the surface roughness R_a, e.g. average or root-mean-square, divided by δ_ν. *Table* 2.1 summarizes the previous attempts to characterize drag reduction of SHSs in turbulent flow. The current work is also highlighted in the subsequent table; however, the findings withheld until later in this dissertation.
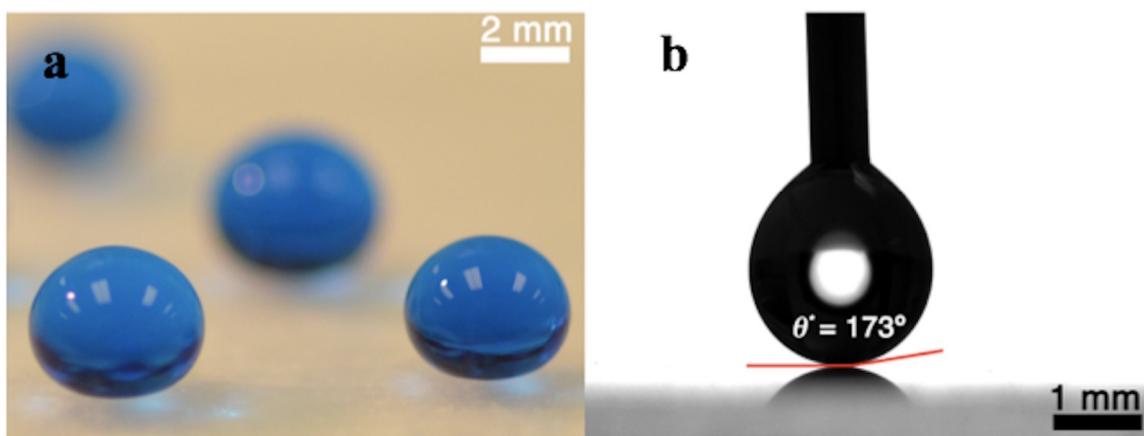
Figure 2.1: (a) Water repellency of a SHS used in this effort showing multiple dyed water drops on the surface and (b) a measured contact angle of 173°. Figure reprinted from *Gose et al.* (2016b).
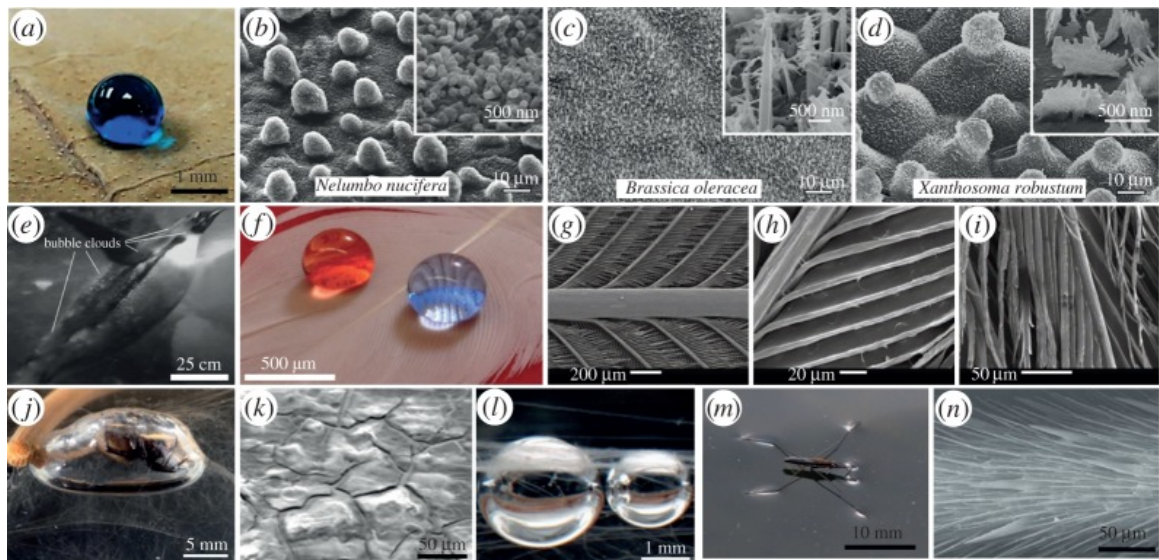
Figure 2.2: Superhydrophobicity in Nature. Water is repelled by the lotus leaf (a) owing to its micro- and nanotexture (b) (*Kota et al.*, 2014). Other plants exhibit similar properties, such as broccoli (c) or taro (d) (*Mockenhaupt et al.*, 2008). Animals such as penguins (*Davenport et al.*, 2011) (e) and ducks (f) also display water repellency owing to the texture of their feathers (g-i) (*Srinivasan et al.*, 2014). The diving bell spider lives under water inside a plastron (j), a bubble of air it drags beneath the water using spider silk (k,l) (*Neumann and Kureck*, 2013). A water strider (m) similarly controls the air–water interface with the fine hairs on its legs (n). (a,b,m,n) From (Science 7 December 2007: vol. 318, Issue 5856, pp. 1618–1622; doi:10.1126/science.1148326). Figure reprinted from *Golovin et al.* (2016).
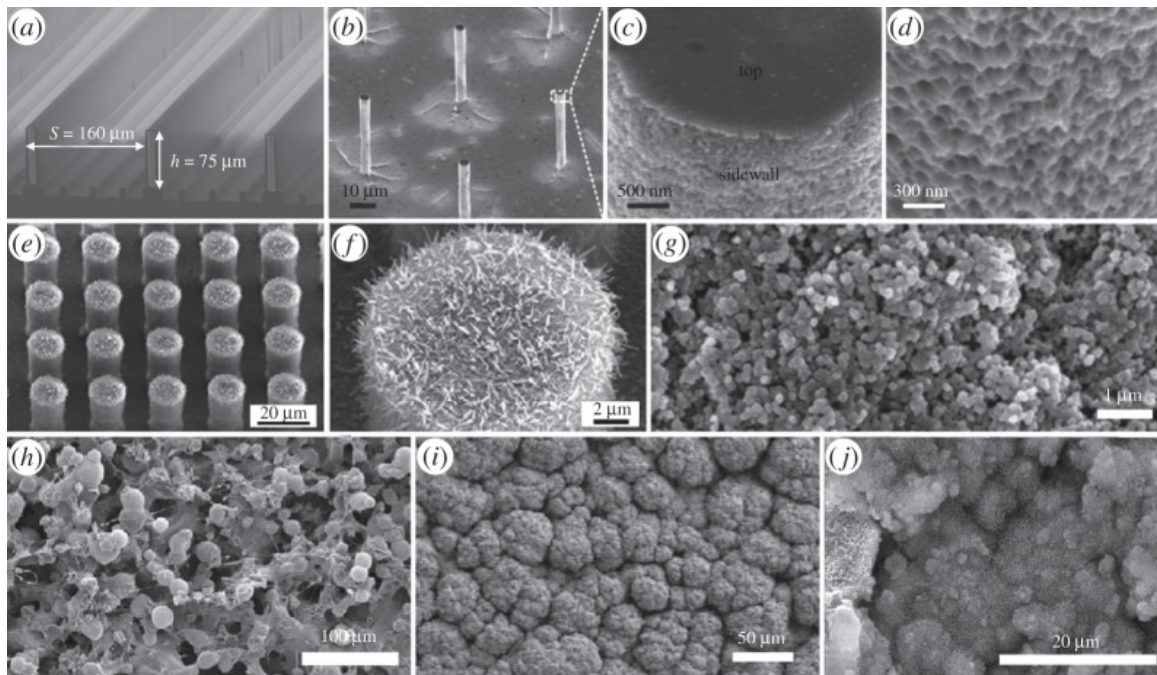
Figure 2.3: Engineered superhydrophobic surfaces tested in turbulent flows. Hierarchical ridges (a) (*Prince et al.*, 2014) or posts (b-d) have been fabricated using microlithography (*Lee and Kim*, 2009). Nanotexturing can also be achieved using vapour deposition techniques (e,f). (Adapted from (*Lee and Kim*, 2009).) The texture of the commercial superhydrophobic spray NeverWet (g) *Vajdi Hokmabad and Ghaemi* (2016). Other randomly structured superhydrophobic surfaces can be fabricated using spray-coating (h) (*Srinivasan et al.*, 2015), thermal deposition (i) (*Bidkar et al.*, 2014) or chemical etching procedures (j). ((h) Reprinted from *Srinivasan et al.* (2011).) Figure reprinted from *Golovin et al.* (2016)
.

Ref.	Geometry	θ^*	$\Delta\theta$	Length (cm)	Re_τ	DR (%)
Park et al. (2014)	Ridges	-	-	2.7	250	+ 0 to +70
Gogte et al. (2005)	Random	156°	-	4.3	40 - 288	+ 3 to +18
Jung and Bhushan (2010)	Posts	173°	1°	6	0 - 18	+ 0 to +30
Woolford et al. (2009)	Ridges	160°	-	8	3 - 100	- 7 to +11
Bidkar et al. (2014)	Random	155°	-	15	1000 - 5000	-13 to +30
Ling et al. (2016)	Random	159°	-	15	693 - 4496	-10 to +36
Henoch et al. (2006)	Posts, Ridges	-	-	20	150 - 600	+ 0 to +50
Henoch et al. (2006)	Random, Posts	-	-	43	200	-50 to +40
Vajdi Hokmabad and Ghaemi (2016)	Random	165°	-	50	2530	+ 0 to +15
Srinivasan et al. (2015)	Random	161°	0°	60	480 - 3810	+ 0 to +22
Zhao et al. (2007)	Random	-	-	80	1700 - 3300	- 5 to + 9
Daniello et al. (2009)	Ridges	-	-	100	100 - 300	+ 0 to +50
Aljallis et al. (2013)	Random	164°	5°	122	520 - 5170	-30 to +30
Gose et al. (2017b) - This work	Random	> 161°	< 5°	120	215 - 950	-90 to +90
Gose et al. (2017a) - This work	Random	> 161°	< 5°	120	1600	-11 to +36

Table 2.1: Previous studies on drag reduction in turbulent flow with corresponding geometry of surfaces, apparent contact angle θ^* and contact angle hysteresis $\Delta\theta$ when reported, where $\Delta\theta$ is equal to the difference between the advancing contact angle θ^*_{adv} and receding contact angle θ^*_{rec}. Lengths of the tested surfaces, range of friction Reynolds numbers evaluated ($Re_\tau = H/2\delta_\nu = \delta/\delta_\nu$ where H is the channel height, δ_ν is the viscous length scale and δ is the effective boundary layer thickness) and the observed drag reduction (positive) or drag increase (negative) are also tabulated.

It is evident from the current review that there are issues that limit the application of SHSs for drag reduction in turbulent flow. The first concern is the inherent interaction of the SHS with the liquid flow. This is of particular concern in the near-wall region, where the elemental micro-features of the SHS can have a significant impact on the near-wall turbulence, and may enhance turbulent momentum transfer between the viscous sublayer and the overlap region. Additionally, the elements themselves, if large enough, may impose themselves on the liquid flow in such a way that the SHS appears to be a rough surface. If so, the largest features of the SHS will add an additional component of form drag to the average wall-shear stress. Furthermore, it is essential that the SHS maintain the Cassie-Baxter state, even in the presence of the high-shear, enhanced mixing, and pressure perturbations of a turbulent boundary layer. It pis expected that under certain conditions, the unsteadiness of the turbulent flow may be able to drive the air from the surface, whether by pressure perturbations or by general decreased pressure, causing the surface to transition to a wetted, Wenzel state. If this occurs, the first issue regarding interaction of the SHS with the near-wall flow may be compounded, and the surface may appear to be fully-rough. Lastly, the robustness of a surface to maintain the Cassie-Baxter state, while limiting the wetting of features, i.e. maintaining a low ϕ_s, enhances a surface's ability to reduce drag. As liquid water flows over the SHS, forces are exerted normal to wall, forcing the gas pockets to compress and spread. When this occurs, liquid will begin to wet additional features of the SHS. This wetting increases r_ϕ and ϕ_s, and results in significant additional solid-liquid interaction.

2.3 Superhydrophobic Surface Development and Application for the Current Effort

To better understand the underlying physics associated with SHSs and drag reduction in the turbulent flow regime, several scalable spray and chemically etched SHSs were developed to be evaluated for a range of Reynolds numbers and in different types of turbulent flows. The SHSs were spray-applied to a base substrate of polycarbonate, acrylic, or stainless steel. In the case of the chemically-etched aluminum SHS, the surfaces were fabricated using 6061 aluminum and bonded to a stainless steel substrate. The substrates were then placed in one or both of the two flow facilities for characterization of their drag reducing abilities. The SHSs adhere to the traditional standards for wettability measurements, including large contact angle ($\theta^* > 160°$), low contact angle hysteresis ($\Delta\theta < 3°$), and a small solid-liquid areal fraction ($\phi_s \leq 0.11$). Moreover, a range of roughness was considered, although the non-dimensional roughness was generally set to be less than the height of the viscous sublayer. Critical analysis of these surface characteristics and the flow properties permitted meaningful insight needed to expand on previous studies, as well as, further the development of SHSs and their resulting drag reduction characteristics.

Variations of these surfaces with very similar properties were implemented in two experimental efforts: an internal, fully-developed turbulent flow (*Gose et al.*, 2016b, 2017b) and an external boundary layer flow (*Gose et al.*, 2017a, 2018). Samples of the coatings were used to characterize the SHSs' roughness and wettability prior to testing. A Philips XL30 FEG scanning electron microscope was used to image the surfaces and surface profilometry was performed using an Olympus LEXT interferometer. Using a step size of 1.25 μm and an overall scan area of 2.50 mm $\times$ 2.50 mm, the two-dimensional root-mean-square roughness S_q, as defined in (2.5), was computed and averaged for the three areas.

$$S_q = \left(\frac{1}{A} \int \int_A Z^2(x,y) dx dy \right)^{1/2} \tag{2.5}$$

In Eq. 2.5, A is the area being characterized and Z is the height of the surface at point (x, y).

A detailed description of the technical approach for the fabrication of the SHSs for both the fully-developed internal flow and the near-zero pressure gradient external boundary layer flow are subsequently described in Chapters III and V, respectively. The results from the experimental flow studies and the characterization the of each SHSs drag reducing ability is detailed in Chapter IV and Chapter VI.

CHAPTER III

Technical Approach I: Internal Fully-Developed Turbulent Boundary Layer Flow

Several SHS coatings were designed and fabricated for application in multiple flow types. In this chapter, the fabrication of the SHSs for the internal flow facility and the flow facility itself are described. First, the surfaces and fabrication methods are discussed. These surfaces all displayed $\theta^* > 161°$; $\Delta\theta < 3°$, when measured using a water droplet and goniometer. Images and characteristics of each surface are provided and tabulated. A description of the fully-developed flow facility follows. The flow facility design, geometric characteristics, and a discussion of the experimental instrumentation is provided. An account of the experimental uncertainties and flow characterization over a hydrodynamically-smooth baseline concludes the chapter. This chapter closely resembles the archival works by *Gose et al.* (2016b, 2017b).

3.1 Superhydrophobic Fabrication for Internal Flow Experiments

Four different SHSs were developed for characterization in the internal flow facility. Scanning Electron Microscopy (SEM) was performed using a Phillips XL30 FEG. Samples were first sputtered with a gold-palladium alloy to avoid charging. SEM

micrographs of the four SHS surface formulations are shown in *figure* 3.1. Surface parameters such as the Root-Mean-Square (RMS) roughness k, which is equivalent to S_q [see (2.5)] were extracted from the optical heightmaps, collected as described in Chapter II. Moreover, a summary of the surface types, roughness, and contact angle measurements are shown in *table* 3.1.
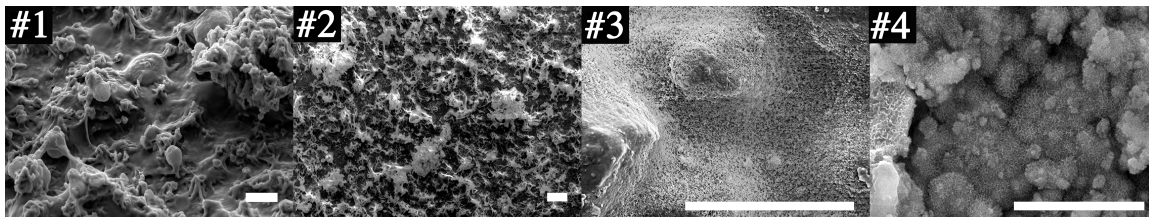
Figure 3.1: SEM micrographs of the four SHSs produced for characterization in the internal flow. Scale bars are 20 μm.

Surface #1 was fabricated from an 80/20 wt% blend of a fluorinated polyurethane (FPU) and fluorodecyl polyhedral oligomeric silsesquioxane (F-POSS) (*Mabry et al.*, 2008). The polyurethane was cross-linked using 3.4 wt% 4,4'-Methylenebis(cyclohexyl isocyanate) (HMDI). The blend was dissolved in Vertrel XF at an overall concentration of 100 mg/mL and probe sonicated until optically transparent. 40 mL of the solution was sprayed onto the 1.20 m × 0.10 m stainless steel substrates using an ATD Tools 6903 high volume-low pressure spray gun with compressed air at a pressure of 20 psi. The sample was then cured at 80 °C for 72 hours. SEM micrographs of Surface #1 are shown in *figure* 3.2.

Surface #2 consisted of a 50/50 wt% blend of cyanoacrylate (SF100) and F-POSS. The two components were dissolved at a concentration of 50 mg/mL in Asahiklin-225 and then sprayed using the same procedure as for surface #1. Surface #2 was cured at 50 °C for 60 minutes. The morphology of this system was altered in the following manner. To increase asperity roughness, the total spray solution volume was tripled to 120 mL. To decrease asperity roughness, the spray gun was replaced with a Paasche airbrush producing a spray with smaller droplets, as described in a
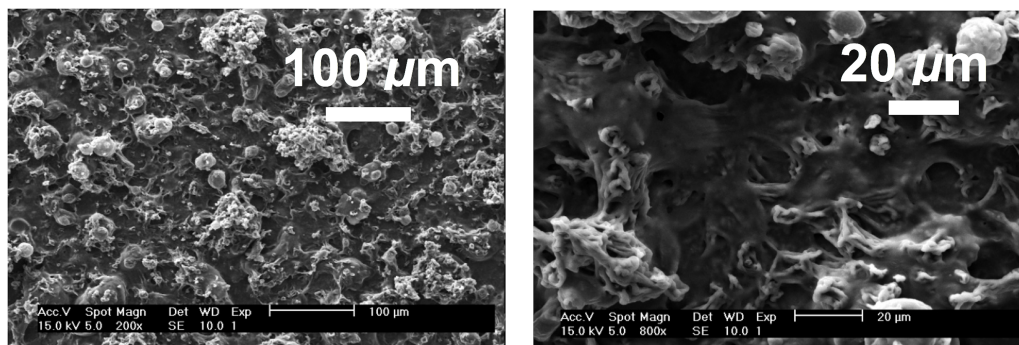
Figure 3.2: SEM micrographs of Surface #1 at two different scales. Figure from *Gose et al.* (2016b).

previous work (*Golovin et al.*, 2013). SEM micrographs of Surface #2, and variants of Surface # 2 are shown in *figure* 3.3.

Surface #3 was fabricated from a blend of the fluorinated polyurethane from surface #1 and 35 wt% fluoro-functionalized silica particles (irregular aggregates approximately 50 - 100 nm in diameter), the synthesis of which is reported elsewhere (*Campos et al.*, 2011). The two components were dispersed at a concentration of 25 mg/mL in Vertrel XF and then 20 mL was sprayed following the same procedures as surfaces #1 and #2. This surface was cured at 80 °C for 72 hours. SEM micrographs of Surface #3 are shown in *figure* 3.4.

Surface #4 was comprised of 6061 aluminum (Al) metal sheets that were etched, boiled, and subsequently functionalized with a fluoro-silane, following modified procedures from previously reported techniques (*Yang et al.*, 2011). Aluminum sheets 0.2 m × 0.1 m × 0.003 m were first etched in 2.5 M hydrochloric acid for 20 minutes. Following etching, the samples were sonicated to remove residual Al flakes adhered to the surface. The etched Al was then boiled in deionized water for 20 minutes. Finally, the surface was exposed to 1H,1H,2H,2H-Heptadecafluorodecyl triethoxysilane vapor overnight at 80 °C under vacuum. To span the full channel length, approximately five sheets were tiled onto the substrate panel. SEM micrographs of Surface #4 are shown in *figure* 3.4.
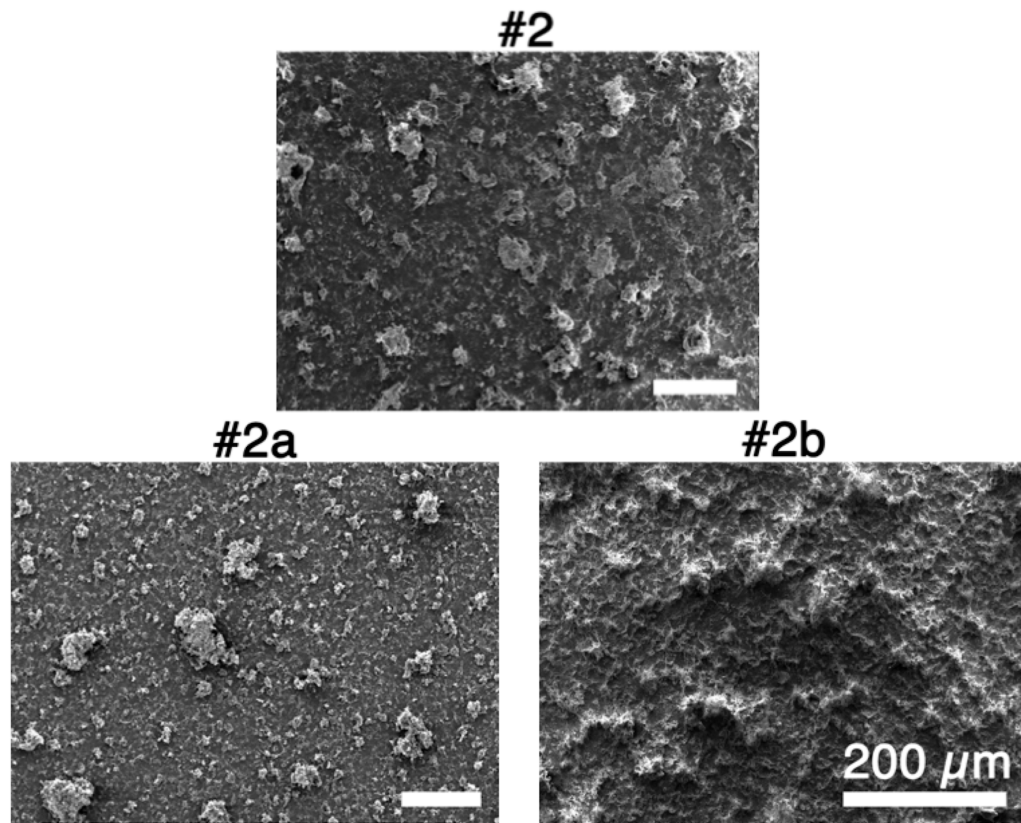
Figure 3.3: SEM micrographs of Surface #2, #2a (rougher) and #2b (smoother). Each reference scale bar (white line) represents 200 μm. Figure from *Gose et al.* (2016b).
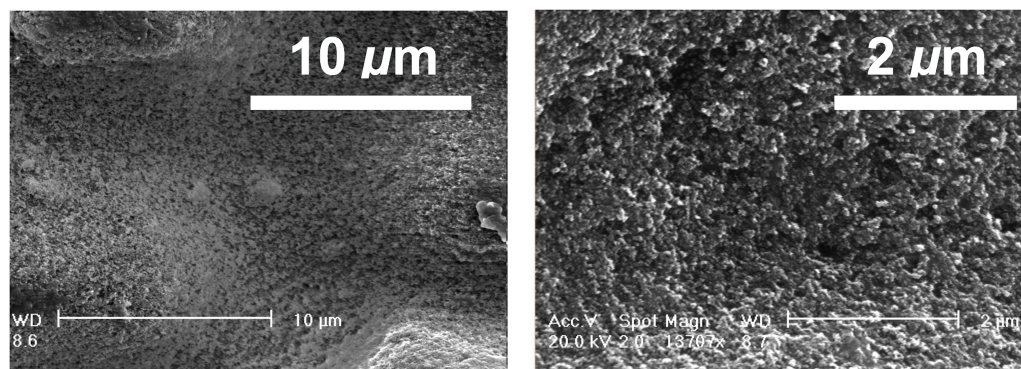
Figure 3.4: SEM micrographs of Surface #3 at two different scales. Figure from *Gose et al.* (2016b).
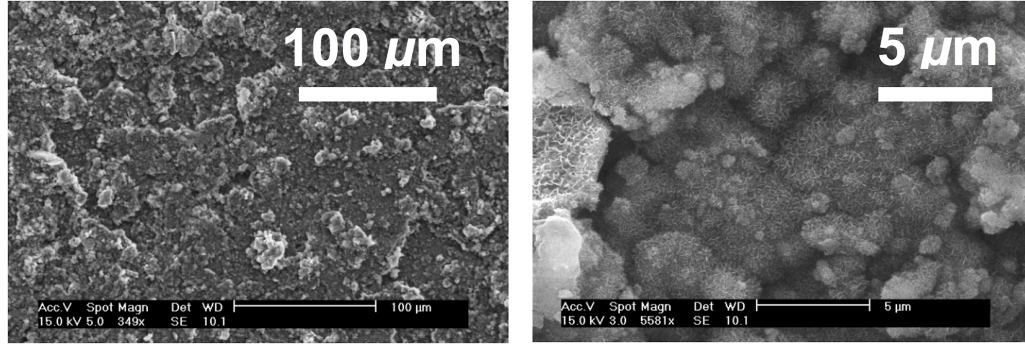
Figure 3.5: SEM micrographs of Surface #4 at two different scales. Figure from *Gose et al.* (2016b).

These four SHSs are mechanically durable (*Golovin et al.*, 2017), easy to fabricate, and were applied over areas of 1.20 m × 0.10 m, an order of magnitude larger than most other SHSs previously tested (*Bidkar et al.*, 2014; *Jung and Bhushan*, 2010; *Daniello et al.*, 2009; *Henoch et al.*, 2006; *Park et al.*, 2014) in turbulent flows.

Additionally, the commercially available coating NeverWet® (Ross Nanotechnology, LLC) was sprayed on a 1.2 m x 0.10 m substrate per manufacturer instructions. First, a base-coat is sprayed once and allowed to cure for 30 minutes at ambient temperature. Next, the topcoat is applied and allowed to dry for two minutes. The application of the topcoat was repeated three additional times, per manufacturer recommendation. Then the final coating is allowed to cure for 24 hours. SEM micrographs of the NeverWet® surface features can be found in *Aljallis et al.* (2011, 2013); *Zhang et al.* (2015); *Vajdi Hokmabad and Ghaemi* (2016).

Surface Number	Contact Angle θ^* [deg]	Contact Angle Hysteresis $\Delta\theta$ [deg]	Areal Fraction ϕ_s	RMS Surface Roughness k [μm]	Non-dimensional Roughness k^+
#1 (FPU + F-POSS)	163 ± 2	3	0.09	18 ± 1	2.4 - 4.9
#2 (SF100 + F-POSS)	161 ± 5	1	0.11	6.4 ± 0.8	0.62 - 0.98
#2a (rougher)	161 ± 3	1	0.10	8.5 ± 0.4	1.2 - 1.6
#2b (smoother)	167 ± 2	0.5	0.04	2.7 ± 0.3	0.16 - 0.34
#3 (FPU + f-SiO2)	172 ± 2	2	0.02	2.2 ± 0.2	0.11 - 0.40
#4(Etched Al)	170 ± 2	1	0.03	4.7 ± 0.7	0.47 - 1.3
NeverWet®	166 ± 2	1	0.04	13 ± 2	1.2 - 2.9

Table 3.1: Summary of the SHSs fabricated for this work, with their low pressure apparent contact angle θ^*, contact angle hysteresis $\Delta\theta^* \equiv \theta^*_{adv} - \theta^*_{rec}$, arial fraction ϕ_s, RMS roughness k, and non-dimensional roughness k^+. Here k^+ is k non-dimensionalized by the viscous length scale δ_ν.

3.2 Internal Fully-Developed Turbulent Flow Facility

We evaluated the skin-friction of the aforementioned SHSs in a fully-developed turbulent channel flow at various flow speeds using pressure drop measurements and Particle Image Velocimetry (PIV). The test facility is shown in *figure* 3.6. Two noteworthy characteristics of channel flow prove efficacious when compared to zero-pressure gradient flows for the fundamental evaluation of skin-friction in turbulent flow, and particularly, for the development and characterization of SHSs for drag reduction. First, channel flows are internal and have a confined outer length scale (channel height H), which is fixed by the opposing walls. In zero-pressure gradient flows the outer length scale δ is unrestricted and grows as a function of distance along the surface. A fixed outer length scale eliminates the dependence of the spatial location on scaling, and results in the scaling being primarily dependent on the bulk-flow variables. Second, channel flow facilities simplify the determination of frictional drag by measurement of the pressure drop for a fully-developed turbulent flow. Pressure drop analysis offers the simplest, and perhaps, the most widely utilized method of measuring skin-friction for internal flows. *Schultz and Flack* (2013) provide a thorough discussion of Reynolds-number scaling for turbulent channel flow and ultimately conclude, channel flow results show Reynolds-number scaling trends that are consistent with recent experimental results from pipe and boundary layer flows. Our channel's height-based Reynolds number Re_H ranged from 10,000 to 40,000, and was calculated using (3.1).

$$Re_H = \frac{U_m H}{nu} \tag{3.1}$$

The experiments were conducted at the University of Michigan. The dimensions of the channel test section are nominally 0.0073 m in height H, 0.10 m in width W, and 1.2 m in length L. The resulting channel cross-section aspect ratio (H/W)

of approximately 14:1 sufficiently exceeds the suggested aspect ratio of 7:1 and 8:1, offered by *Dean* (1978) and *Monty* (2005), needed to provide two-dimensional flow through the center of the channel. Two-dimensionality of the flow was also validated using spanwise pressure measurements on either side of the channel centerline. The flow facility is coupled to a 11.2 kilowatt centrifugal pump controlled by a variable frequency drive. The mean flow speeds obtainable in the test section range from 1 to 20 ms^{-1}. The flow rate was set and measured using an ultrasonic flow meter with an accuracy of approximately 1% and later validated using PIV analysis of the mean flow field. This allows for a Re_H of up to 145,000, corresponding to a smooth-wall friction Reynolds number Re_τ of 3,200 .

A turbulence management section was placed upstream of the test section to improve flow uniformity, remove large-scale vortices, and to reduce the free stream turbulence intensity. A wide-angle diffuser with a divergence angle of approximately 22 degrees and an area ratio of 2.5 was used to transition from the 4-inch pipe used in the recirculation loop to a larger rectangular area, which permitted the use of a large-area contraction upstream of the test section. The typical properties of wide-angle diffusers are area ratios of two to four at divergence angles of about 45 degrees (*Mehta and Bradshaw*, 1979; *Barlow et al.*, 1999). However, in such a diffuser, flow separation could only be avoided by using boundary layer control, often in the form of a series of several screens. As such, experimental data provided by *Sovran and Klomp* (1967) were used to design a rapid, one-dimensional expansion, with a reduced divergence angle and curved walls, to eliminate the need of screens for boundary layer control, and to increase the pressure recovery compared to that of a wide-angle diffuser.

A honeycomb section and screens were installed directly downstream of the wide-angle diffuser. The honeycomb is composed of tubular polycarbonate construction, having a cell diameter and length of 3.175 mm and 25 mm respectively, resulting in a length to diameter ratio of eight; it has a porosity of 0.80 as suggested by
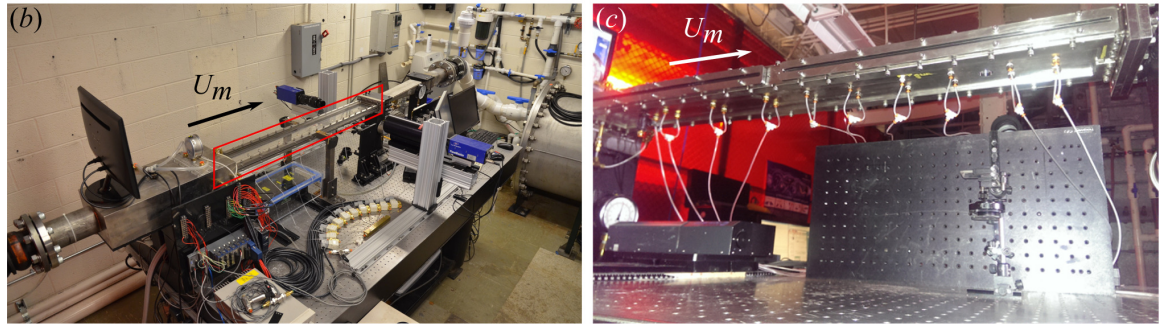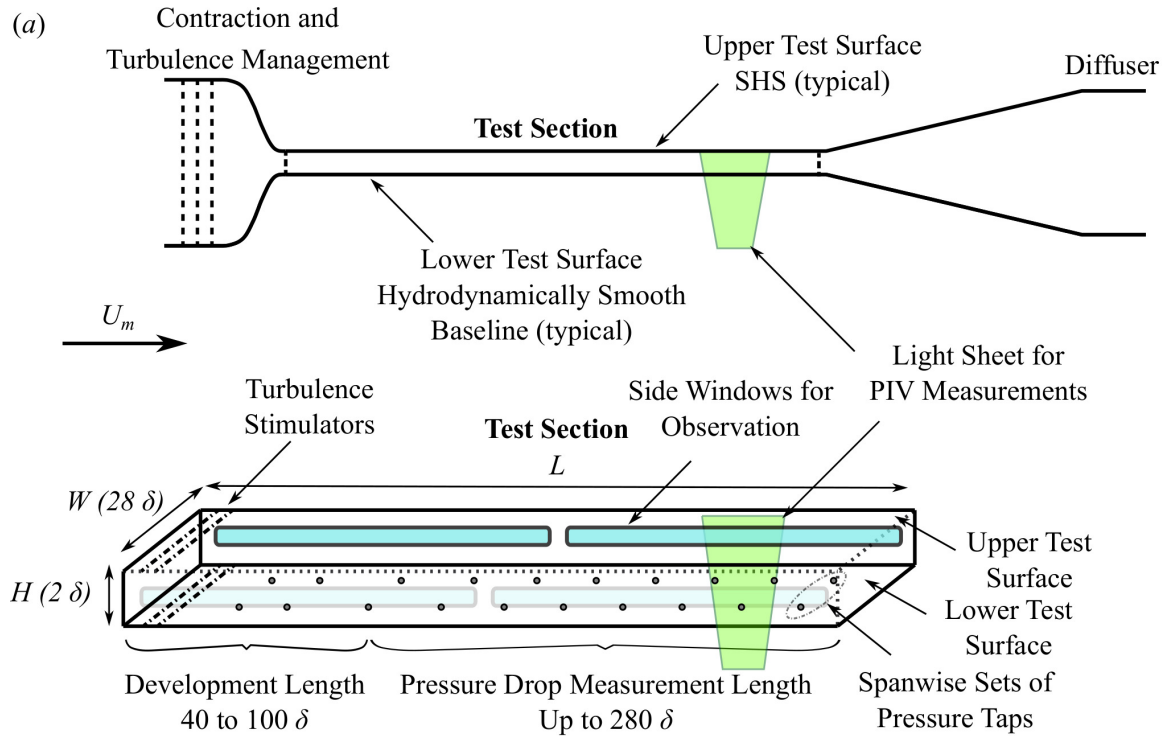
Figure 3.6: Schematic and images of the fully-developed turbulent flow facility. (*a*) The major flow components of the flow facility. (*b*) Image of the flow facility. Fabricated SHSs are inserted into the top of test section (outlined in red). (*c*) Image of the pressure taps used for to infer the skin-friction, viewed obliquely from the underside of the test section.

Barlow et al. (1999). A series of two screens are placed immediately downstream of the honeycomb to further reduce vortical structures. The screen's mesh is 26×26 (number of openings per linear inch or 25.4 mm) with a wire diameter of 0.19 mm and an open area of 0.65, so as to avoid instabilities which occur for open areas less than 0.57. The flow then passes through a two-dimensional, rectangular contraction composed of two sets of symmetric, matched cubic arcs in the vertical and horizontal planes. The two-dimensional contraction is used to achieve the desired wall-pressure coefficients within the shortest possible nozzle length while preventing detached flow at the exit (*Morel*, 1977). The horizontal contraction ratio is two and the vertical contraction area is 15, resulting in a total contraction ratio of 30, over a length of 3.55 cm.

The flow is tripped at the entrance of the test section using a 25 mm streamwise length of 50 grit, waterproof sandpaper spanning the full width of the upper and lower channel surfaces, resulting in a blockage ratio of approximately 20%. Tripping ensures that fully-developed flow is obtained at downstream measurement locations for lower Reynolds number flows. Results provided by *Durst et al.* (1998) suggest that flow characteristics remain independent of conditions at the channel inlet for blockage ratios greater than 15%.

The pressure is measured using three, speed-matched differential pressure transducers, GE UNIK 5000, connected to a series of pressure ports located along the bottom of the 1.2 m long channel test section. The pressure transducers have a manufacturer specified accuracy of 0.04% of the full-scale output. Two pressure taps, measuring 0.75 mm in diameter and 3 mm in length, were placed 16.67 mm to each side of the channel centerline and longitudinally at $20H$, $30H$, $50H$, $70H$, $84H$, $98H$, $112H$, $126H$, $140H$, and $150H$ from the trip at the channel inlet. The streamwise pressure measurements along the channel were used to validate that the flow was fully-developed. Although various development lengths are often quoted, it turns out

that a development length of $30H$ was sufficient to ensure a fully-developed state of the mean-pressure distribution in the flow direction, as presented by *Zanoun et al.* (2009). An image of the pressure taps along the test section is shown in *figure* 3.6(c).

Optical access is provided along the length of the test section for visual observations and to allow flow field measurements. PIV is used to validate the volumetric flux measurements and to provide a local velocity evaluation using a Flowmaster 3S imager coupled to a Sigma APO Macro 180 mm F2.8 EX DG OS HSM and a Sigma APO 2X teleconverter. The resulting field of view is 8 mm × 10 mm with a square pixel size of 7.8 μm. The flow field is seeded with TiO_2 particles, with a nominal mean diameter to 2 to 3 μm, and illuminated using a New Wave Solo, Nd:YAG laser, combined with a series of three cylindrical lenses, in a configuration recommended by *Raffel et al.* (2007), which resulted in a light sheet with a thickness of approximately 0.5 mm. As many as 1,200 image pairs are recorded and analyzed to determine the mean flow field speed using a commercial processing software.

The skin-friction on the surfaces is inferred from the streamwise pressure gradient dP/dx in the test section. Using a simple momentum balance of turbulent channel flow gives the wall shear stress

$$\tau_w = \frac{H}{2} \left| \frac{dP}{dx} \right| \tag{3.2}$$

where H is the channel height. The static pressure is measured at various longitudinal locations, and thus is used to confirm that dP/dx, and consequently, the water flow is fully-developed. Using τ_w, the friction velocity at the wall u_τ and the average skin-friction coefficient can be determined as follows.

$$u_\tau = \sqrt{\frac{\tau_w}{\rho}} \tag{3.3}$$

$$C_f = \frac{\tau_w}{\frac{1}{2}\rho U_m^2} \tag{3.4}$$

Here ρ is the density of water and U_m is the mean speed in the test section. For the smooth channel, C_f can be compared directly to historical results, as is shown later in *Section* IV. Specifically, for historical comparison we used a refined-C_f relation provided by *Zanoun et al.* (2009), which is an empirical power relation dependent on Re_H for turbulent channels and in good agreement with previous results provided by *Dean* (1978).

$$C_{f,Zanoun} = 0.0743 \; Re_H^{-0.25} \tag{3.5}$$

$$C_{f,Dean} = 0.073 \; Re_H^{-0.25} \tag{3.6}$$

In the current work, the skin-friction is inferred from the streamwise pressure gradient measured over one hydrodynamically-smooth baseline and each SHS. Therefore, the resulting skin-friction is the average of the baseline and the SHS, and consequently, a two-sided SHS test section is expected to provide twice the savings in skin-friction. The drag reduction is defined as

$$DR = 2 \; \times \; \left(\frac{C_{f,baseline} - C_{f,SHS}}{C_{f,baseline}} \right). \tag{3.7}$$

where the subscripts *baseline* and *SHS* indicate the C_f inferred for two, hydrodynamically-smooth baseline surfaces and one-SHS with one hydrodynamically-smooth baseline surface installed in the test section, respectively.

3.3 Experimental Uncertainty

The flow rate is set and measured using an ultrasonic flow meter with an accuracy of approximately $\pm 1\%$ and is later validated using PIV analysis of the mean flow field. The velocity measurements collected using the two methods discussed are determined to yield results to be within $\pm 2\%$ of each other. Moreover, as previously discussed, the GE UNIK 5000 pressure transducers have a manufacturer specified accuracy of $\pm 0.04\%$ of the full-scale output, accounting for the combined effects of non-linearity, hysteresis and repeatability.

The channel height is extremely critical in this application and can vary significantly with each SHS, and thus, is the most significant source of error. As such, great effort is made to control and evaluate the channel height for each experiment. Each test substrate is measured before and after the application of each coating to estimate the impact of the coating thickness on the height of the channel. Additionally, after the SHS is installed, the channel height is evaluated optically with a camera set up, with a known spatial calibration, in an elevation view. The channel height is also measured with a set of Starrett precision gage blocks and a bore gage following testing. The side windows of the channel test section were removed and the channel height is measured and recorded at five streamwise locations. Given the three methods used to evaluate the channel height, it is believed tha the aforementioned process, permits a precise and accurate measurement method of H, with which to calculate Re_H and C_f with confidence. Propagation of these errors resulted in an expected error in C_f of less than $\pm 8\%$, with typical error values less than 5%.

3.4 Baseline Results - Velocity Profile and C_f

Characterization of the flow facility for a hydrodynamically-smooth baseline surface is preformed. Flow field velocity profiles are shown for the hydrodynamically-

34

smooth baseline in *figure* 3.7. DNS data of *Kim et al.* (1987) is provided for comparison and is shown to be in good agreement for the two Re_H provided. The measured baseline skin-friction is shown in *figure* 3.8 and is shown to match the historical curves for skin-friction within the stated accuracy of $\pm 8\%$.
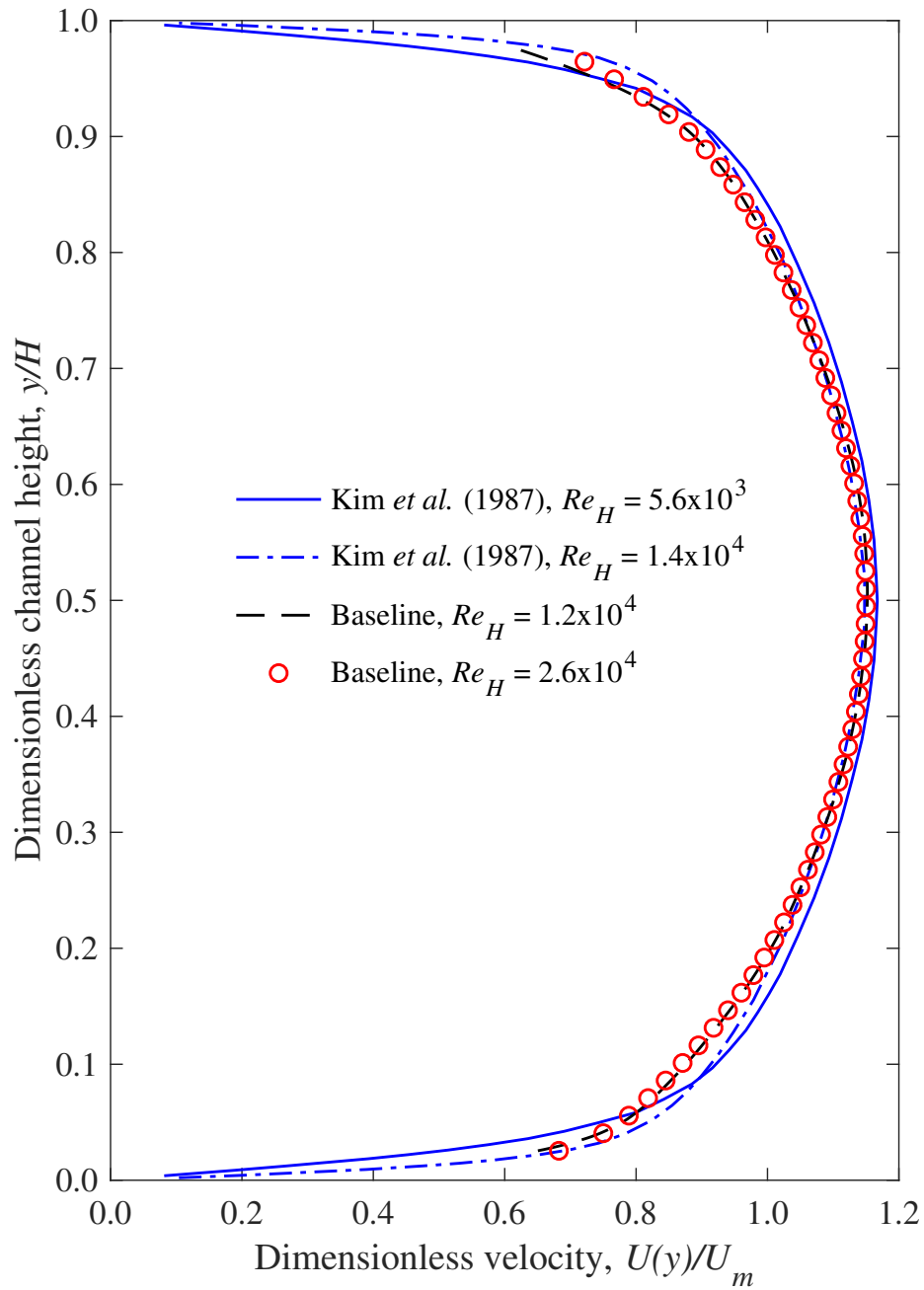
Figure 3.7: Mean velocity profiles for flow between two hydrodynamically-smooth baseline substrates at $Re_H = 1.2 \times 10^4$ and $Re_H = 2.6 \times 10^4$. DNS data for *Kim et al.* (1987) $Re_H = 5.6 \times 10^3$, and $Re_H = 1.4 \times 10^4$ are provided for reference.
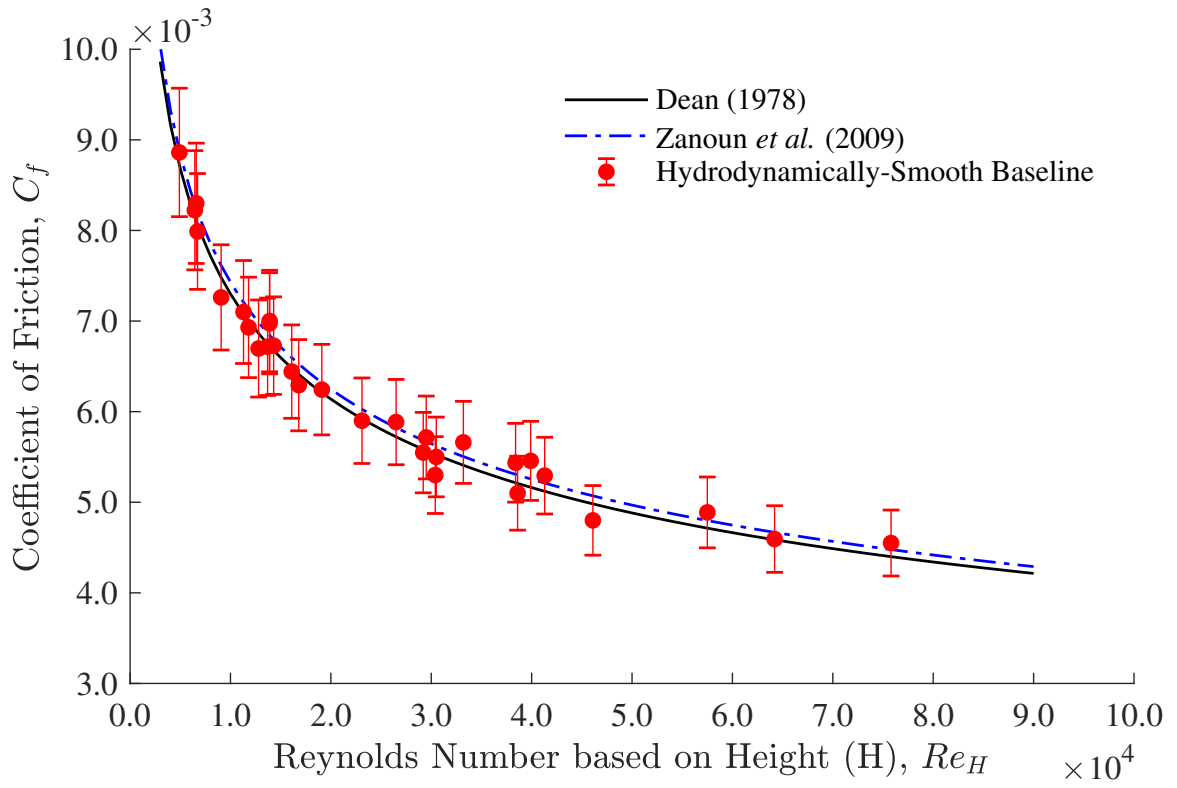
Figure 3.8: The measured baseline skin-friction coefficient data graphed as a function of Re_H for fully-developed turbulent channel flow. Reference correlations by *Zanoun et al.* (2009) and *Dean* (1978), shown in (3.5) and (3.6), are provided.

CHAPTER IV

Results and Discussion I: Internal Fully-Developed Turbulent Boundary Layer Flow

This chapter characterizes the skin-friction on essentially heterogeneously, randomly rough, spray-applied SHSs in fully-developed turbulent flow. First, velocity profiles and shear stress measurements are provided and discussed. Next, skin-friction for each SHS is provided for a range of Reynolds numbers. The results are then used to characterize each surface's drag reducing potential, and highlight the physical mechanisms, which (1) permit SHS drag reduction in fully-developed turbulent flow and (2) may prevent a SHS from providing a reduction in skin-friction. Surface topology and wettability is discussed thoroughly, and used to provide scaling laws for SHS drag reduction. This chapter closely resembles the archival work by *Gose et al.* (2016b, 2017b).

4.1   SHS Results - Velocity Profile and C_f

Flow field velocity profiles are shown for the hydrodynamically-smooth baseline and each of the SHSs is shown in *figure* 4.1. DNS data of *Kim et al.* (1987) is provided for comparison. The results show the effect of the presence of the heterogeneously, randomly rough, SHSs as examined through the results of the mean velocity profile in

the fully-developed channel flow. The PIV analysis of the hydrodynamically smooth, baseline channel is shown to be in good agreement with the mean velocity profiles from the direct numerical simulations (DNS) of *Kim et al.* (1987). However, significant deviation is observed when reviewing the results from the variations of surface #2. Specifically, the maximum flow speed, which is typically located along the centerline of a symmetric, fully-developed channel, shifted towards the hydrodynamically smooth baseline surface ($y = 0$) as the roughness of the SHS increased. From the streamwise conservation of mass and momentum, this necessarily dictates that the fluid speed decreased near the 'rough' wall, and consequently, the interaction with the roughness elements increased. Ideally, if the roughness elements are small compared to the purely viscous sublayer, which is defined conventionally as five times the viscous length scale $\delta_\nu \equiv \nu/u_\tau$ (*Pope*, 2000), no drag increase is expected. This is observed with the less rough variant of surface #2. For the smoother surface there is a slight decrease in the maximum velocity and a slight increase in flow speed near the SHS wall. The flow speed increase over the less rough SHS is not as large as expected, at least visually; however, the largest change in velocity for a friction reducing surface, when compared to a smooth-wall, occurs in the viscous sublayer, which could not be measured with the current PIV setup. Alternatively, if the roughness elements are sufficiently large to extend into or beyond the viscous sublayer, roughness effects will become significant. This is seen with surface #2 and its rougher variant, which in a mean sense (based on k) do not have roughness features extending beyond the viscous sublayer; however, they do have very large asperity roughness features measuring 100 to 200 μm across (a result of the fabrication method) that do protrude well-beyond the buffer layer, typically defined as $5\delta_\nu$ to $70\delta_\nu$ (*Schlichting and Gersten*, 2003). These very large asperity features, which can be numerous, may explain the significant slowing of the flow velocity at the rougher SHS surfaces, despite the surfaces maintaining a non-dimensional roughness less than the height of the viscous sublayer, and as such are

not hydrodynamically-smooth.

The average wall shear stress, calculated from the streamwise pressure gradient [as shown in (3.2)], for one smooth baseline and a second baseline or each SHS is shown in *figure* 4.2. The skin-friction correlation provided by *Zanoun et al.* (2009) is used to calculate a reference wall shear stress, which is also shown in *figure* 4.2. The results show a decrease in the average wall shear stress for Surfaces #2b (smoother), #3, and #4. Surface #4 is able to sustain a reduced wall-shear stress for the largest range of Re_H, extending to 37,000, while the smoother variation of Surface #2 (Surface #2b) provides the most significant reduction in shear stress for $9,000 < Re_H < 17,000$. As expected, the SHSs that triggered a reduced velocity near the wall, Surface #1, #2, and #2a (rougher) showed a significant increase in shear stress.

Figure 4.3 and 4.4 show the measured skin-friction coefficients graphed as a function of Re_H for the hydrodynamically-smooth baseline and each SHS. The figures present the measured reduction (or increase) in skin-friction due to the presence of only one SHS and one hydrodynamically-smooth baseline. The factor of two in (3.7) arises as only one of the two channel walls is a SHS. This is equivalently the local skin-friction drag reduction on the SHS, whereas dP/dx is the average pressure drop along the channel with one SHS surface and one hydrodynamically-smooth surface. A similar scaling was observed by *Daniello et al.* (2009) using micro-fabricated parallel ridges (*Daniello et al.*, 2009). They observed approximately 25% drag reduction in their channel using one SHS and one smooth plate, and approximately 50% drag reduction in their channel using two SHSs. However, we note that the wall shear stresses measured here, for which drag reduction is still observed, are an order of magnitude greater than that of *Daniello et al.* (2009). The friction on the two sidewalls is neglected due to their small areas and negligible influence on the mean flow properties at the center of the channel (*Schultz and Flack*, 2013; *Zanoun et al.*, 2009). Moreover, local wall shear stress along the top wall of the channel is derived
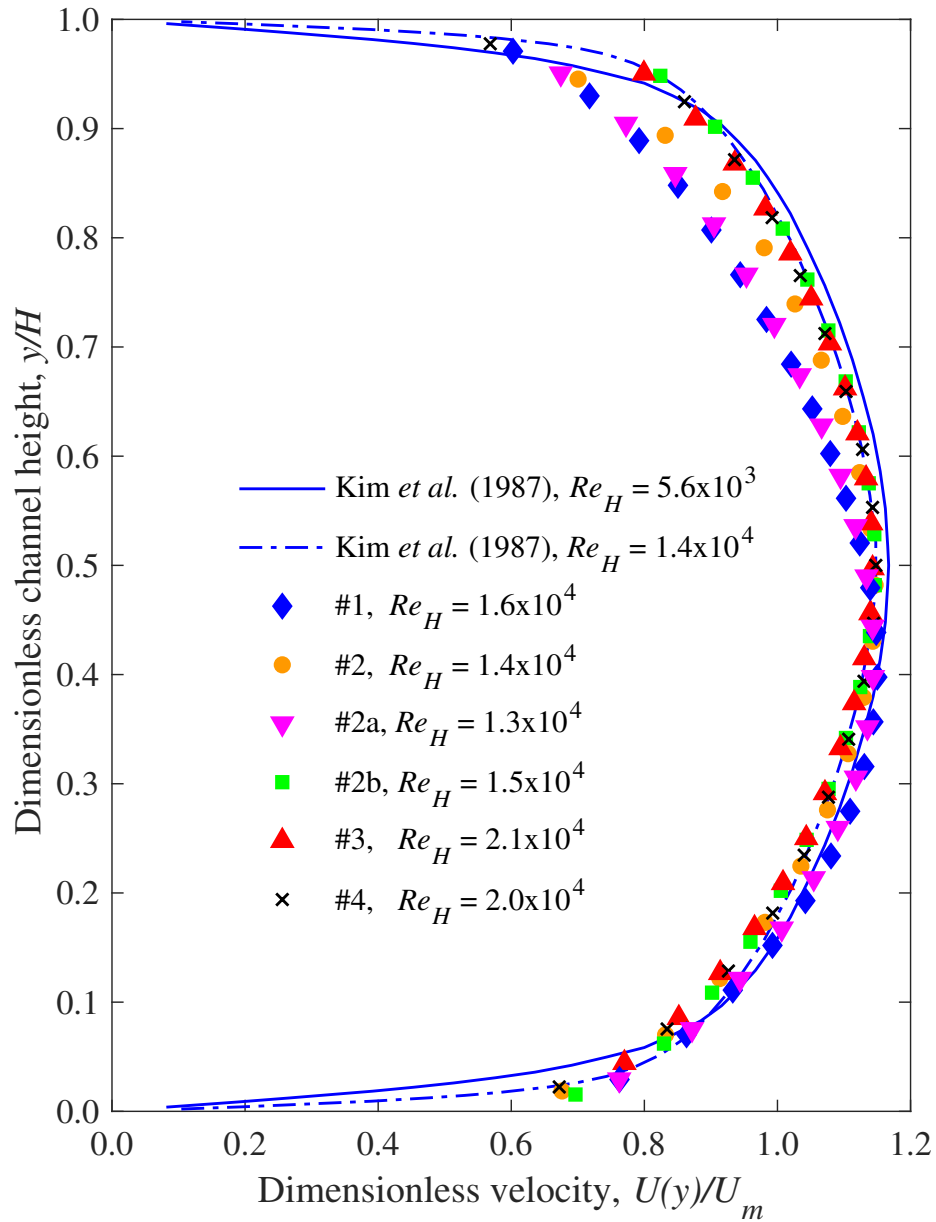
Figure 4.1: Mean velocity profiles for flow between one hydrodynamically-smooth baseline ($y/H = 0$) and each SHS ($y/H = 1$) investigated in this study. DNS data for *Kim et al.* (1987) $Re_H = 5.6 \times 10^3$, and $Re_H = 1.4 \times 10^4$ are provided for reference.
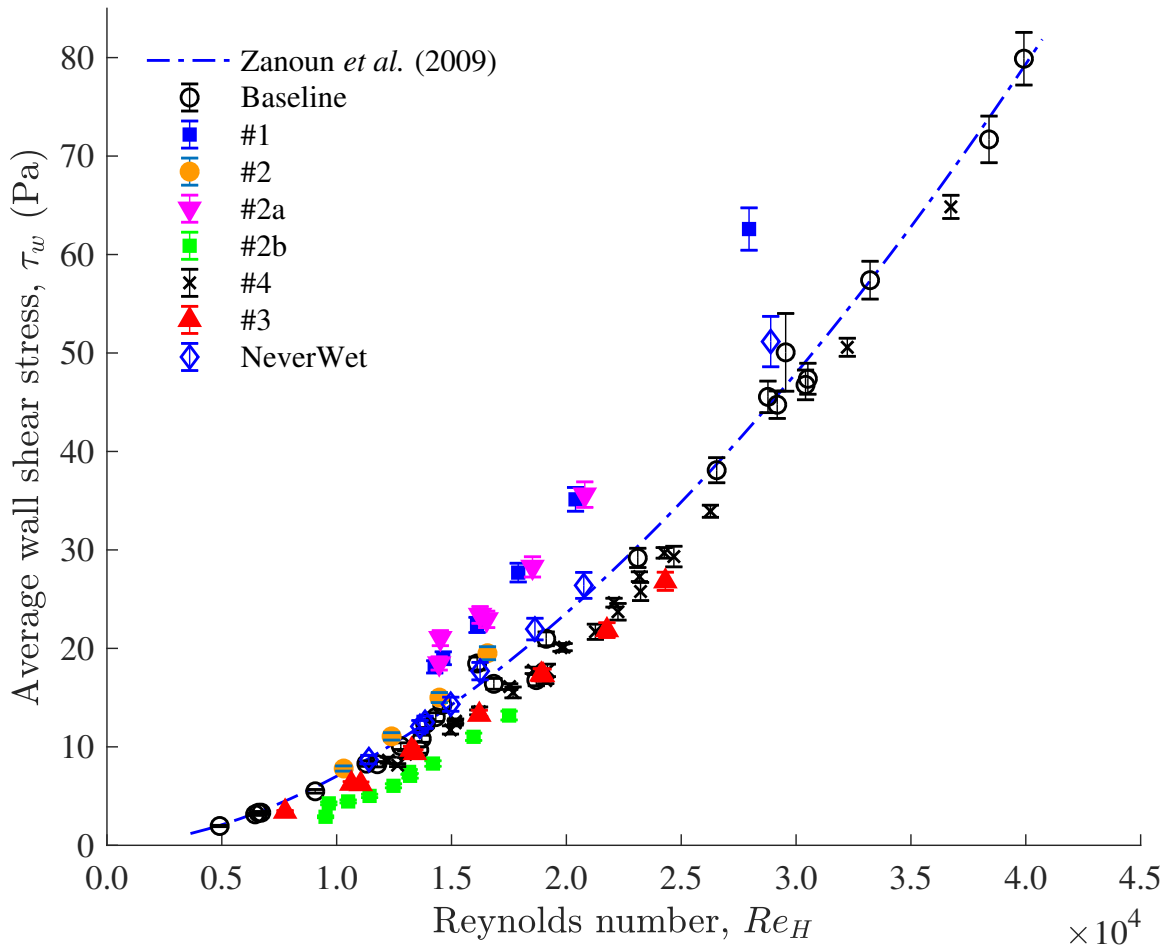
Figure 4.2: Average wall shear stress calculated from the measured streamwise pressure gradient over the hydrodynamically-smooth baseline and each SHS. Expected wall-shear stress calculated using (3.2), and the refined-C_f scaling for turbulent channel flow provided by *Zanoun et al.* (2009), as shown in (3.5), is provided for reference. Variation in the wall-shear is due to the presence of only one SHS; two SHSs are expected to provide roughly $2\times$ the reduction shown.

from a simple control volume, constructed along the fully-developed, two-dimensional flow region in the center of the channel. A linear momentum analysis of this control volume indicated that shear on the side-walls is negligible. Although including the side-wall shear would provide a better idea of the overall frictional loss through the duct, this differs from the local shear along the SHS and would not be pertinent for turbulence scaling arguments.

Surfaces #1 (*figure* 4.3) and the rough variant #2 (*figure* 4.4) show the greatest increase over baseline and have the largest superhydrophobic element makeup with a $k^+ > 1$, and the largest solid-liquid areal fraction at $\phi_s \geq 0.10$. Additionally, the measured skin-friction shows a strong dependence on Reynolds number. For the rougher surfaces, the skin-friction increasingly deviates from the historical, smooth friction line with increasing Reynolds number, while smoother surfaces show an increasing reduction in friction to a limited Reynolds number. When that Reynolds number is reached, the friction begins to return to that of a smooth surface. This may suggest that the spacing between features is not optimized, for a given surface, until a threshold Re_H is achieved and the resulting slip length has a more dramatic effect on the flow. *Min and Kim* (2004) used DNS to investigate feature spacing for a Re_H and the effect on skin-friction drag reduction, and found that slip length must be greater than a lower limit to have a noticeable effect on turbulence. Moreover, Min and Kim demonstrated that streamwise slip provides a reduction in skin-friction and weakens turbulence intensities and structures, while spanwise slip increases drag. Consequently, there may also be a relation to the ratio of streamwise to spanwise slip and the effect on skin-friction drag, which implies that streamwise alignment of features may generate additional savings if the Cassie-Baxter state can be maintained. Increases in friction above the historical friction line should continue until the surface becomes fully-rough; a condition that would signify a deviation from the expected dependence on Reynolds number. Although it is not shown here, we hypothesize

the make-up of the current surfaces providing drag reduction will eventually show an increase in friction at higher Reynolds number, at the very least, such that the measured skin-friction matches the baseline. The non-dimensional roughness increases with increasing Reynolds number, and as such, there will be a point where the effect of roughness could outweigh any friction saving due to the presence of slip or the reduction of near-wall turbulence, or the shear stress could physically alter and/or remove the coating.

4.2 RMS Roughness Effects on SHS Skin-Friction

To better understand the effect of SHS roughness on drag reduction in turbulent flow, drag reduction [see (3.7)] versus non-dimensional roughness k^+ is presented in *figure* 4.5. Using the heightmaps discussed in Section 4.5 to calculate k of the unwetted SHSs, in combination with u_τ inferred from the pressure drop measurements, k^+ is determined for this effort. Here it is demonstrated that a drag increase is expected for $k^+ > 1$, and a savings is generally achieved for $k^+ < 1$ with the significant drag reduction only occurring for $k^+ < 0.5$. This seems to suggest that SHSs do not adhere to the general understanding of 'rough' surfaces in turbulent flow.

Conventionally, a surface is considered hydrodynamically smooth when $k^+ \leq 5.0$ (*Schlichting and Gersten*, 2003). Only when $k^+ \geq 60$ is the surface considered fully rough (*White*, 2006). Several researchers have attempted to limit the allowable RMS roughness k of SHSs that are capable of producing turbulent drag reduction. By non-dimensionalizing k with the viscous length scale δ_ν, values of $k^+ = k/\delta_\nu = 0.1$ (*Ünal et al.*, 2012) and 0.5 (*Bidkar et al.*, 2014) have been proposed as limits for SHS drag reduction, while 1.0 (*Schultz and Flack*, 2007) has been proposed as a limit for when traditionally rough surfaces become noticeable. Drag reduction as high as 8% is observed when $k^+ = 0 - 0.95$, and a drag increase of 19% even when k^+ is as low as 0.11 (*figure* 4.14b). This finding is indeed in agreement with
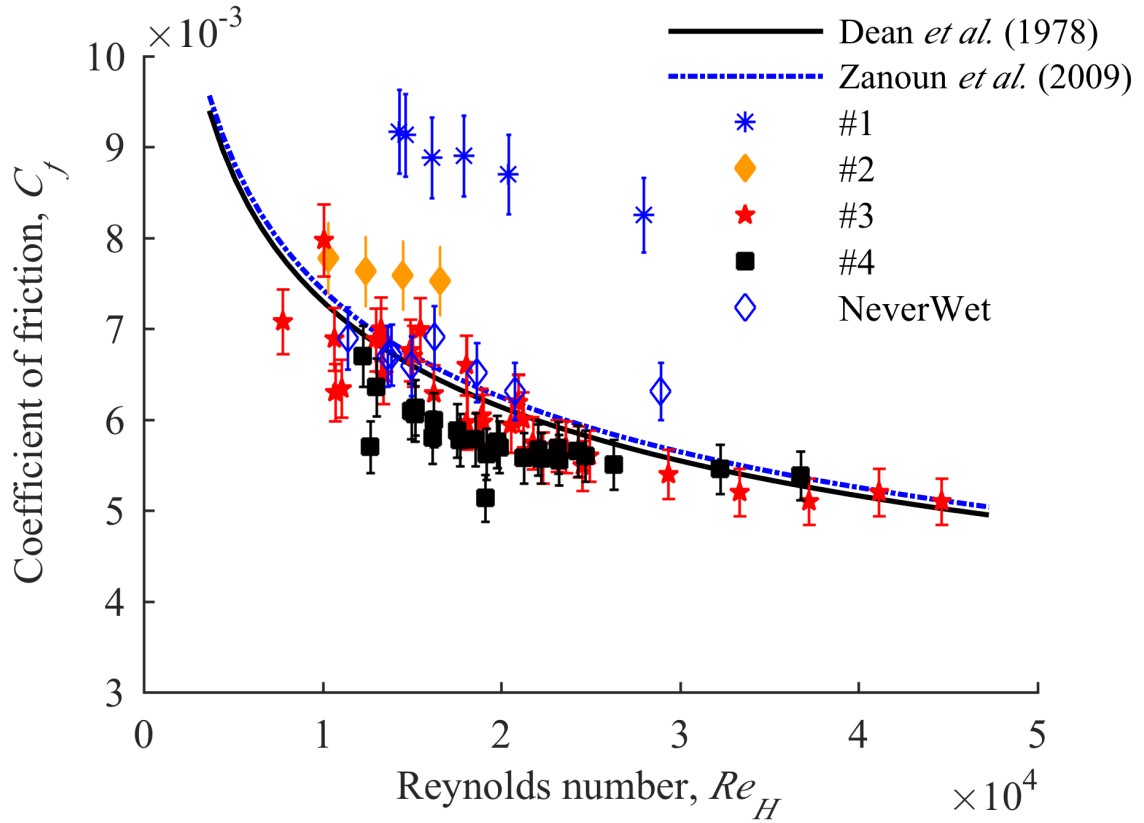
Figure 4.3: Coefficient of skin-friction [see (3.4)] plotted against height-based Reynolds number for the hydrodynamically-smooth baseline and each SHS. Reference correlations by *Zanoun et al.* (2009) and *Dean* (1978), shown in (3.5) and (3.6), are provided. Variation in the skin-friction is due to the presence of only one SHS and one baseline substrate.
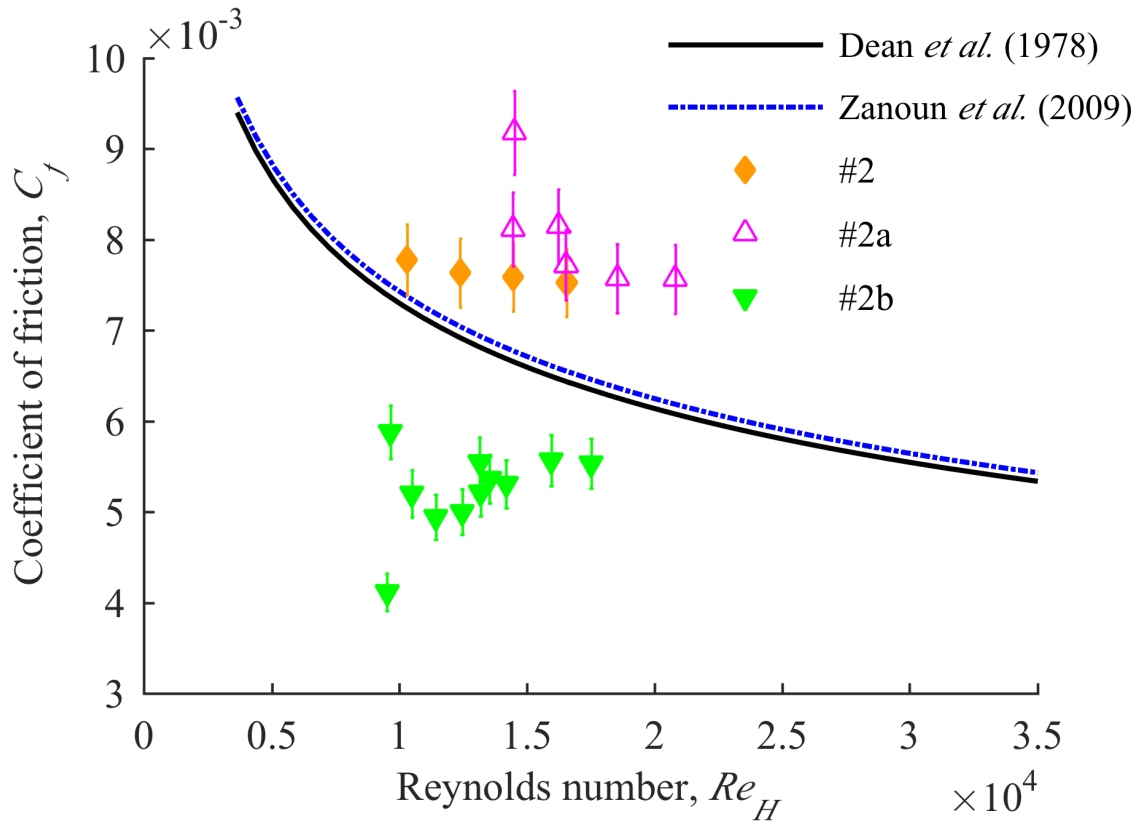
Figure 4.4: Coefficient of skin-friction [see (3.4)] plotted against height-based Reynolds number for the hydrodynamically-smooth and each variant of Surface #2. Reference correlations by *Zanoun et al.* (2009) and *Dean* (1978), shown in (3.5) and (3.6), are provided. Variation in the skin-friction is due to the presence of only one SHS and one baseline substrate.

others' conclusions that the conventional definition of a hydrodynamically smooth surface does not apply to randomly rough SHSs; however, this work demonstrate that k^+ alone cannot be used to determine SHS DR. An additional explanation can be found in the computational work of *Jelly et al.* (2014). In their work, they found that over 70% of the friction on the regions of no-slip (wetted solid surfaces, $r_\phi \phi_s$) was a direct result of the presence of the slip regions (air pockets, $1 - \phi_s$). *Jelly et al.* (2014) attributed the increase in skin-friction to (1) spanwise diffusion of the mean momentum from free-slip to no-slip regions which increases the local skin-friction coefficient on the edges of the no-slip features and (2) a reduction in the drag-reducing capacity of the SHS due to a generation of great velocity fluctuations, i.e. Reynolds stresses. Thus, the deleterious roughness effects of SHSs with $k^+ \geq 1.0$ may be amplified by the entrapped air pockets. Moreover, as *Min and Kim* (2004) have computed, and *Woolford et al.* (2009) has experimentally confirmed, entrapped air pockets that produce spanwise slip unambiguously increase drag. This discussion highlights again that SHS drag reduction cannot be determined based on θ^* and k of a surface alone - more information is needed. And as previously eluded to, the wettability of a SHS at pressure may be the answer.

The surface #2 variations, with identical surface chemistry, but slightly different texture, are expected to produce drastically different resistance due to the presence of different roughness features, as was previously demonstrated in *figure* 4.2. When exposed to flow, the rougher variant of surface #2 significantly increased the wall shear, presumably due to a significant component of form drag. Conversely, the less rough variant of surface #2 produced significant drag reduction. The drag savings measured in the channel were in excess of 60% at lower Reynolds number, and spanned 26% to 90% for the investigated Reynolds numbers ranging from 9,500 to 18,000 (decreased savings with increased speeds). Note that, in this channel flow, for $U_m = 1$ m/s, the mean pressure $P_m \approx 300$ Pa. For $U_m = 5$ m/s, $P_m \approx 9,000$ Pa, highlighting

how increasing Re_H can drastically alter the pressure exerted on the SHS, and in turn, the wetted area of the SHS.

These results further suggest that SHS drag reduction in turbulent flow may also be highly dependent on its state of wetting, beyond that of maintaining the Cassie-Baxter state or transitioning to the Wenzel state, a state at which the near-wall flow would feel the full effect of the roughness. If the Cassie-Baxter state is maintained, the wetted features lying above the entrapped air should have a greater impact on the flow than those lying beneath the air. That is to say, the wetted-area and the height of the wetted roughness elements should dictate drag savings or drag increases at a given flow condition.

4.3   Pressure Effects on SHS Skin-Friction

SHSs are characterized by their high contact angles, which are typically measured using a goniometer with 5 to 50 μL water droplets in atmospheric pressure conditions. The Laplace pressure P_L within a droplet is given by $P_L = 2\gamma_{LG}R^{-1}$, where γ_{LG} is the surface tension of the liquid and R is the radius of the droplet. For a 25 μL droplet, roughly the size used to obtain the values in *table* 2.1, $P_L = 80$ Pa. In the turbulent flow experiments, the pressure exerted on the SHSs evaluated varied between 300 Pa and 20 kPa. To gain insight into the effect such high pressures would have on these SHSs, contact angle of the coatings is also measured using 250 nL droplets ($P_L = 370$ Pa). The results of the two measurement techniques are shown in *figure* 4.6, where higher pressure data for surface characterization is obtained using a data fit to the lower pressure contact angle measurements, which range from approximately 100 Pa to 500 Pa and interatively solving the Cassie-Baxter equation [see (2.4)]. Here it is shown that θ^* is reduced by more than 15° for Surfaces #1, #2, the rougher variant of #2, and NeverWet® from the moderate increase in pressure of 290 Pa. Recall from *figures* 4.3 and 4.4 that these SHSs showed an increase in friction, which also
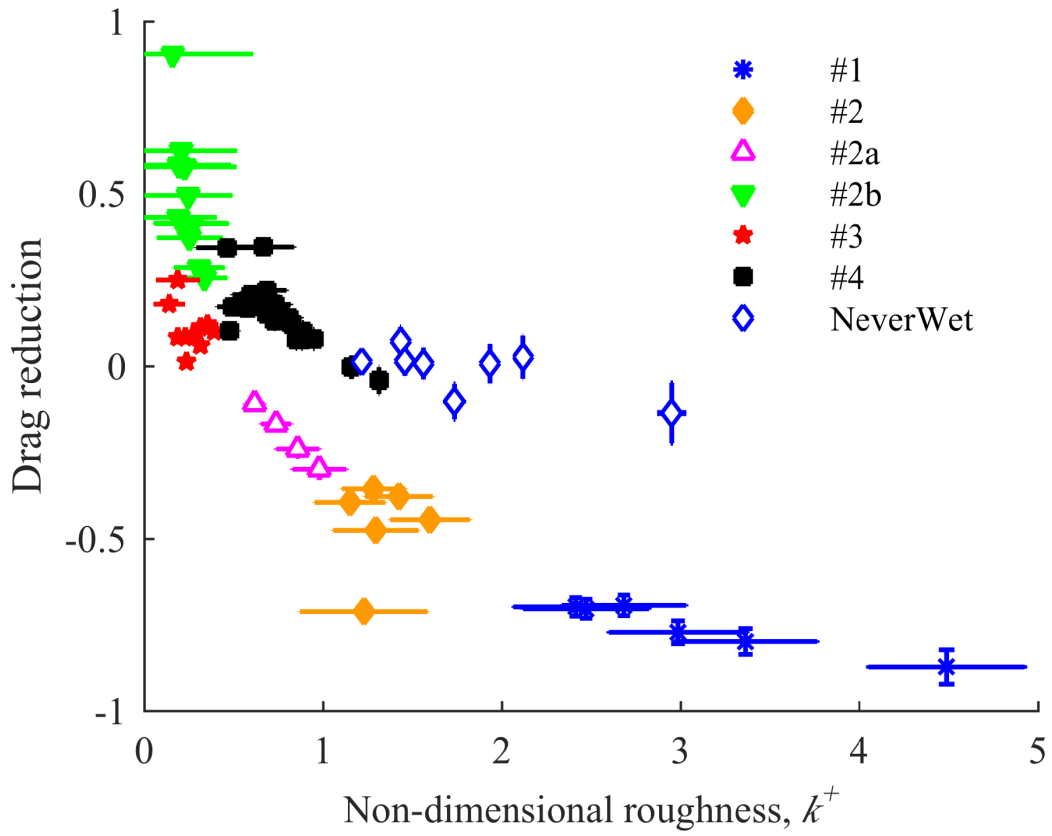
Figure 4.5: Drag reduction [see (3.7)] plotted against non-dimensional roughness k^+. It is evident from the figure that another physical parameter is needed to fully collapse these data. Nevertheless, the data show that no drag reduction is achieved with $k^+ > 1$, and significant drag reduction is only achieved when $k^+ < 0.5$.

increased with Re_H. The change in facility pressure is due to an increase in flow speed and the resulting increase in friction, which requires a higher test section inlet pressure to move the water across the surface.

Regularly defined surfaces, such as the ridges and posts evaluated previously (*Henoch et al.*, 2006; *Daniello et al.*, 2009; *Peguero and Breuer*, 2009; *Woolford et al.*, 2009; *Jung and Bhushan*, 2010; *Park et al.*, 2014), exist in essentially only two states (*Bartolo et al.*, 2006). When non-wetted, (2.4) is valid and ϕ_s remains constant until the surface becomes fully-wetted, where (2.3) then applies and $\phi_s = 1.0$. For the irregular surfaces fabricated in this effort, pressure reduces θ^*, which by (2.4), necessitates a decrease in ϕ_s. For example, even for Surface #3, the most pressure-resistant surface evaluated (*figure* 3.4), large changes in θ^* are realized for the higher pressure measurements. 34% drag reduction was measured on Surface #3 at $Re_H \approx 13,000$ but no drag reduction is observed at the higher speeds tested, $Re_H > 35,000$. Using the measured heightmaps constructed to evaluate the surface, the Cassie-Baxter relation can be solved to find the solid fraction at the pressure experienced at these test conditions, $\phi_s = 0.28$ [*figure* 4.6 (b)] and $\phi_s = 0.56$ [*figure* 4.6 (c)]. Thus, this demonstrates that the observed loss of drag reduction with increasing Reynolds number could be due the change in solid fraction, due to the increased facility pressure, resulting from the increased pumping requirements, at higher flow speeds. Additional details of the high-pressure surface characterization is presented in Section 4.5.

4.4 Effect of Wetted Roughness Height on SHS Skin-Friction Reduction

To further investigate the effects of roughness and pressure on SHS drag reduction, which to the best of our knowledge has never been investigated, we attempt to determine a wetted elemental height in the flow. If one considers regular structures
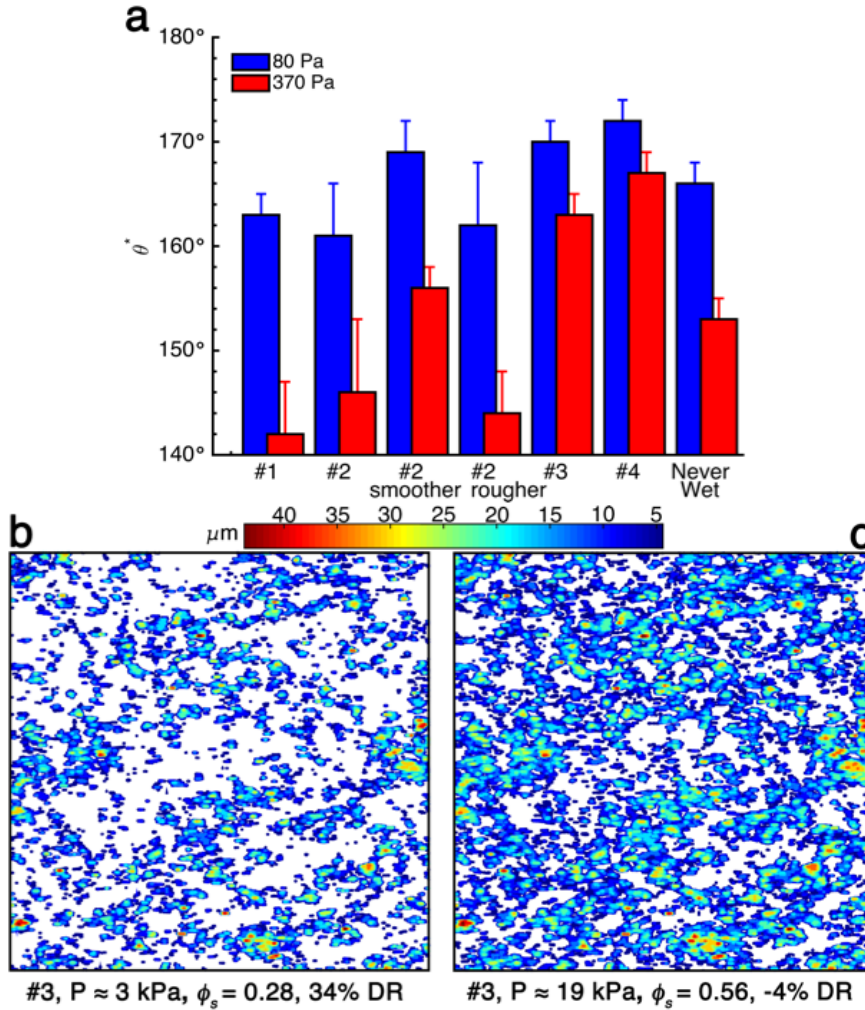
Figure 4.6: (a) Apparent contact angles of the seven SHSs tested, measured at two different pressures. (b) A contour map of the meniscus of Surface #3, at the labeled test condition. White regions represent an air-water interface at an 3kPa inlet pressure of the facility. (c) The same surface, tested at a much higher pressure and higher speed, shows a marked difference in ϕ_s. At this test condition, a drag increase is observed. The scan areas are 2.5 × 2.5 mm and the corresponding contact angles are 149° and 136° for (b) and (c) respectively.

like ridges or posts, the height of these structures directly determines the wetted height, but has essentially no effect on the drag reduction, which is controlled by ϕ_s. Thus, ridges or posts with $k^+ \gg 1$ can probably still reduce drag significantly, if the Cassie-Baxter state is maintained and flow does not feel the presence of the structures beneath the liquid-gas interface. However, for irregular surfaces, it is shown that changes in pressure result in changes in ϕ_s. The only way to alter ϕ_s is by wetting additional SHS features that were not wetted at lower pressures. This means that the effective roughness that the flow sees has changed, and is designated the wetted roughness height k_{eff}. In *figure* 4.7, k_{eff} is plotted versus ϕ_s, which can be determined by iterating though all possible menisci heights. From the values of ϕ_s given in *table* 2.1, all seven surfaces have a k_{eff} well below the length of the viscous sublayer and considerably less than their roughness k. But this is a low-pressure measurement. It may be more important to design a SHS that maintains a moderate ϕ_s at higher pressure, rather than an ultra-low ϕ_s, measured at low pressure. For example, *Daniello et al.* (2009) has shown that 50% drag reduction is possible even for ridges with $\phi_s = 0.5$.

Since the seminal work of *Nikuradse* (1933), flow over rough surfaces has been thoroughly investigated. In this work, a strong correlation is found between size of the roughness k and the resulting friction and velocity distributions in pipes. In a recent review, *Flack and Schultz* (2010) propose that an effective sand-grain roughness can be correlated directly to a generic roughness using

$$k_s \approx 4.43 k_{RMS} \left(1 + S_{sk}\right)^{1.37} \tag{4.1}$$

where S_{sk} is the skewness of the surface profile. Here this is applied to these SHSs to further explore the role of roughness in SHS drag reduction. The two-dimensional equivalent is used, for which the skewness is given by
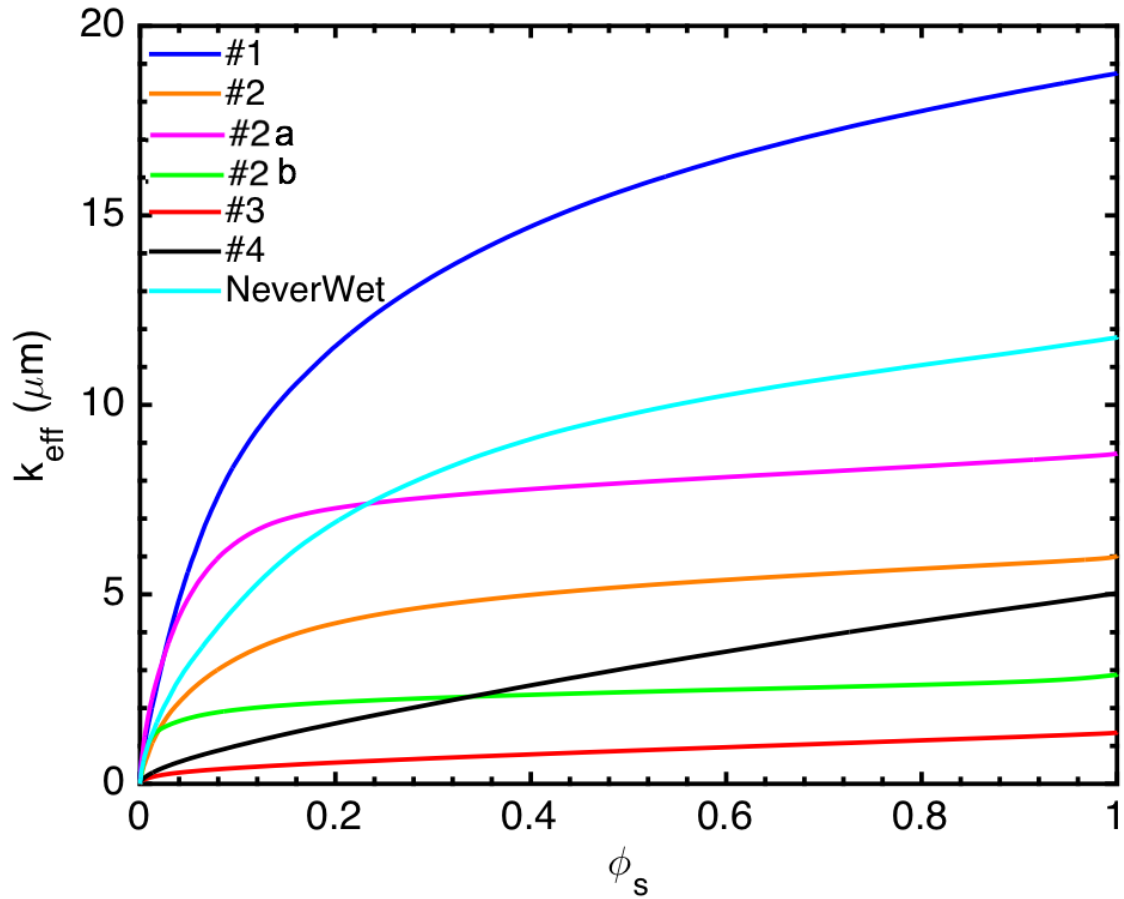
Figure 4.7: The effective root-mean-square roughness of each SHS as a function of the solid fraction. When fully-wetted, $k_{eff} = k$. Note that most SHS exhibit $\phi_s \leq 0.10$, making the roughness that the flow sees drastically different than the fully-wetted roughness, for certain SHSs.

$$S_{sk} = \frac{1}{S_q} \left(\frac{1}{A} \iint\limits_{A} Z^3(x,y)\, dx dy \right) \tag{4.2}$$

where S_q is again equal to k, A is the scan area, and Z is the height at point (x, y). The observed drag versus the non-dimensionalized equivalent sandgrain roughness of these surfaces is presented in *figure* 4.8. Drag reduction is essentially never observed when $k_s^+ \geq 20$. A similar scaling is observed as with k^+ (see *figure* 4.5), except that Surfaces #3 and #4 warrant comment. Both these surfaces achieve their non-wetting state mostly through nano-scale texture (see *figures* 3.4 and 3.5). The other four surfaces exhibit micro-scale features, and NeverWet®appears to be a of hybrid of nano- and micro-texture. The achievable slip length for SHSs depends on the spacing between features, so Surfaces #3 and #4 could possess smaller slip lengths. Also, looking back at *figure* 4.3, Surfaces #3 and #4 were tested at much higher Reynolds numbers, and consequently much higher pressures. Note also that here the k used is for the fully-wetted surface, whereas, as previously stated above, the k_{eff} may be significantly less for some SHSs.

The authors acknowledge that the roughness correlation used by *Flack and Schultz* (2010) was intended for surfaces that are in the hydraulically rough regime. Nevertheless, as the surfaces investigated here showed some indication of having significant roughness effects, use of this established method to explore the impact of SHS roughness and skewness was warranted. The analysis provided some evidence that the roughness features of the SHS presented here were indeed not impacting the flow as a fully-rough surface, which is an important aspect to note.
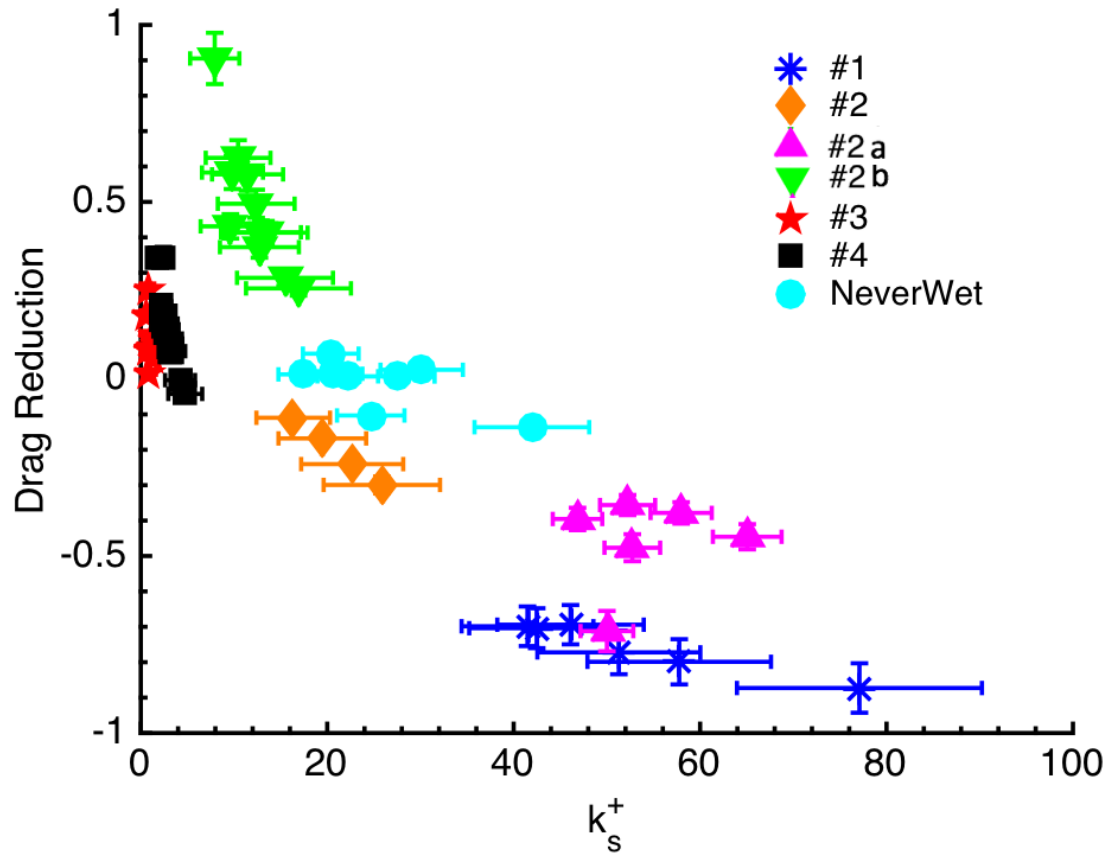
Figure 4.8: The measured drag reduction on a SHS as a function of the non-dimensionalized equivalent sandgrain roughness.

4.5 A Novel Surface Wettability Characterization Technique for SHS Resistance Estimation

To this point we have highlighted that both roughness and wettabililty of a SHS are important aspects for drag reduction in turbulent flow. Moreover, we have shown that the local mean total pressure in the flow can drastically alter these parameters. As such, we suggest that SHSs should be characterized using mean pressures relevant to the flows in which they will be evaluated for drag reduction, as opposed to the typical ambient pressure measurements and that the results can be used to predict the preformance of the SHSs in turbulent flow. We note that these pressures do not account for the pressure fluctuation experienced in a turbulent boundary lay, an effect which could effect these results.

As shown in *table* 2.1, authors of the previous studies may not have reported the contact angles of the SHSs examined, or they only reported a static apparent contact angle, with no measure of contact angle hysteresis. From a materials design standpoint, there are few guidelines regarding how surfaces should be fabricated so as to maximize the drag reducing potential of a SHS in turbulence. Generally in the literature, reporting θ^*_{adv} and θ^*_{rec} at ambient pressure has been considered sufficient to describe a SHS. However, here it is shown that characterization of these angles at ambient pressure, while necessary, may not be sufficient to identify surfaces capable of reducing drag in turbulent flow. Fully-turbulent, high-Reynolds number flows create large pressure fluctuations and high shear stresses. Such large surface pressures can displace the entrapped air pockets of a SHS if its capillary resistance is low, i.e. only a small pressure is required to transition from the non-wetted Cassie-Baxter state to the fully wetted Wenzel state. Similarly, the high shear stresses can mechanically damage and detach any fragile texture elements of the SHS, again removing the entrapped air. Insufficient mechanical durability is one reason SHSs have previously not shown

sustainable friction reduction in turbulent flow (*Bidkar et al.*, 2014; *Zhao et al.*, 2007; *Aljallis et al.*, 2013; *Srinivasan et al.*, 2013; *Ling et al.*, 2016). Regardless, even if the air remains within the interstices of a SHS, the surface may not reduce drag if the texture is not of the correct morphology and scale (*Bidkar et al.*, 2014; *Zhao et al.*, 2007), as is explained below.

As the liquid pressure increases on a SHS, the liquid-vapor interface moves downwards into the air pockets, partially filling the surface texture, thereby increasing ϕ_s and possibly also r_ϕ, depending on the surface geometry. Using heightmaps of the surface and θ^* data at varying pressure, it is possible to iteratively solve for $r_\phi\phi_s$ using (2.4), calculate the meniscus height corresponding to that wetted area, and then solve for ϕ_s and r_ϕ independently using the known surface morphology. An example of such results are shown in *figure* 4.9. The heightmaps are collected with an Olympus LEXT OLS4000 laser measuring microscope with a Z step size of 1.25 μm, an overall scan area of 2.5 mm $\times$ 2.5 mm, and an XY resolution of 1.25 μm $\times$ 1.25 μm. A minimum of three locations are imaged per sample. Contact angles are measured using a Ramé-Hart 200 F1 contact angle goniometer with water droplets of varying volumes. Dynamic contact angles and contact angle hysteresis are measured via the conventional low-pressure sessile drop method, by increasing or decreasing the volume of a water droplet contacting the surface while attached to a microsyringe tip. Droplet volumes ranged from 10-20 μL for this technique. By decreasing the size of the droplet used to measure contact angles, θ^* at elevated pressures may be measured. As previously discussed, the Laplace pressure, P_L, within an azimuthally symmetric water droplet is given by $P_L = 2\gamma/R$ where γ is the surface tension of water and R is the radius of the droplet. For a 250 nL droplet, $P_L \approx 370$ Pa. The higher-pressure static contact angles on the four SHSs spanned a range of 20°, indicating a disparate response to applied pressure, as seen in *figure* 4.10. Although the pressure range of this method is severly limited by the minimum drop size that may be deposited and

57
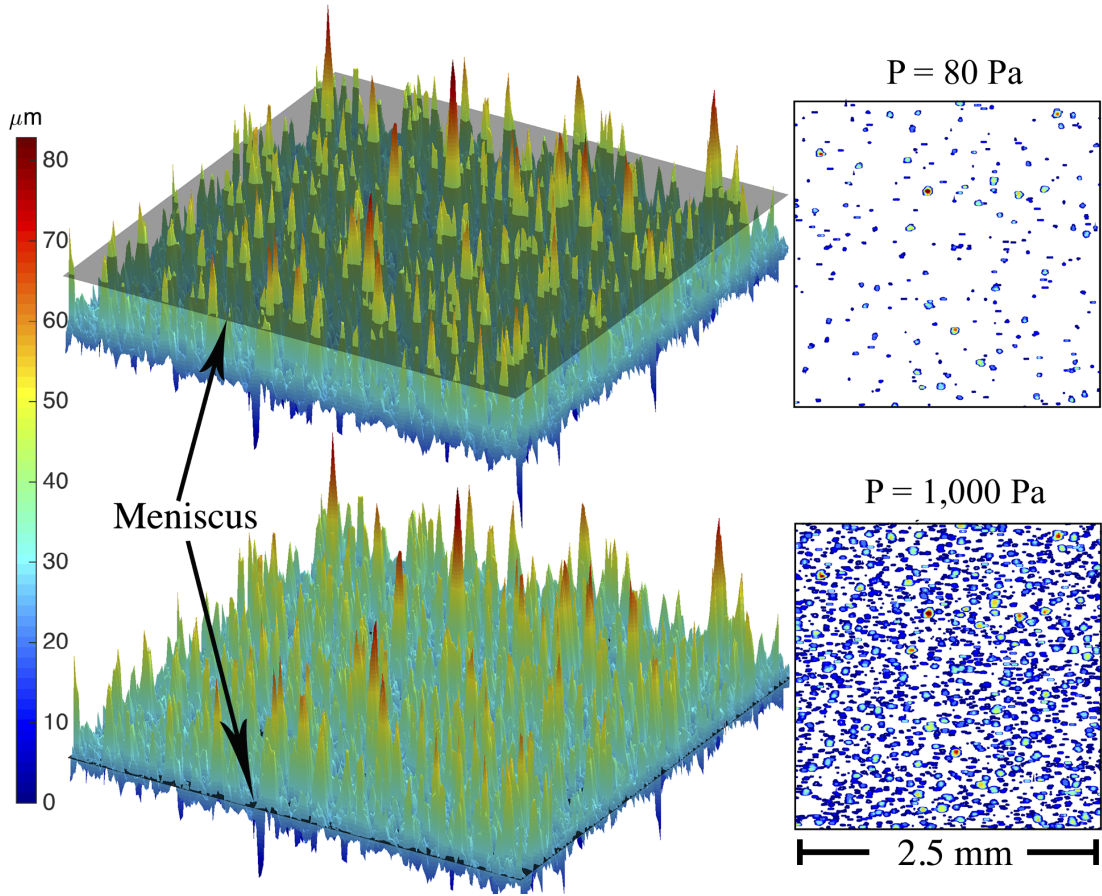
Figure 4.9: The measured static apparent contact angle of a droplet may be used to calculate the wetted area fraction $r_\phi \phi_s$ using (2.4). This experimental $r_\phi \phi_s$ is then used to determine the meniscus height, and subsequently, the geometry of wetted asperities, by using a heightmap of the surface texture. These are computed for varying hydrostatic pressures by using measured θ^* of droplets with varying volume and Laplace pressure as shown in *figure* 4.10. This also allows extrapolation to pressures greater that can be measured with goniometry, as the droplet volume becomes impractically small. Here we show a height map of Surface #2, collected with an Olympus LEXT OLS4000 laser measuring microscope with a Z step size of 1.25 μm, an overall scan area of 2.5 mm $\times$ 2.5 mm, and an XY resolution of 1.25 μm $\times$ 1.25 μm. Superimposed on the upper heightmap is the air-water interface at low pressure, which is conventionally used to measure contact angle. The air-water interface at high pressure shown on the bottom heightmap may be expected in turbulent flow conditions. Figure reprinted from *Gose et al.* (2017b).

measured, contact angles at higher pressures and Reynolds numbers may be extrapolated with a power law fit to the data, as shown in *figure* 4.11. The range of mean pressures P_m experienced in this study is approximately 300 Pa to 9,000 Pa, linearly varying with a nominally zero outlet pressure at the downstream end of the SHSs. Additionally, the variation of $r_\phi \phi_s$ with pressure is shown in *figure* 4.12 as a power law fit to the experimental data. This pressure-Reynolds number relation is specific to the facility in this analysis; however, the a similar increase in pressure with increasing *Re* should be expected for other facilities.

According to (2.4), θ^* must decrease with the increased wetted area at increased pressures, as shown in *figure* 4.10. This has two critical implications. First, the projected wetted area ϕ_s calculated from conventional measurements of θ^* may be significantly different from the ϕ_s in a turbulent flow at elevated pressures, depending on the pressure resistance of the texture. Second, the wetted asperities that protrude into the flow, as characterized by the wetted roughness r_ϕ, may cause form drag (*Bidkar et al.*, 2014; *Leonardi et al.*, 2007; *Leonardi and Castro*, 2010; *Xie and Castro*, 2006; *Kanda et al.*, 2004), increase turbulent mixing, and/or enhance turbulent structures (*White*, 2006) that may negate any skin-friction drag reduction, resulting in a net increase in drag. A significant decrease in θ^* with elevated pressure necessarily indicates an increase in $r_\phi \phi_s$, and equivalently, an increase in the number and size of texture elements protruding into the flow. In short, a surface that exhibits a large decrease in θ^* with increasing pressure will exhibit an increase in form drag in turbulent flow. It is therefore important to characterize the wetted area of the surface at the pressures expected during turbulent flow to accurately predict turbulent skin-friction drag reduction.

Using these measurements, we can then estimate the contribution of form drag by the wetted roughness as a means of determining if a rough surface is expected to cause a drag increase when compared to a smooth baseline. As form drag is not
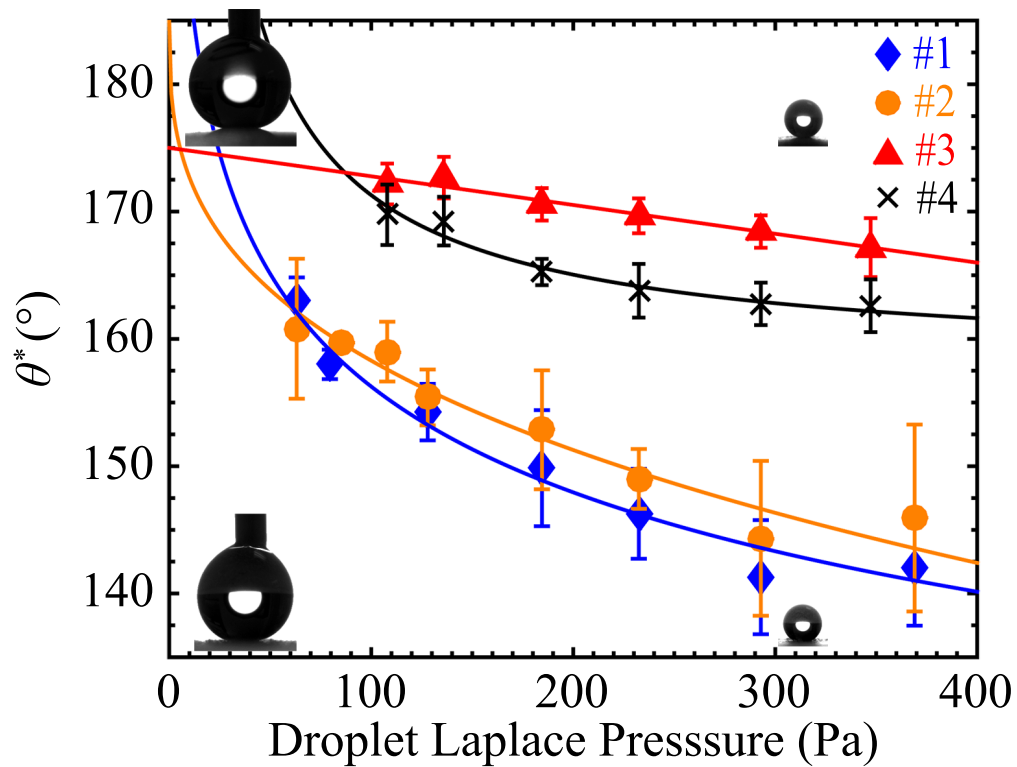
Figure 4.10: The apparent contact angle θ^* as a function of pressure for the four surfaces considered in this work, as measured using drops of varying volume and Laplace pressure. The curves are power law fits to the data. The insets show goniometer images of droplets on Surfaces #1 (below) and #3 (above). Figure reprinted from *Gose et al.* (2017b).
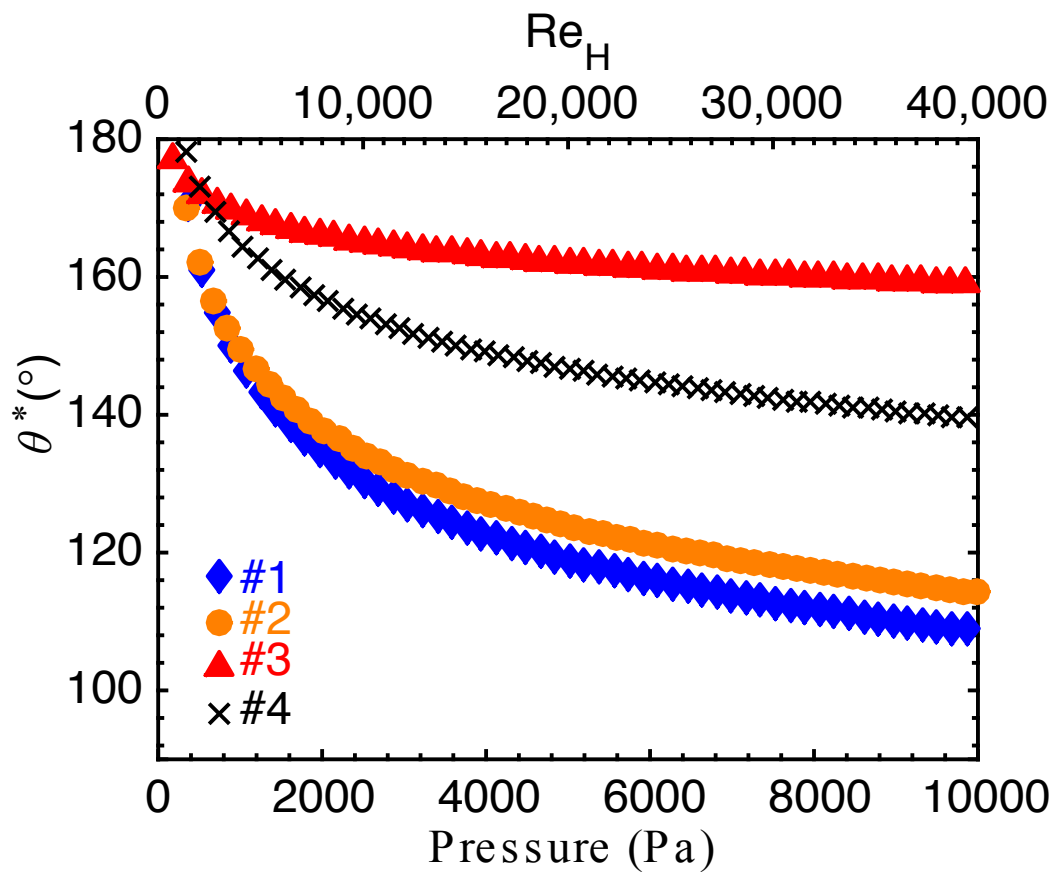
Figure 4.11: The expected measured apparent contact angle θ^* as a function of pressure and the corresponding height-based Reynolds number Re_H of the experimental flow facility (shown in *figure* 3.6 and discussed in *Section* 3.2) for the four surfaces considered in this work. The quantities presented are extrapolated from a power law fit to the experimental contact angle data in *figure* 4.10. Figure reprinted from *Gose et al.* (2017b).
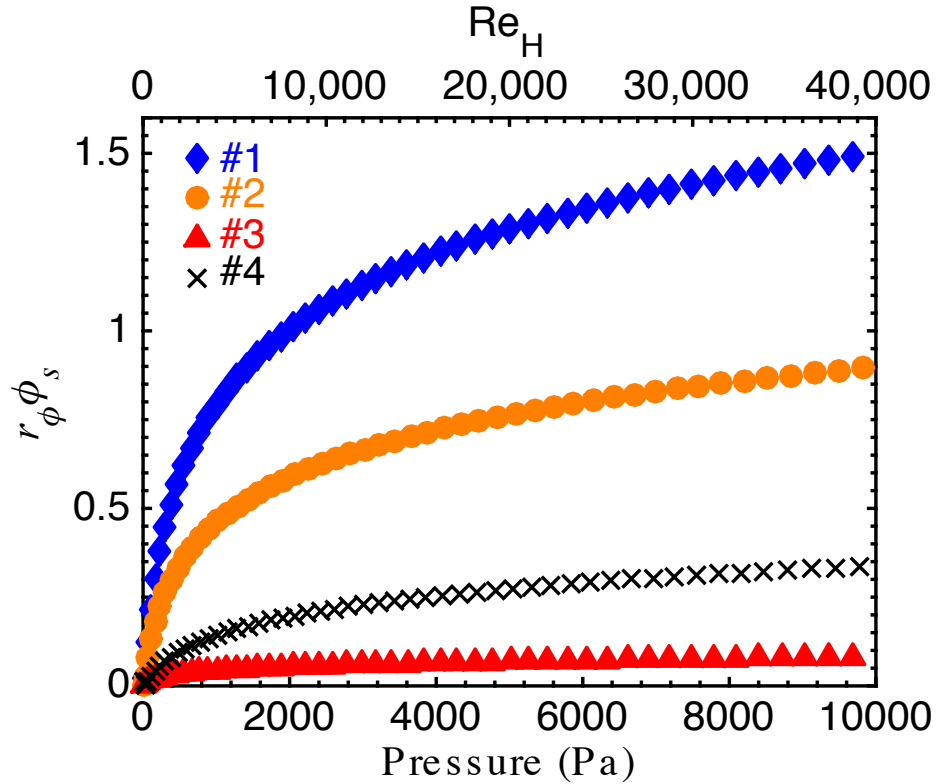
Figure 4.12: The expected variation of $r_\phi \phi_s$ as a function of pressure and the corresponding height-based Reynolds number Re_H of the experimental flow facility (shown in *figure* 3.6 and discussed in *Section* 3.2) for the four surfaces considered in this work. The quantities presented are extrapolated from a power law fit to the experimental contact angle data in *figure* 4.10. Figure reprinted from *Gose et al.* (2017b).

important for a hydrodynamically-smooth plate (RMS roughness $<$ 1μm for the present study), an estimate is made to see whether an expected increase in resistance over the skin-friction, i.e. if there are sufficient texture elements protruding above the heterogeneous three-phase interface to increase the power required to move water over the surface at a predetermined speed. Using the heightmap and meniscus height, and the geometry of each wetted texture element (using the method presented and *figure* 4.9), the form drag on each texture element is approximated by the following equation (*White*, 2006)

$$F_{Di} = \frac{1}{2}\rho U_i^2 A_i C_D \tag{4.3}$$

where ρ is the density of water, U_i is the average flow speed in the vicinity of each texture element, A_i is the element's projected area in the flow direction, and C_D is the drag coefficient based on the geometry of each element. In this analysis, the wetted geometry is determined using the high-pressure contact angle measurements and the measured geometry of the surface. Thus, for a given mean flow speed and pressure, the number of wetted elements and their area projected normal to the flow is known. We assume that U is equal to the flow speed that would occur at the one-half height of each element in the viscous sublayer. Admittedly, this is a gross assumption, especially in the presence of slip. Nevertheless, acknowledging the velocity in the viscous sublayer can be related to the height above the surface ($u^+ = y^+$, where u^+ is the local flow speed non-dimensionalized by the friction velocity, i.e. $u(y)/u_\tau$ and y^+ is the inner variable coordinate above the surface non-dimensionalized by the friction velocity and kinematic viscosity, i.e. $y^+ = yu_\tau/\nu$, where u_τ is as defined in *Section* 3.2), an approximation of the flow speed at each element is reached. The last step is to determine C_D for the roughness elements, which based on their shape is assumed to most closely match the C_D of a triangular roughness element, or $C_D \approx 1.0$. It should be stated that this analysis should only be used to evaluate if a net increase or a

potential reduction is possible, based on the known flow conditions and the measured rough surface topology.

On a SHS, if the sum of the forces due to form drag on each of the protruding texture elements exceeds the drag reduction due to the presence of the trapped air pockets, a net drag increase will result. This drag increase is a direct consequence of the meniscus height at pressure, and is independent of the θ^*_{adv} or θ^*_{rec} measured at low/atmospheric pressure. Computationally it has been shown that surfaces with $\phi_s \approx 0.1$ exhibit the highest form drag in the fully wetted case (*Leonardi and Castro*, 2010; *Kanda et al.*, 2004). Moreover, the largest texture elements produce disproportionately high form drag (*Leonardi et al.*, 2007; *Xie et al.*, 2008). As such, designing SHSs that will not cause significant form drag in turbulent flow is non-trivial and has rarely been investigated (*Bidkar et al.*, 2014; *Vajdi Hokmabad and Ghaemi*, 2016). The dynamics of the gas-liquid interfaces on the SHS will also play a significant role in how the wetted surface textures may be exposed to the flow under changing flow pressure. This, in turn, is related to the contact angle hysteresis of the SHS, measured at higher pressure. For higher pressure $\Delta\theta$ measurements, low volume (250 nL to 6 μL) droplets are deposited onto the SHSs using a micropipette. The surface is then tilted on the goniometer until the droplet rolled off, while monitoring the contact angles of the droplet. Here we assume $\theta^*_{adv} = \theta_{max}$ and $\theta^*_{rec} = \theta_{min}$ immediately prior to droplet roll-off.

To be consistent with the wettability analysis discussed here, a slight modification of the notation is made; $C_{T,SHS}$ is used to denote the resistance coefficient for the SHS, which has both skin-friction and an assumed form drag contribution. $C_{f,baseline}$, and correspondingly $C_{T,SHS}$, are inferred from the streamwise pressure gradient dP/dx along one SHS and one baseline hydrodynamically -mooth surface in a fully-developed turbulent flow channel. Additionally, form drag calculations are provided based on the above discussion for comparison. This comparison is shown in *figure* 4.13.
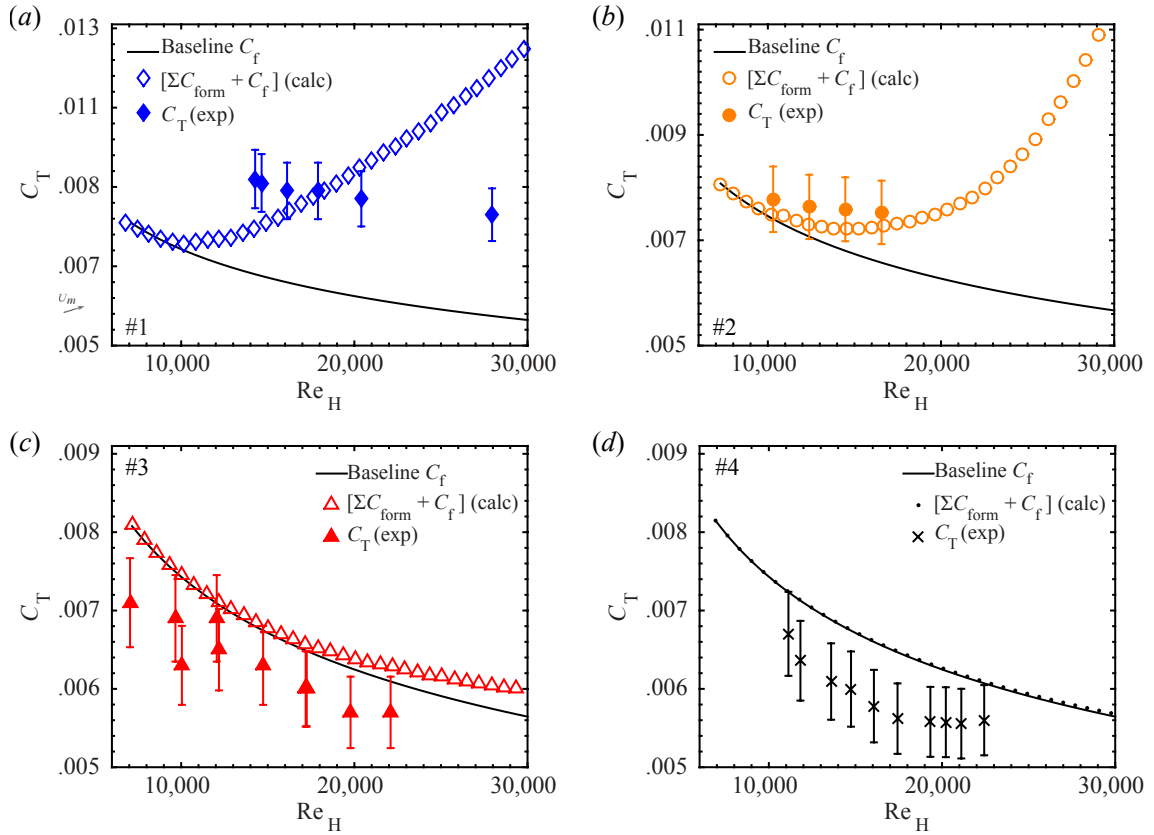
Figure 4.13: Experimental (exp) and calculated (calc) C_T values for Surfaces #1 - #4, denoted as *figures* (*a*) - (*d*). The calculated C_T includes the skin-friction expected for a hydrodynamically smooth flat plate as well as the total form drag due to any asperity roughness. The experimental C_T includes both asperity form drag and the skin-friction drag on the SHS. Therefore, these surfaces may still be producing skin-friction drag reduction locally, but the effect is sometimes mitigated by the overall increase in form drag (Surfaces #1 and #2). Figure reprinted from *Gose et al.* (2017b).

As previously mentioned, C_T for the SHSs as referenced in *figures* 4.13 and 4.14 have contributions from both and is presented as the sum of C_f and a presumed form drag component, denoted as $\sum C_{form} = \sum_{i=1}^{n} C_{Di} = [\sum_{i=1}^{n} F_{Di}/(1/2 \; \rho U_m^2)]$. None of the SHSs were wetted following the high-Re_H flow testing, i.e. there is no loss of entrapped air. However, Surfaces #1 and #2 showed an increase in the wall-shear stress and the overall measured drag coefficient C_T. Thus, although the entrapped air pockets of Surfaces #1 and #2 provided a slip interface, the overall wall shear is increased. On the other hand, Surfaces #3 and #4 showed significant drag reduction, as high as 34% at a Reynolds number of 19,000. For Surfaces #3 and #4, the wall shear is significantly lower than that experienced by a hydrodynamically-smooth baseline. Using our form drag calculations, these results could be anticipated. The drag reduction is both sustainable over hours of continuous high-speed flow ($Re_H \approx 30,000$), and repeatable even after months separating successive runs of the same SHS. To date, in fully-developed turbulence, i.e. where the necessary fluid-flow development length ($> 50H$) requires the fabrication of large surfaces, randomly rough SHSs capable of reducing drag have rarely been evaluated, much less modeled or predicted, using both physical properties of both the surface and flow.

The calculated values of C_T, is defined as the summation of the expected drag on a smooth plate (*Zanoun et al.*, 2009) and any additional form drag caused by the wetted roughness elements of the SHS. In contrast, the measured total drag coefficients are the summation of any form drag due to surface roughness, plus the frictional drag on the mixed slip/no-slip boundary condition SHS, as inferred from the streamwise pressure drop. For SHSs, the latter term could be significantly less than the frictional drag experienced on a smooth, no-slip surface. In this case, our calculated drag coefficients would over-predict the measured drag coefficients, as is observed for Surface #1 and the rougher variant of Surface #2. Thus, deviation between measured and calculated *drag increase* most likely indicates surface slip (which decreases drag) that

66

is mitigated by surface roughness (which increases drag) and a large form drag contribution that should trend towards a value significantly greater than $C_{f,baseline}$ with increasing form drag contributions (C_D is assumed to be 1.0 for the asperity roughness elements). In fact, form drag due to large, sparse ($\phi_s \leq 0.2$) features has been shown to be the major component of total friction for certain texture geometries (*Leonardi et al.*, 2007; *Leonardi and Castro*, 2010; *Xie et al.*, 2008; *Kanda et al.*, 2004). When the form drag did not nullify the decrease in frictional drag due to slip, drag reduction is observed. Some deviation in the calculated and measured C_T is expected as these surfaces can in fact be altered by the fluid flow. Additionally, we have observed that larger, less firmly attached SHS roughness features can be removed from the surface at low water speeds if the particles used in the SHS fabrication are not adequately bonded to the substrate. This artifact may be apparent in the measured resistance of Surfaces #1 and #2 (more rough), where deviation in the measured and calculated values are observed. Moreover, this model is developed and intended to be used as a zeroth-order estimate for the comparison of form to frictional resistance, and other factors may be important.

Additionally, it is found that a surface's contact angle hysteresis, measured at higher pressure $\Delta\theta^{HP}$, helped explicate the increase in resistance for these SHSs. Whereas the conventional measurement of θ^*_{adv} and θ^*_{rec} always resulted in $\Delta\theta < 5°$ for all our surfaces, the higher pressure measurement varied drastically between surfaces that increased or decreased drag. The product of $\Delta\theta^{HP}$ and k^+ collapsed all our drag measurements onto a single curve, as shown in *figure* 4.14c. A similar collapse of the data is observed with the product of k^+ and the wetted solid surface area $r_\phi\phi_s$, as calculated from θ^* of varying drop volumes and heightmap data as described in *figure* 4.9. This is to be expected, as $\Delta\theta^{HP}$ increases with increasing wetted area at elevated pressures. The advantage of the $\Delta\theta^{HP}k^+$ scaling parameter lies in its ease of measurement, as no heightmap data (only k) or computation of the meniscus height

is required. Note that these are empirical scaling laws, and products of other relevant quantities (k, θ^*, θ^*_{adv}, θ^*_{rec}, ϕ_s, etc.) did not produce a collapse of the measured drag reduction.

4.6 Concluding Remarks

In closing, we have fabricated scalable, mechanically robust superhydrophobic surfaces that significantly reduce skin-friction, by more than 50%, in high-speed turbulent flows such as those relevant to many naval applications. This was accomplished by fabricating randomly rough SHSs that minimize the product of the non-dimensional roughness and the contact angle hysteresis measured at higher pressure. Only by considering both the wettability and the flow-dependent characteristics of these SHSs can turbulent drag reduction be achieved. The conventional characterization techniques for SHSs that do not consider the dynamic nature of the micro gas-liquid interfaces and will not predict if or when a randomly rough SHS can produce turbulent drag reduction. We have shown a significant increase in the wetted area of these SHSs at mean pressures realized in turbulent flows. The combination of surface roughness, wetted solid surface area, and the form drag contributions from the heterogeneous, randomly rough surface significantly impact the resulting resistance of flow over a SHS.

Major findings from the internal flow experiments are summarized here:

- Mechanically robust and extremely scalable SHSs have shown up to 50% DR in fully-developed turbulent channel flow for $Re_H \leq$ 40,000

- Form drag on a few large asperities is significant and can negate skin-friction drag reduction

- Large feature size ($k^+ > 1$) results in a net increase or no change in the overall pressure drop through the test section, indicating no drag reduction, which
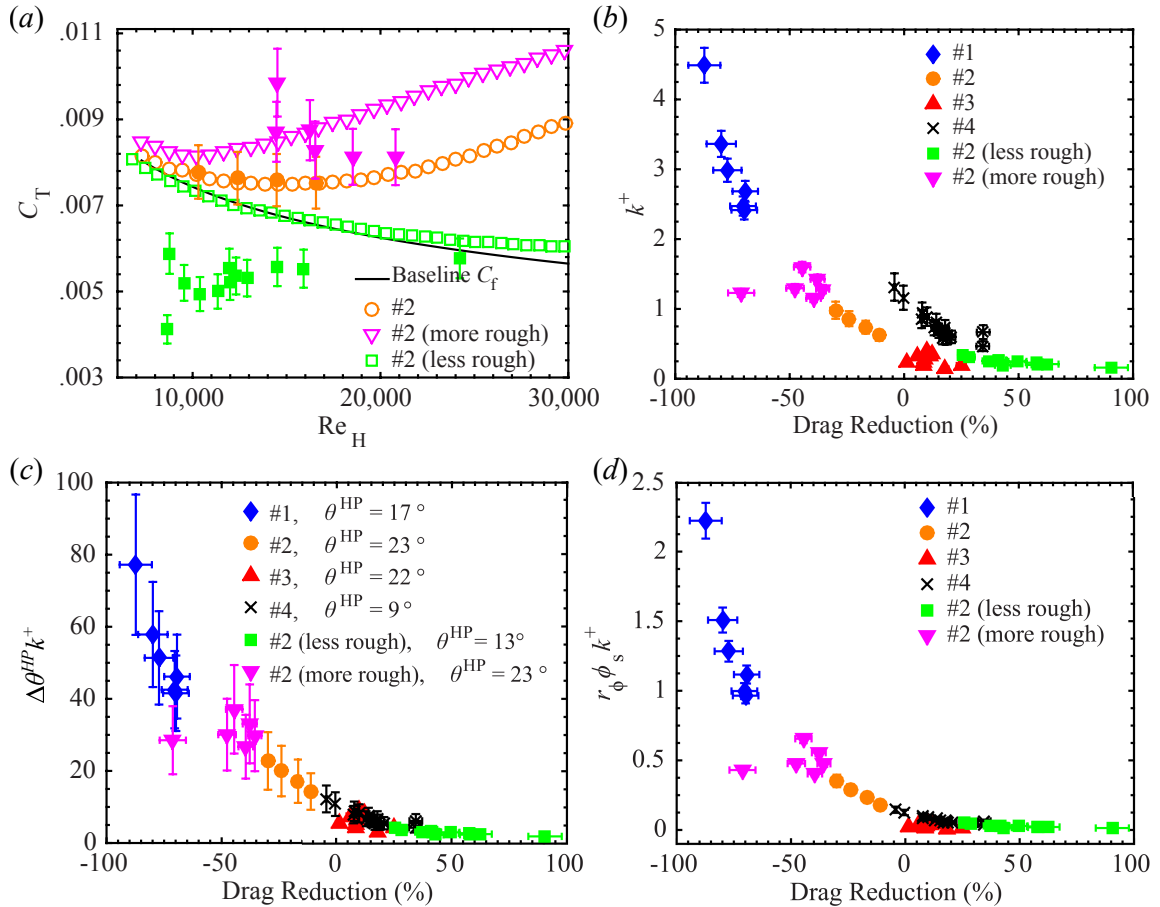
Figure 4.14: The effect of surface roughness. (*a*) three variations of Surface #2, exhibiting either significant form drag, or significant drag reduction. Open symbols are the calculated C_T values and closed symbols are the experimental data. The baseline is for the unmodified Surface #2. (*b*) The drag reduction or increase (negative means drag increase) provided by all the surfaces considered as a function of the non-dimensional roughness. Recall that the drag associated with the smooth baseplate has been removed. (*c-d*) The drag reduction data collapsed onto a single curve when plotted versus the product of the non-dimensional roughness and the higher-pressure contact angle hysteresis (370 Pa for a 250 nL droplet) or $r_\phi \phi_s$. Figure reprinted from *Gose et al.* (2017b).

differs significantly from the traditional understanding of the effects of wall roughness on the a flow

- SHSs with low apparent contact angle $\theta^* < 160°$ and high wetted area under pressure ($\phi_s > 0.10$) usually results in a significant increase in drag

- Small feature size ($k^+ < 1$), large θ^* and a small high-pressure contact angle hysteresis $\Delta\theta^*$ is needed for meaningful drag reduction in turbulent flow over SHSs

CHAPTER V

Technical Approach II: External Turbulent Boundary Layer Flow

SHSs that closely resembled those described in Chapter III were fabricated and spray applied to a polycarbonate, base substrate for evaluation in a turbulent boundary layer facility. In this chapter, a description of the SHSs, their fabrication methods, and the facility in which they were tested is presented. Images of the SHSs and a table of their roughness is provided. A description of the facility and measurement methods follows. An estimation of the experimental uncertainty and flow measurements over a hydryodynamically-smooth baseline surface concludes the chapter. This chapter closely resembles the archival works by *Gose et al.* (2017a, 2018).

5.1 Superhydrophobic Fabrication for the External Flow Experiments

The SHSs described here were previously shown to provide drag reduction in turbulent flow (*Gose et al.*, 2016b, 2017b). As such, variations of these surfaces were fabricated for application in an external turbulent boundary layer flow (*Gose et al.*, 2017a, 2018). Additional surface variations of the coatings were generated to evaluate the effective roughness for coatings with the same surface chemistry. A brief

discussion of the SHS fabrication, which is similar to the above, is provided here-in. In this effort, S_q is systematically varied from 1.7 ± 0.3 μm to 33 ± 4 μm for the samples tested, which will provide critical insight into the effect of superhydrophobic roughness when exposed to turbulent flow. S_q is tabulated for each SHS in Table 5.1.

Surface 1 (and variations of it, 1a through 1d) is fabricated by spray coating a blend of a fluorinated polyurethane polyol (Helicity Inc.) with a highly hydrophobic molecule, fluorodecyl polyhedral oligomeric silsesquioxane (F-POSS). A solution of the polyol and a urethane crosslinker, 4,4-Diisocyanato-methylenedicyclohexane (Wanhua Chemical Group Co.), is dissolved in Vertrel XF (Chamois). To this solution, the F-POSS is added such that the overall concentration is 200 mg per mL and 20 wt% is comprised of the F-POSS. The mixture is sonicated until it became completely transparent, approximately 30 seconds. Volumes of 10 ml (1c), 20 ml (1a,1b), and 40 ml (1d) of the solution are sprayed onto a 1.2 m x 0.2 m polycarbonate substrate using an ATD Tools 6903 high volume-low pressure spray gun with compressed air at a pressure of 140 kPa (20 psi). The sample is cured at 80 degrees C for 72 hours in an ambient environment using a silicone heating pad. An SEM image of Surface 1d is shown in *figure* 5.1.

Surface 2 is fabricated by forming a solution of fast-curing superglue (SF-100, 3M) and the same F-POSS molecules as above in equal mass fractions in Asahiklin-225 (Asahi Glass Co.) at a concentration of 50 mg per mL. The solution is sprayed using the same procedures as Surface 1. Surface 2 is cured at 50 degrees C for 60 minutes. An SEM image of Surface 2 is shown in *figure* 5.1.

Surface 3 consisted of a blend of the fluorinated polyurethane polyol and crosslinker from Surface 1 and fluoro-functionalized silica nanoparticles. The particles are nominally 50 to 100 nm irregular aggregates, the synthesis of which is described by *Campos et al.* (2011). A 25 mg per mL solution of these components is formed in Vertrel XF, with 35% of the total mass being the silica particles. A total of 20 mL of this solution
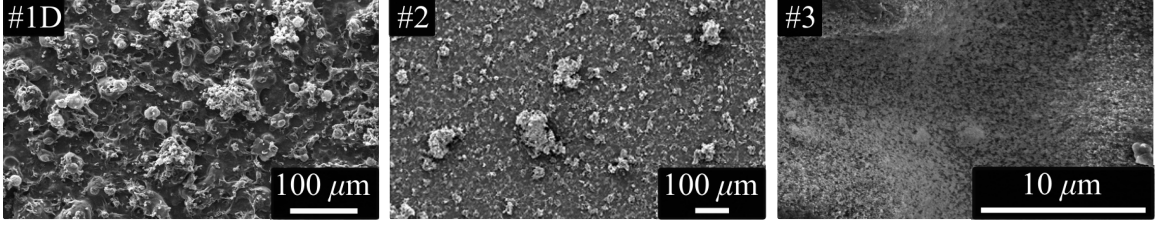
Figure 5.1: SEM micrographs of Surface 1D (left), 2 (center) and 3 (right), collected using a Phillips XL30 FEG.

Surface	1a	1b	1c	1d	2c	3a
S_q [μm]	22 ± 1	24 ± 2	16 ± 2	33 ± 4	1.9 ± 0.2	1.7 ± 0.4

Table 5.1: Summary of the two-dimensional root-mean-square roughness S_q, as defined in 2.5.

is sonicated until clear, and then sprayed and cured using the same procedures as for Surface 1. It is important to note that this surface derives its roughness from the silica nanoparticles, as opposed to the spraying process as with Surfaces 1 and 2, and in this way the roughness could be kept small compared to the other sprayed surfaces. An SEM image of Surface 3 is shown in *figure* 5.1.

5.2 External Turbulent Boundary Layer Facility

Experiments are conducted in a recirculating water tunnel designed for detailed boundary-layer measurements. The test facility is shown in *figure* 5.2. The test section is 2.0 m long, 0.2 m wide, and nominally 0.1 m high. The bottom wall is a flat plate which served as the test wall. The upper wall is adjustable and set for a nominally zero streamwise pressure gradient with a nominal free-stream velocity U_0 of 1.25 ms^{-1} for all cases. The acceleration parameter, defined as

$$K = \frac{\nu}{U_0^2} \frac{dU_0}{dx} \tag{5.1}$$

73
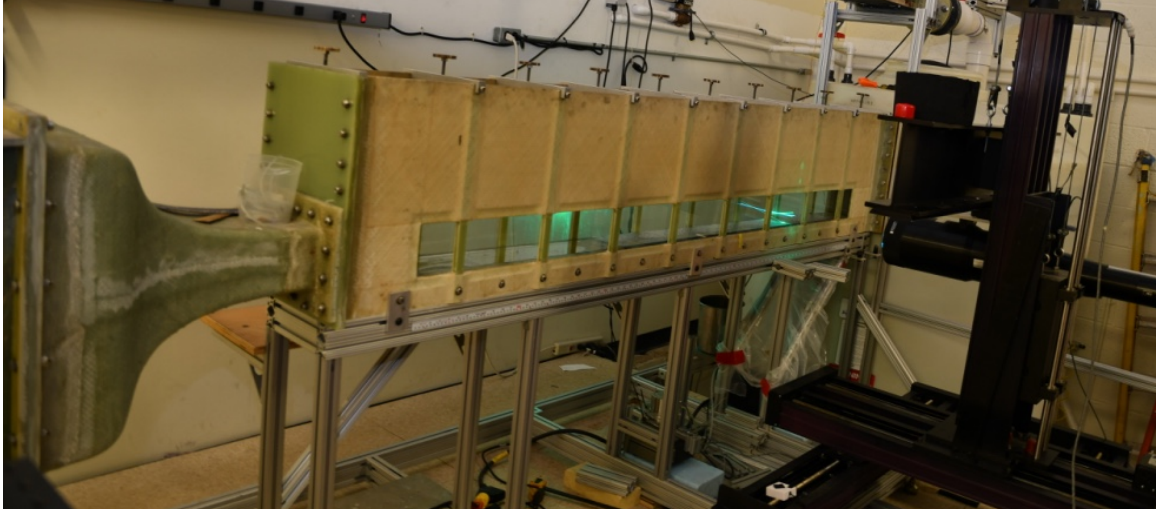
Figure 5.2: Image of the recirculating TBL facility that is used in this work. The facility is located at the U.S. Naval Academy and has been used in numerous TBL experiments by Drs. Michael Schultz and Karen Flack. The LDV system is shown on the right, while the SHS is seen at the lower wall of the facility.

is less than 5×10^{-9}. The upper wall and sidewalls provided optical access. The boundary-layer is tripped near the leading edge with a 0.8 mm diameter wire, fixing the location of transition and ensuring a TBL over the surfaces. Velocity measurements showed that a core flow remained at downstream end of the test section. Flow is supplied to the test section from a 4,000 L cylindrical tank. Water is drawn from the tank by two variable-speed, 7.5 kW pumps operating in parallel, and then sent to a flow-conditioning section consisting of a diffuser containing perforated plates, a honeycomb, three screens and a three-dimensional contraction. The test section immediately followed the contraction. The free-stream turbulence level is less than 0.5%. Water exited the test section through a perforated plate emptying into the cylindrical tank. The test fluid is filtered and deaerated water. A chiller is used to keep the water temperature constant to within one Kelvin during all tests.

Boundary-layer velocity measurements are obtained with a TSI FSA3500 two-component laser-Doppler velocimeter (LDV). The LDV consisted of a four-beam fiber

optic probe that collects data in backscatter mode. A custom-designed beam displacer is added to the probe to shift one of the four beams, resulting in three co-planar beams that can be aligned parallel to the wall. Additionally, a 2.6:1 beam expander is located at the exit of the probe to reduce the size of the measurement volume. The resulting probe volume diameter d is 45 μm with a probe volume length l of 340 μm. The corresponding measurement volume diameter and length in viscous length scales are $d^+ \leq 2.2$ and $l^+ \leq 16$.

Measurements are recorded approximately 1.5 m downstream of the trip, or 0.8 m downstream of the leading edge of the SHS plates resulting in a development length of approximately 45δ (boundary layer height). For the velocity profiles, the LDV probe is traversed to 45 locations within the boundary layer with a Velmex three-axis traverse unit. The traverse allowed the position of the probe to be maintained to ± 5 μm in all directions. For the first ten points near the wall, a total data sampling time is set to 300 seconds, yielding 10,000 to 20,000 random velocity samples for each velocity component. The large sampling time is necessary for the velocity statistics to converge, due to the lower data rate in the near-wall region. Subsequent points are limited to 180 seconds for sake of time; however, yielding 30,000 or more data points per wall-normal location. The experiments are conducted over the period of approximately four hours. The data are collected in coincidence mode. The flow is seeded with 2 μm diameter silver-coated glass spheres.

5.3 Velocity Measurements over a Hydrodynamically-Smooth Baseline

Velocity measurements and stresses over a hydrodynamically-smooth baseline are shown in *figures* 5.3 and 5.4, respectively. These results show that the measurements are in very good agreement with the expected results of a TBL, with $\kappa = 0.41$ and

$B = 5$ for the smooth-wall log-law values.
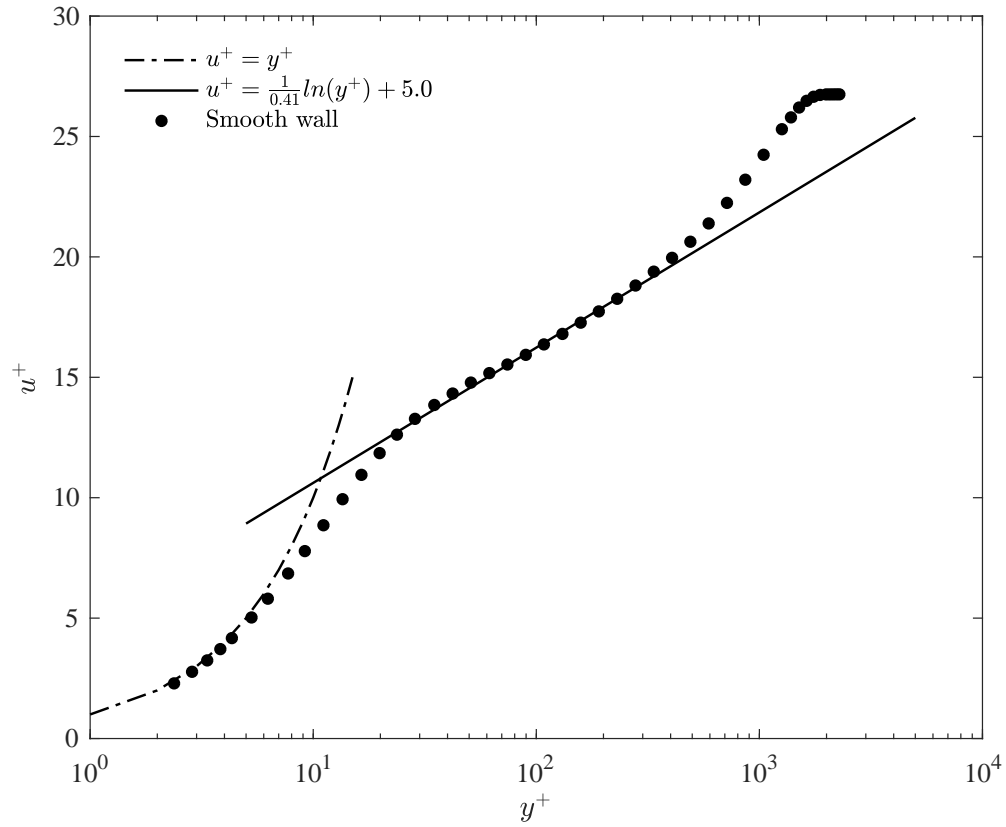
Figure 5.3: Mean velocity profiles for the hydrodynamically-smooth baseline at a nominal Re$_\tau$ of 1,600.

Figure 5.4: Profiles of the viscous shear stress, Reynolds stress, and total shear stress for the hydrodynamically-smooth baseline at a nominal Re_τ of 1,600.

CHAPTER VI

Results and Discussion II: External Turbulent Boundary Layer Flow

In this chapter, measurements of the mean velocity profile and stresses of a TBL Flow over several spray applied SHSs are presented. The results are determined from two analysis methods: the total stress method, similar to *Ling et al.* (2016), and a new method which used a log+wake fit to the velocity profile. The analysis methods directly affect the outcomes of the local shear stress, and in turn, the resulting drag reduction as defined in (6.1), where C_f is the coefficient of skin-friction.

$$DR = \frac{C_{f,Smooth} - C_{f,SHS}}{C_{f,Smooth}} \tag{6.1}$$

Note that the aforementioned equation for drag reduction is slightly different than that which was presented previously. A summary of the flow parameters for each analysis method are presented and compared directly to the results for the hydrodynamically-smooth baseline.

6.1 Total Stress Method

A method based on the total shear-stress, similar to *Ling et al.* (2016) is implemented, and its performance tested. Table 6.1 summarizes the flow parameters

Surface	U_0 [ms^{-1}]	δ [mm]	u_τ [ms^{-1}]	Re$_\tau$ [-]	C_f [10^{-3}]	DR [%]
Smooth-wall	1.24	33.5	0.046	1626	2.80	-
1a	1.27	34.3	0.040	1442	2.00	+28
1b	1.26	33.5	0.041	1446	2.15	+23
1c	1.29	30.9	0.046	1491	2.56	+8.3
1d	1.29	27.9	0.045	1328	2.47	+12
2c	1.26	35.8	0.041	1542	2.13	+24
3a	1.28	34.1	0.038	1363	1.79	+36

Table 6.1: Summary of the flow parameters from the total stress method, adopted and modified from *Ling et al.* (2016).

as determined from the total stress method with DR ranging from $+8$ to $+36\%$ for the six SHSs discussed. Mean velocity profiles are presented in *figure* 6.1, while the stresses, non-dimensionalized by the smooth wall friction velocity u_τ are shown in *figure* 6.2. The total stress method uses an average of the first five points in the total stress to determine the wall shear stress and friction velocity. It is believed this is a conservative estimate based on the shape of the stresses in *figure* 6.2, which do not asymptote to one.

The mean velocity profiles for the SHSs had an increased velocity from wall through the wake region of the TBL. The increase in the mean velocity profiles is likely due to the presence of the air-water interface, and indicated that the roughness of the SHSs is not negatively affecting the flow and that an overall drag reduction is expected, particularly considering the viscous length scale is a fraction of the roughness of the SHSs evaluated. Moreover, the data indicate a decrease in the near-wall viscous stress of 25 to 50% for each SHS with an increase of near-zero to 25% in the near-wall Reynolds stresses. The increases in Reynolds stress generally appear to coincide with increases in roughness. Lastly, from the stresses it is very apparent that increases in both streamwise and spanwise velocity fluctuations (u' and v') over the smooth wall, resulting in significantly higher Reynolds stress and total stress in the overlap region of the TBL.

Figure 6.1: Mean velocity profiles for the hydrodynamically-smooth baseline and the SHSs - as determined from the total stress method - at nominal Re_τ of 1,600.
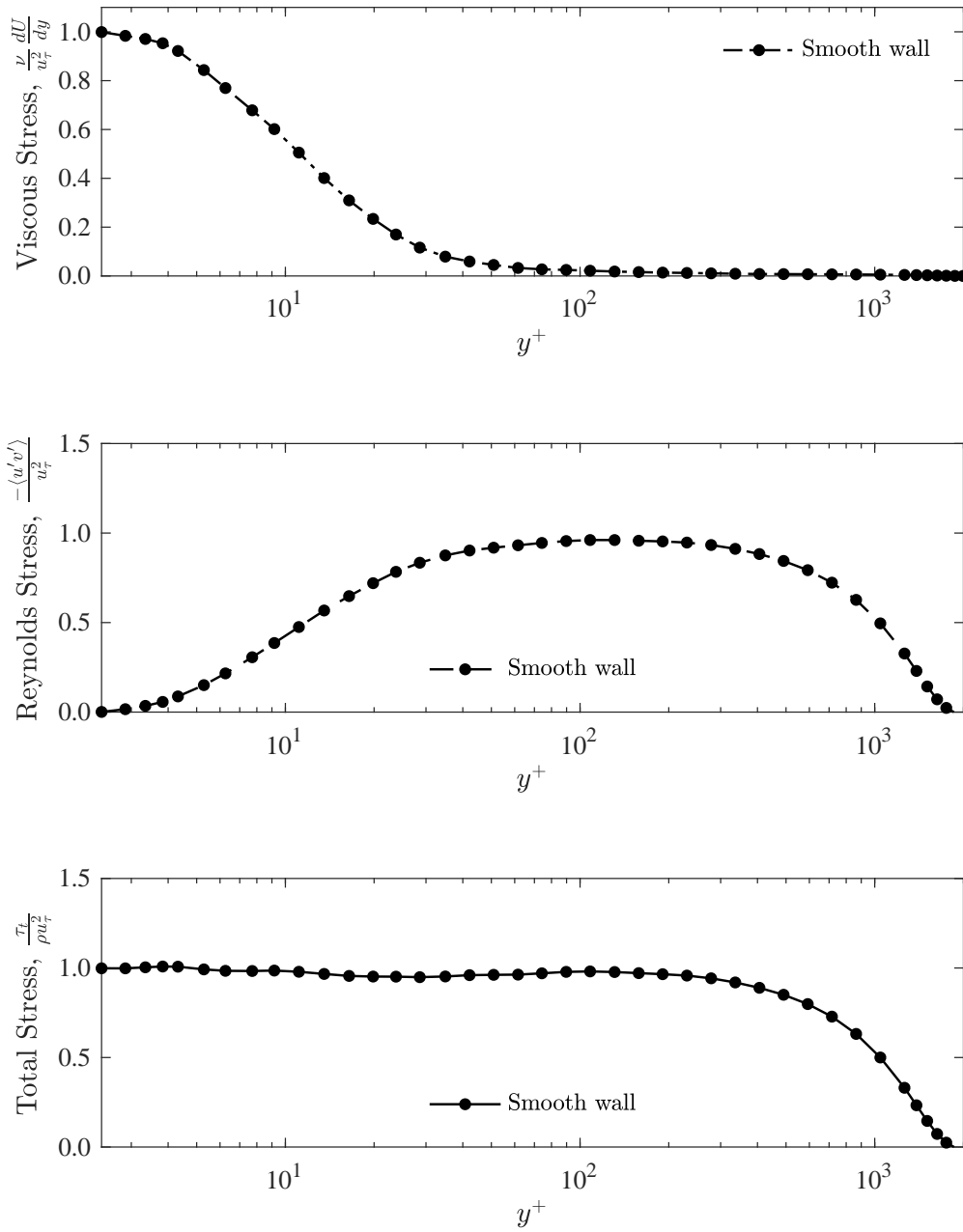
Figure 6.2: Profiles of the viscous shear stress, Reynolds stress, and total shear stress for the hydrodynamically-smooth baseline and the SHSs - as determined from the total stress method - at nominal Re_τ of 1,600.

Although not presented here, the total stress method is proven to produce a range of C_f estimations on multiple runs from the same SHS surface. One possible explanation is that small changes in pressure drag could occur due to the local plastron topography where the LDV measurements were taking place. This may have introduced concomitant changes in both viscous and Reynolds shear stress in the sublayer region, and thus affect the C_f estimation from the total stress profile. Moreover, it is known that heterogeneous, randomly rough SHSs are governed by an effective slip length and slip velocity, which can not be determined using a point measurement, such as that provided by the LDV. Thus, the measurements presented, are likely dependent on the LDV measurement location selected.

6.2 Log+Wake Method

Because the LDV measurements are recorded several boundary layer thicknesses downstream of the leading edge of the SHSs, the flow could adjust to a new, drag reducing self-similar state. Therefore, the log-layer should reflect, in a mean sense, the structural changes due to the new wall boundary condition. Therefore, to determine the wall shear stress, and thus the friction velocity and C_f, a nonlinear least square minimization based on the logic of a log-law plus wake deviation for rough-wall flows was implemented, in the form

$$u^+ = \frac{1}{\kappa}\ln(y^+) + B + \frac{2\Pi}{\kappa}\sin^2\left(\frac{y}{\delta}\frac{\pi}{2}\right) - \Delta U^+ \tag{6.2}$$

where $\kappa = 0.41$ and $B = 5$ are the smooth wall log-law values, and u_τ, ΔU, and Π are the parameters determined from the nonlinear minimization. For the SHSs, a negative ΔU^+ means that the shift in the log-law is above the smooth-wall log-law resulting in drag reduction.

Table 6.2 summarizes the flow parameters for the log+wake method. Mean ve-

Surface	U_0 [ms^{-1}]	δ [mm]	u_τ [ms^{-1}]	Re$_\tau$ [-]	C_f [10^{-3}]	DR [%]
Smooth-wall	1.24	33.5	0.046	1620	2.77	-
1a	1.27	34.3	0.050	1789	3.09	-11
1b	1.26	33.5	0.043	1510	2.34	+16
1c	1.29	30.9	0.043	1386	2.22	+20
1d	1.29	27.9	0.049	1424	2.84	-2.3
2c	1.26	35.8	0.042	1564	2.20	+21
3a	1.28	34.1	0.047	1693	2.76	+0.5

Table 6.2: Summary of the flow parameters from the log+wake method defined in Eq. 6.2.

locity profiles are presented in *figure* 6.3, while the stresses, non-dimensionalized the smooth wall friction velocity u_τ are shown in *figure* 6.4. Although the non-dimensionalized stresses look very similar to the results from the total stress method, the mean velocity profiles of the SHSs have greater variation when compared to the smooth wall. Most notably, the SHSs have velocity profiles that lie both above and below the smooth-wall data, yet all of the SHSs result in local DR ranging from -11 to +21%. This result is a bit surprising as a reduction in u^+ is consistent with the presence of a rough surface in a TBL. Nevertheless, unlike the total stress method, consistent estimation of the friction velocity is seen from multiple runs for a given tested SHS when analyzed using the log+wake method.

6.3 Concluding Remarks

In this brief review, the need to further investigate SHS, for turbulent drag reduction in large-scale applications is highlighted. The surfaces were designed to be a scalable spray formulation with strong mechanical durability and resistance to wetting. The results previously collected for fully-developed turbulent channel flow and those shown here for an external TBL flow at comparable friction Reynolds number are in good agreement. The results show that heterogeneous, randomly rough, SHS spray applied over large areas can provide meaningful total drag reduction; however,
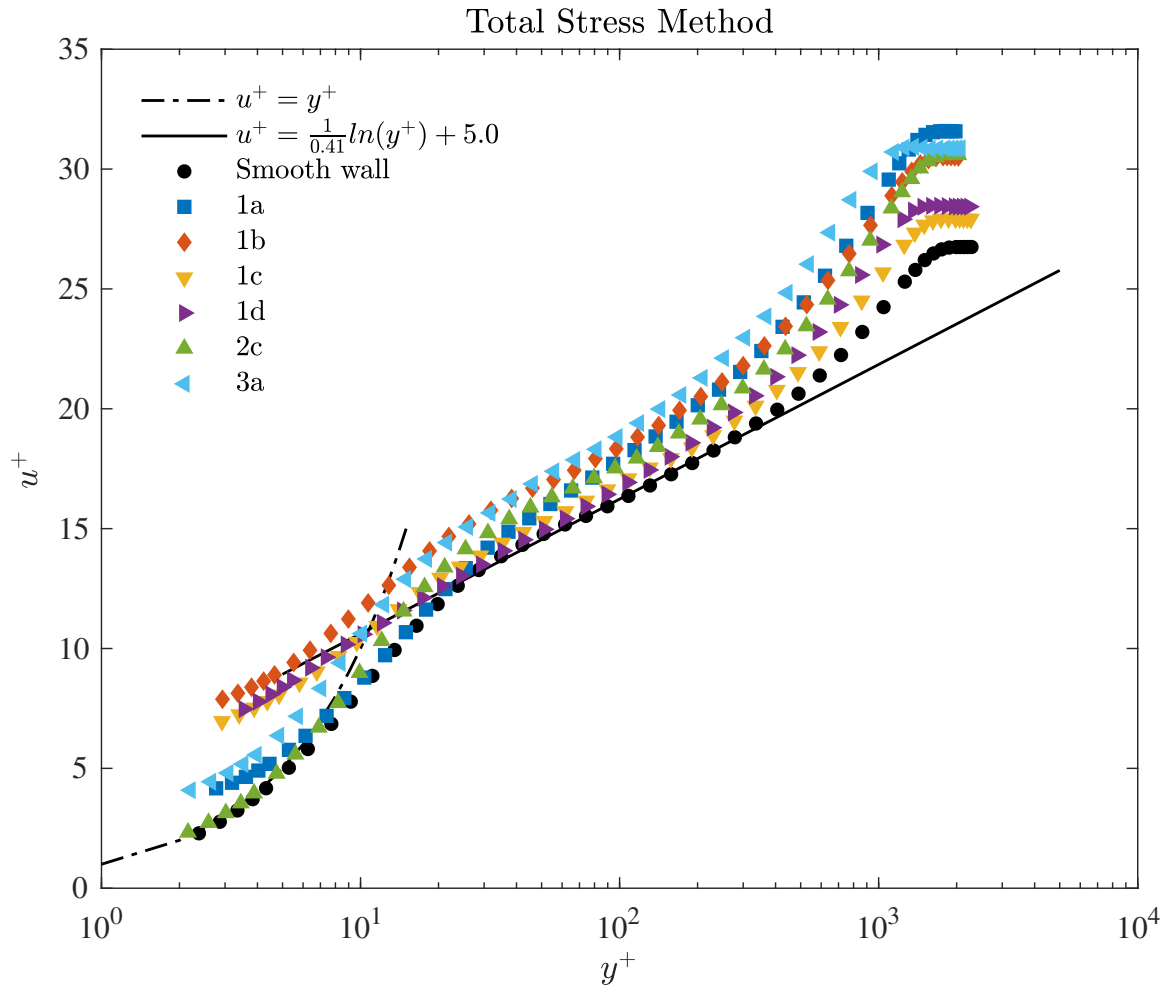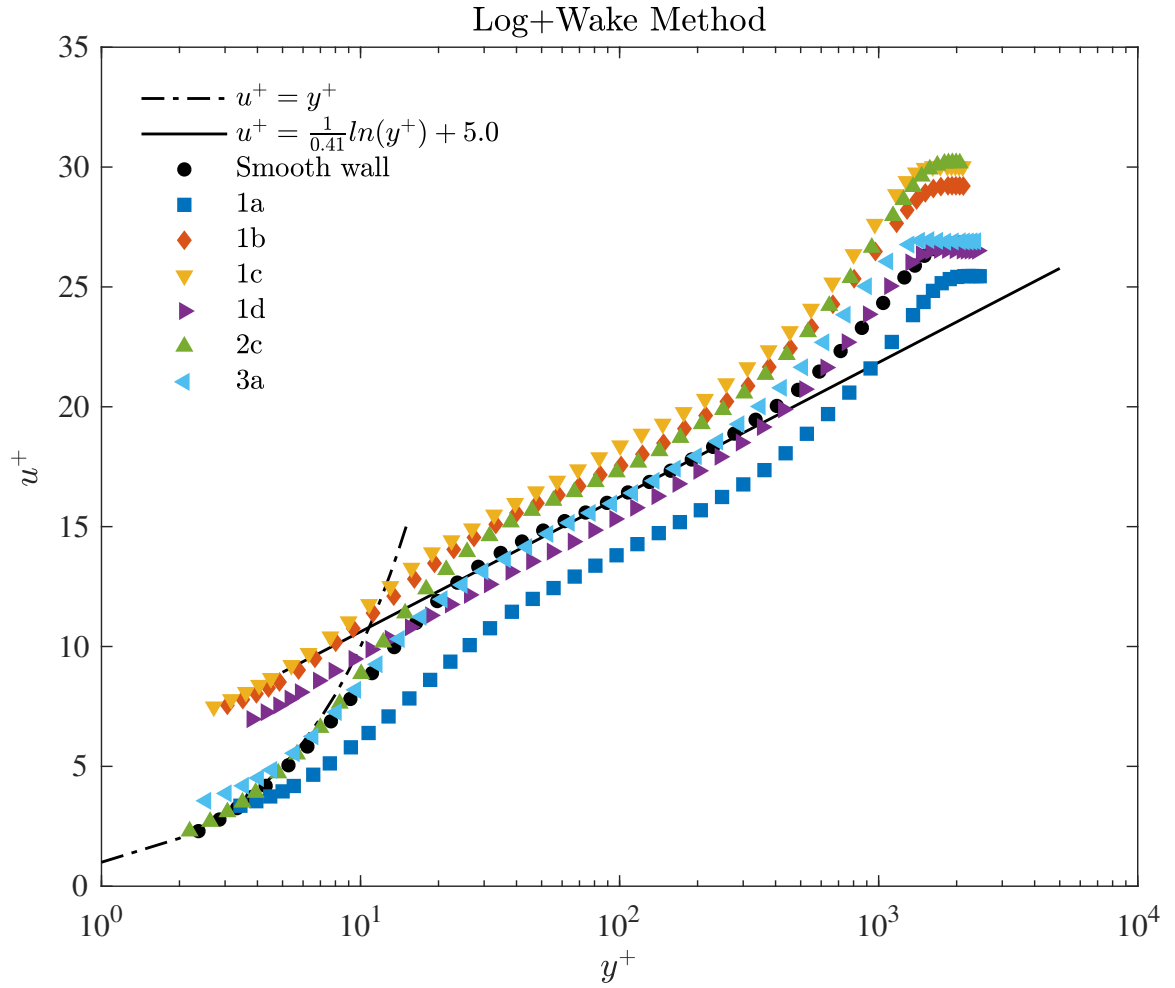
Figure 6.3: Mean velocity profiles for the hydrodynamically-smooth baseline and the SHSs - as determined from the log+wake method - at nominal Re_τ of 1,600.
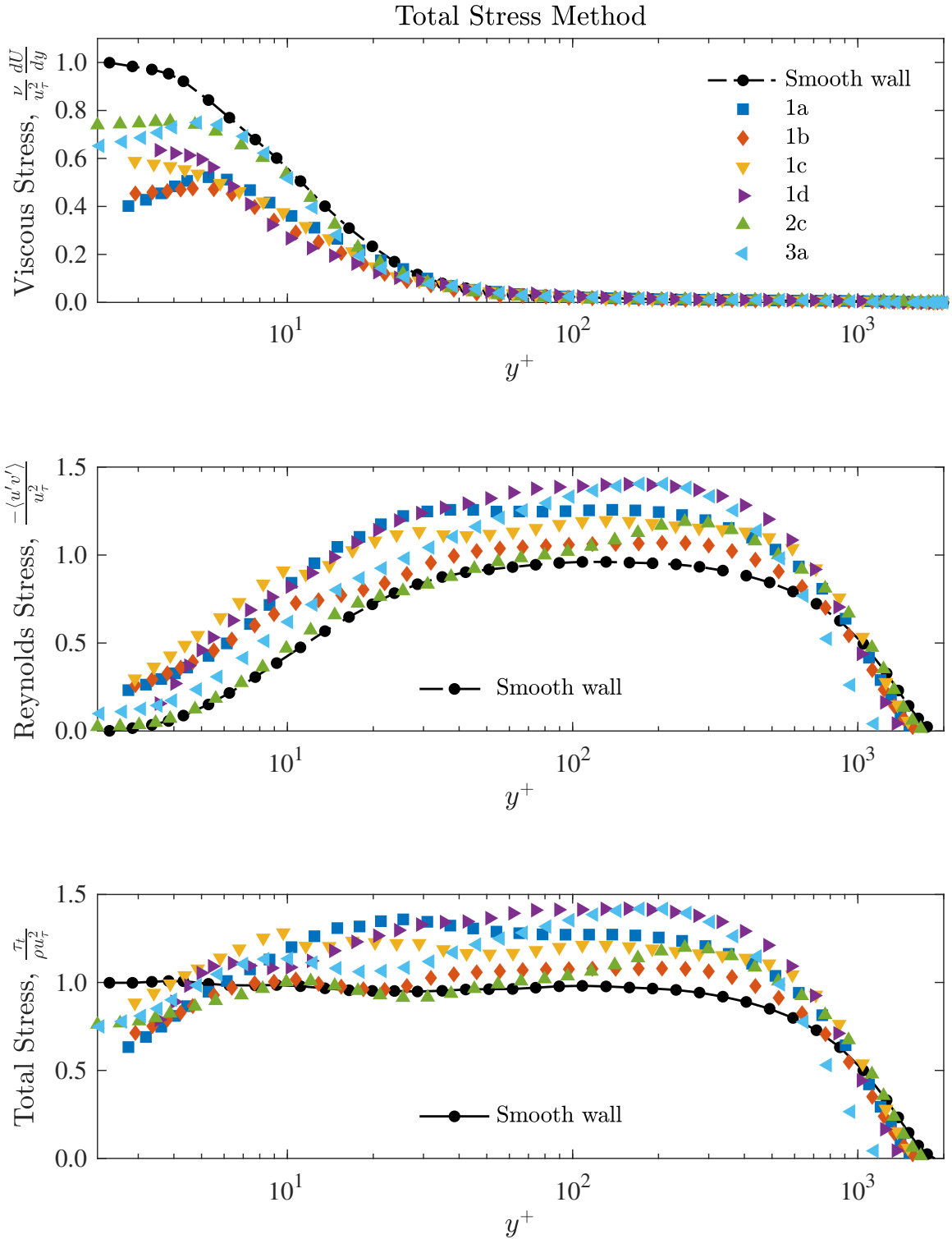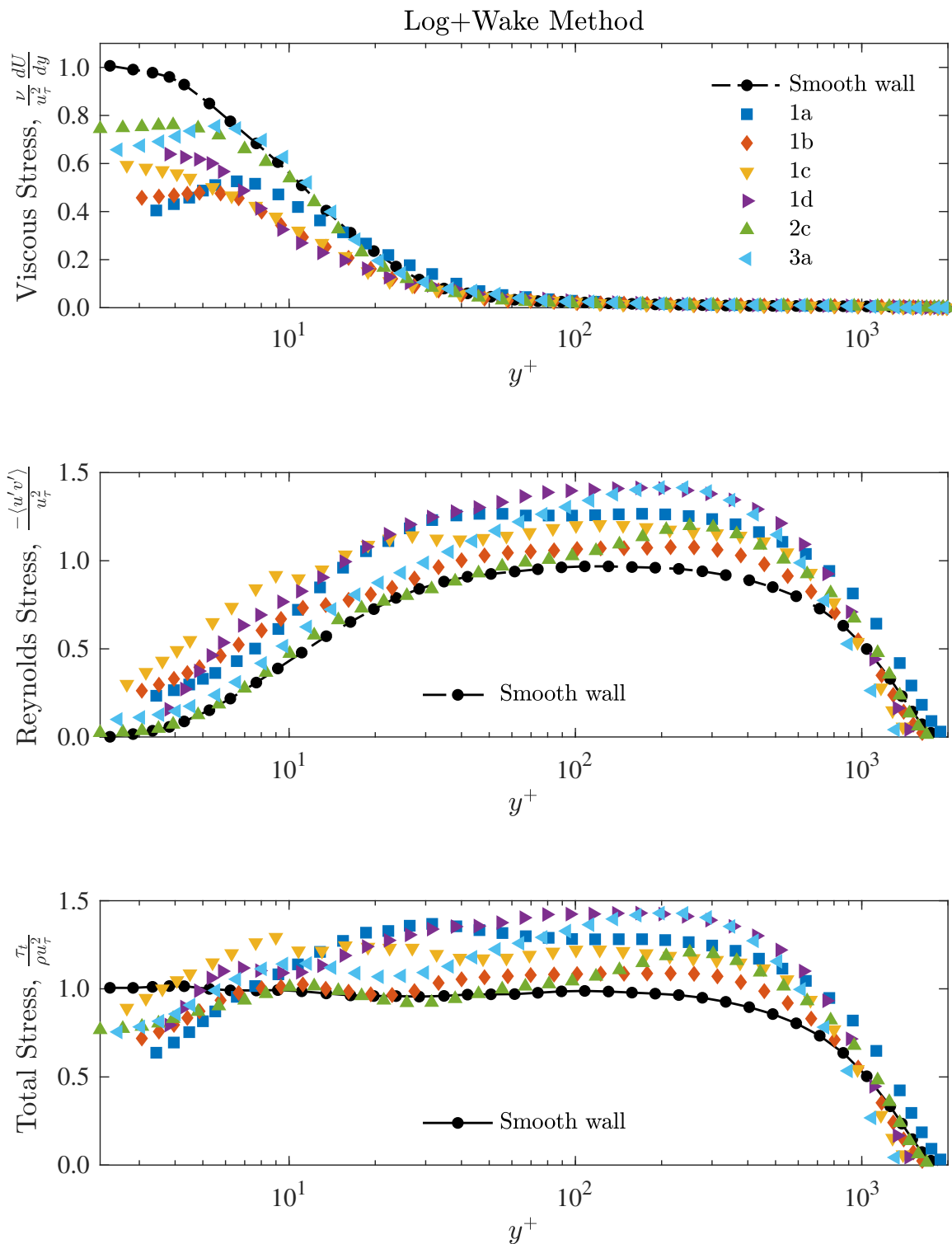
Figure 6.4: Profiles of the viscous shear stress, Reynolds stress, and total shear stress for the hydrodynamically-smooth baseline and the SHSs - as determined from the total stress method - at nominal Re_τ of 1,600.

the analysis methods and inconsistencies need additional attention. The aforementioned discussion emphasizes the importance of analysis methods used to characterize the flow field and skin-friction in turbulent flow. As shown here, two methods used to characterize frictional benefits of SHS can provide very different results. Nevertheless, it is believed the spray SHSs discussed here were appropriated designed and applied to provided meaningful ($> 10\%$) DR in naval relevant, TBL flows.

Major findings from the external flow experiments are summarized here:

- Heterogeneously, randomly rough, spray applied SHSs have been shown to provide greater than 10% in turbulent boundary layer flow

- Increase in the mean velocity profile indicates that the roughness of the SHSs is not negatively affecting the flow and that an overall drag reduction is expected, particularly considering the viscous length scale was a fraction of the roughness of the SHSs evaluated

- The total stress method was observed to produce widely different C_f estimations on multiple runs from the same SHS surface

- Implementation of fit minimization to the velocity profile, the log+wake method, proved to provide similar results to those seen for the more widely accepted total stress method

- The data fit of the log+wake method establishes a κ and that results in a u_τ different from the that of the total stress method, essentially forcing the data to match a log+wake form that may not be a perfect match

- Using two analysis methods, the velocity measured showed a reduction in the wall-shear stress in a turbulent boundary layer flow over a spray applied SHS can be drastically from a smooth baseline

CHAPTER VII

Conclusions and Future Work

In this dissertation, the design and fabrication of scalable SHSs that are capable of providing meaningful drag reduction in navy relevant turbulent flows have been addressed. These surfaces were fabricated to exhibit large apparent contact angles, small contact angle hysteresis, and small non-dimensional roughness, which in turn resulted in surfaces that affected the near-wall region of turbulent flow over the SHSs and resulted in a reduction of skin friction compared to a hydrodynamically-smooth flat surface. Pressure drop measurements in an internal, fully-developed turbulent channel flow demonstrated that a decrease in the frictional loss of greater than 50% could be achieved over a range of friction based Reynolds numbers.

Similar surfaces were then applied to the flow over an external TBL at a higher friction Reynolds number. Measurements of the near-wall velocities over the SHSs showed a net increase in the mean velocity and a 20-50% decrease in the wall viscous stresses. Moreover, meaningful drag reduction of greater than 10% was achievable.

Combined, these two studies showed that SHSs can be effective at reducing skin friction for turbulent wall bounded flows. The relevant wettability and roughness that dictate skin-friction of SHSs in TBLs, were determined to be the wetted area of the SHSs and the size of the largest surfaces features, relative to the size of the viscous sublayer, at the mean pressures experienced in the flow.

The followings sections elaborate on the major conclusions and future work of this study.

7.1 Development and Implementation of Spray Superhydrophobic Surfaces

At the start of this effort, SHS fabrication was generally limited to small scales, which were fabricated with patterned features. That is to say, SHSs were often created using lithography, laser etching, chemical or thermal deposition, or corrosion, and few SHSs were fabricated at length scales greater than a few centimeters. Hence, the size of SHSs that could be created, limited the feasibility of their application for flows with larger surface areas. For the flows of interest in the present study, it was necessary to develop a SHS that could be applied to areas on the order of one square meter. Therefore, a sprayable SHS was developed. This effort has demonstrated that heterogeneously, randomly rough SHSs can be created using a composite spray process, that would have virtually no area limitation. Effective spray deposition for the fabrication of SHSs was proven viable using both manual and automated methods. The surface was also shown to be durable for the laboratory flow conditions used in this study. Improvements to the creation of sprayed-on SHSs include the following.

First, the repeatability with which the SHS may be sprayed should be improved. Despite showing repeatability of several of the surfaces presented here, there were times throughout this effort that fabricated surfaces that possessed the desired superhydrophobic characteristics were unable to be generated. At times, a repeated SHS fabrication processes would render SHSs with different contact angles, roughness, and resistance to wetting, and hence were extremely difficult to characterize in any experimental application. This suggests that there may be an unrecognized or uncontrolled process during the manufacturing steps that should be identified and

controlled. Additionally, it has been shown here that unwanted asperity roughness is a major contributor to the inability of a SHSs to provide a reduced friction in turbulent flow. Processes need to be developed to reduce or eliminate the formation of asperities during manufacturing.

Moreover, mechanical robustness of spray SHSs will need to be improved. Many of the SHSs were susceptible to failure when contacted with anything other than water. Some deposited spray was easily removed, and thus needed to be handled delicately and occasionally needed secondary treatment following transport.

As the Reynolds number increases, the relative length scale decreases, and thus, the SHSs presented here will not be effective at Reynolds numbers much larger than those shown in the present study. Ideally, the manufacturing process would be such that they can control the length scales of the surface features, tuning them to be optimal for the design range of Reynolds numbers sought. Therefore, control of the surface topology of spray SHSs will need to be more predictable and precise to extend their application to higher Reynolds number flows.

7.2 Characterization of Meaningful SHS Drag Reduction in Turbulent Flows

We have shown that spray SHSs can produce meaningful drag reduction as discussed above. The range of friction based Reynolds numbers for which a given surface would be effective was determined after the surface was manufactured. The amount of drag reduction achieved was related directly to the surface features and the local skin friction (friction based Reynolds number). Indeed, the difference in total friction drag reduction achieved between the University of Michigan and U.S. Naval Academy facilities can be related to the difference in the friction based Reynolds number of the two flows and to the fact that Re_τ is constant in the fully-developed turbulent flow

and evolves downstream for the TBL. Additional, different ambient pressures are realized for the two flows.

However, the efficacy of the friction reduction for both surfaces would degrade over several hours. This was likely due to the removal of the air trapped in the surface by the turbulent flow and by direct gas diffusion. Both passive and active gas replenishment were somewhat explored as part of this effort. Methods of active gas replenishment should continue to be a topic of further investigation.

Also, these studies have been conducted on flat surfaces, while many objects of naval interest include curved surfaces with pressure gradients. Experiments are currently underway to determine the overall drag reduction that can be achieved on a towed DARPA SUBOFF model, and these results will help answer the questions raised above.

7.3   Scaling the Effects of SHS Roughness and Wettability for Drag Reduction

It has been shown that the physical topology and the wettability of the SHS both play key roles in effectiveness as a agent for skin friction reduction. To first order, the surface roughness length scale k^+ adequately captured the most important scale of the topology. The wetted area as a function of mean static pressure, denoted as ϕ_s, to first order, captured the most important element of the surface wettability. Together, these two parameters were shown to properly predict the performance of a given SHS at a given friction based Reynolds number. In all cases, this scaling was effective for surfaces that did not have significant numbers of roughness asperities extending beyond the viscous sublayer of the flow.

This successful scaling could be improved by considering higher order parameters of both the SHS and the TBL flow. The effects of other surface length scales, chemical

properties, and additional TBL characteristics should be examined.

If SHSs could be manufactured with a controlled range of properties, they could then be tested over a wider range of Reynolds numbers. This would help further the understanding of the flow physics of SHS drag reduction, and help yield improved models that relate the SHS properties to the resulting FDR.

BIBLIOGRAPHY

BIBLIOGRAPHY

Aljallis, E., M. Sarshar, R. Datla, S. Hunter, J. Simpson, V. Sikka, A. Jones, and C.-H. Choi (2011), Measurement of Hydrodynamic Frictional Drag on Superhydrophobic Flat Plates in High Reynolds Number Flows, *Proceedings of the ASME 2011 International Mechanical Engineering Congress & Exposition*, pp. 1–6, doi: 10.1115/IMECE2011-63272.

Aljallis, E., V. K. Sikka, A. K. Jones, M. A. Sarshar, R. Datla, C. H. Choi, V. K. Sikka, A. K. Jones, and C. H. Choi (2013), Experimental study of skin friction drag reduction on superhydrophobic flat plates in high Reynolds number boundary layer flow, *Physics of Fluids*, *25*(2), 025,103, doi:10.1063/1.4791602.

Argyros, D., C. Raucci, T. Smith, and N. Sabio (2014), Global Marine Fuel Trends 2030, *Report*, UCL Energy Institute and Lloyd's Register Group Limited, London, England.

Balasubramanian, A. K., A. C. Miller, and O. K. Rediniotis (2004), for Hydrodynamic Drag Reduction, *Notes*, *42*(2), 6–9, doi:10.2514/1.9104.

Barlow, J., W. Rae, and A. Pope (1999), *Low-Speed Wind Tunnel Testing*, 3rd ed., 713 pp., Wiley, New York.

Barthlott, W., and C. Neinhuis (1997), Purity of the sacred lotus, or escape from contamination in biological surfaces, *Planta*, *202*(1), 1–8, doi:10.1007/s004250050096.

Bartolo, D., F. Bouamrirene, É. Verneuil, A. Buguin, P. Silberzan, and S. Moulinet (2006), Bouncing or sticky droplets: Impalement transitions on superhydrophobic micropatterned surfaces, *Europhysics Letters*, *74*(2), 299–305, doi: 10.1209/epl/i2005-10522-3.

Bhushan, B., and Y. C. Jung (2011), Natural and biomimetic artificial surfaces for superhydrophobicity, self-cleaning, low adhesion, and drag reduction, *Progress in Materials Science*, *56*(1), 1–108, doi:10.1016/j.pmatsci.2010.04.003.

Bhushan, B., Y. C. Jung, and K. Koch (2009), Micro-, nano- and hierarchical structures for superhydrophobicity, self-cleaning and low adhesion, *Philosophical Transactions of the Royal Society A: Mathematical, Physical and Engineering Sciences*, *367*(1894), 1631–1672, doi:10.1098/rsta.2009.0014.

Bidkar, R. A., L. Leblanc, A. J. Kulkarni, V. Bahadur, S. L. Ceccio, and M. Perlin (2014), Skin-friction drag reduction in the turbulent regime using random-textured hydrophobic surfaces, *Physics of Fluids*, *26*(8), 85,108, doi:10.1063/1.4892902.

Bixler, G. D., and B. Bhushan (2013a), Fluid drag reduction with shark-skin riblet inspired microstructured surfaces, *Advanced Functional Materials*, *23*(36), 4507–4528, doi:10.1002/adfm.201203683.

Bixler, G. D., and B. Bhushan (2013b), Bioinspired micro/nanostructured surfaces for oil drag reduction in closed channel flow, *Soft Matter*, *9*(5), 1620–1635, doi:10.1039/C2SM27070F.

Bixler, G. D., and B. Bhushan (2013c), Shark skin inspired low-drag microstructured surfaces in closed channel flow, *Journal of Colloid and Interface Science*, *393*(1), 384–396, doi:10.1016/j.jcis.2012.10.061.

Bormashenko, E. E., Y. Bormashenko, T. Stein, G. Whyman, and E. E. Bormashenko (2007), Why do pigeon feathers repel water? Hydrophobicity of pennae, Cassie-Baxter wetting hypothesis and Cassie-Wenzel capillarity-induced wetting transition, *Journal of Colloid and Interface Science*, *311*(1), 212–216, doi:10.1016/j.jcis.2007.02.049.

Bureau of Transportation Statistics (2012), Table 4-5: Fuel Consumption by Mode of Transportation in Physical Units, *Tech. rep.*, U.S. Department of Transportation.

Bushnell, D. (1991), Drag Reduction In Nature, *Annual Review of Fluid Mechanics*, *23*(1), 65–79, doi:10.1146/annurev.fluid.23.1.65.

Busse, A., N. D. Sandham, G. McHale, and M. I. Newton (2013), Change in drag, apparent slip and optimum air layer thickness for laminar flow over an idealised superhydrophobic surface, *Journal of Fluid Mechanics*, *727*, 488–508, doi:10.1017/jfm.2013.284.

Campos, R., A. J. Guenthner, T. S. Haddad, and J. M. Mabry (2011), Fluoroalkyl-functionalized silica particles: Synthesis, characterization, and wetting characteristics, *Langmuir*, *27*(16), 10,206–10,215, doi:10.1021/la201545a.

Cassie, A. B. D., and S. Baxter (1944), Wettability of porous surfaces, *Transactions of the Faraday Society*, *40*(26), 546, doi:10.1039/tf9444000546.

Ceccio, S. L. (2010), Friction Drag Reduction of External Flows with Bubble and Gas Injection, *Annual Review of Fluid Mechanics*, *42*(1), 183–203, doi:10.1146/annurev-fluid-121108-145504.

Choi, C. H., and C. J. Kim (2006), Large slip of aqueous liquid flow over a nanoengineered superhydrophobic surface, *Physical Review Letters*, *96*(6), doi:10.1103/PhysRevLett.96.066001.

Daniello, R. J., N. E. Waterhouse, and J. P. Rothstein (2009), Drag reduction in turbulent flows over superhydrophobic surfaces, *Physics of Fluids*, *21*(8), doi: 10.1063/1.3207885.

Davenport, J., R. Hughes, and M. Shorten (2011), Drag reduction by air release promotes fast ascent in jumping emperor penguins—a novel hypothesis, *Marine Ecology Progress Series*, *430*, 171–182.

Dean, R. B. (1978), Reynolds Number Dependence of Skin Friction and Other Bulk Flow Variables in Two-Dimensional Rectangular Duct Flow, *Journal of Fluids Engineering*, *100*(2), 215–223, doi:10.1115/1.3448633.

Durst, F., M. Fischer, J. Jovanovic, and H. Kikura (1998), Methods to Set Up and Investigate Low Reynolds Number, Fully Developed Turbulent Plane Channel Flows, *Journal of Fluids Engineering*, *120*(3), 496–503, doi:Doi 10.1115/1.2820690.

Feng, B. L., et al. (2002), Super-hydrophobic surfaces: From natural to artificial, *Advanced Materials*, *14*(24), 1857–1860, doi:DOI 10.1002/adma.200290020.

Flack, K. A., and M. P. Schultz (2010), Review of Hydraulic Roughness Scales in the Fully Rough Regime, *Journal of Fluids Engineering*, *132*(4), 041,203, doi: 10.1115/1.4001492.

Gao, X., and L. Jiang (2004), Water-repellent legs of water striders, *Nature*, *432*(7013), 36, doi:10.1038/432036a.

Garcia-Mayoral, R., and J. Jimenez (2011), Drag reduction by riblets, *Philosophical Transactions of the Royal Society A: Mathematical, Physical and Engineering Sciences*, *369*(1940), 1412–1427, doi:10.1098/rsta.2010.0359.

Gogte, S., P. Vorobieff, R. Truesdell, A. Mammoli, F. van Swol, P. Shah, and C. J. Brinker (2005), Effective slip on textured superhydrophobic surfaces, *Physics of Fluids*, *17*(5), 1–4, doi:10.1063/1.1896405.

Golovin, K., D. H. Lee, J. M. Mabry, and A. Tuteja (2013), Transparent, flexible, superomniphobic surfaces with ultra-low contact angle hysteresis, *Angewandte Chemie - International Edition*, *52*(49), 13,007–13,011, doi: 10.1002/anie.201307222.

Golovin, K., M. Boban, J. M. Mabry, and A. Tuteja (2017), Designing Self-Healing Superhydrophobic Surfaces with Exceptional Mechanical Durability, *ACS Applied Materials and Interfaces*, *9*(12), 11,212–11,223, doi:10.1021/acsami.6b15491.

Golovin, K. B., J. W. Gose, M. Perlin, S. L. Ceccio, and A. Tuteja (2016), Bioinspired surfaces for turbulent drag reduction, *Philosophical Transactions of the Royal Society A: Mathematical, Physical and Engineering Sciences*, *374*(2073), 20160,189, doi:10.1098/rsta.2016.0189.

Gose, J. W., K. Golovin, J. Barros, M. P. Schultz, A. Tuteja, S. L. Ceccio, and M. Perlin (2016a), Biomimetic Super-Hydrophobic Coatings for Friction Reduction, in *The 10th Conference on High-Performance Marine Vehicles (HIPER)*, pp. 477–490, Cortona, Italy.

Gose, J. W., K. Golovin, A. Tuteja, S. L. Ceccio, and M. Perlin (2016b), Experimental Investigation of Turbulent Skin-Friction Drag Reduction Using Superhydrophobic Surfaces, in *31st Symposium on Naval Hydrodynamics*, September, pp. 11–16, Monterey, CA.

Gose, J. W., K. B. Golovin, J. M. Barros, M. P. Schultz, A. Tuteja, M. Perlin, and S. L. Ceccio (2017a), Laser Doppler Velocimetry Measurements of a Turbulent Boundary Layer Flow over Sprayed Superhydrophobic Surfaces, in *10th International Symposium on Turbulence and Shear Flow Phenomena (TSFP10)*, vol. 1, Chicago, USA.

Gose, J. W., K. B. Golovin, M. Boban, J. M. Mabry, A. Tuteja, M. Perlin, and S. L. Ceccio (2017b), Characterization of Superhydrophobic Surfaces for Drag Reduction in Turbulent Flow, *Journal of Fluid Mechanics, Submitted*, 1–18.

Gose, J. W., K. B. Golovin, M. Boban, J. Barros, M. P. Schultz, A. Tuteja, M. Perlin, and S. L. Ceccio (2018), Laser Doppler Velocimetry Measurements of a Turbulent Boundary Layer Flow over Sprayed Superhydrophobic Surfaces, *International Journal of Heat and Fluid Flow, Submitted*.

Gruncell, B. R. K., N. D. Sandham, and G. McHale (2013), Simulations of laminar flow past a superhydrophobic sphere with drag reduction and separation delay, *Physics of Fluids*, *25*(4), doi:10.1063/1.4801450.

Henoch, C., T. Krupenkin, P. Kolodner, J. Taylor, M. Hodes, A. Lyons, C. Peguero, and K. Breuer (2006), Turbulent drag reduction using superhydrophobic surfaces, in *Collection of Technical Papers - 3rd AIAA Flow Control Conference*, vol. 2, pp. 840–844, San Francisco, CA, USA, doi:10.2514/6.2006-3192.

Jelly, T. O., S. Y. Jung, and T. A. Zaki (2014), Turbulence and skin friction modification in channel flow with streamwise-aligned superhydrophobic surface texture, *Physics of Fluids*, *26*(9), doi:10.1063/1.4894064.

Jing, D., and B. Bhushan (2013), Boundary slip of superoleophilic, oleophobic, and superoleophobic surfaces immersed in deionized water, hexadecane, and ethylene glycol, *Langmuir*, *29*(47), 14,691–14,700, doi:10.1021/la4030876.

Joseph, P., and P. Tabeling (2005), Direct measurement of the apparent slip length, *Physical Review E - Statistical, Nonlinear, and Soft Matter Physics*, *71*(3), doi:10.1103/PhysRevE.71.035303.

Joseph, P., C. Cottin-Bizonne, J. M. Benoît, C. Ybert, C. Journet, P. Tabeling, and L. Bocquet (2006), Slippage of water past superhydrophobic carbon nanotube forests in microchannels, *Physical Review Letters*, *97*(15), 156,104, doi:10.1103/PhysRevLett.97.156104.

Jung, Y. C., and B. Bhushan (2010), Biomimetic structures for fluid drag reduction in laminar and turbulent flows, *Journal of Physics Condensed Matter*, *22*(3), 035,104, doi:10.1088/0953-8984/22/3/035104.

Kanda, M., R. Moriwaki, and F. Kasamatsu (2004), Large-eddy simulation of turbulent organized structures within and above explicity resolved cube arrays, *Boundary-Layer Meteorology*, *112*(2), 343–368, doi:10.1023/B:BOUN.0000027909.40439.7c.

Kim, J., and C.-J. Kim (2002), Nanostructured surfaces for dramatic reduction of flow resistance in droplet-based microfluidics, in *Proc. IEEE Int. Conf. MEMS*, pp. 479–482, IEEE, Las Vegas, NV, USA, doi:10.1109/MEMSYS.2002.984306.

Kim, J., P. Moin, and R. Moser (1987), Turbulence statistics in fully developed channel flow at low Reynolds number, *J . Fluid Mech*, *177*(-1), 133–166, doi:10.1017/S0022112087000892.

Koch, K., B. Bhushan, Y. C. Jung, and W. Barthlott (2009), Fabrication of artificial Lotus leaves and significance of hierarchical structure for superhydrophobicity and low adhesion, *Soft Matter*, *5*(7), 1386, doi:10.1039/b818940d.

Kota, A. K., G. Kwon, and A. Tuteja (2014), The design and applications of superomniphobic surfaces, *NPG Asia Materials*, *6*(6), e109, doi:10.1038/am.2014.34.

Lauga, E., and H. A. Stone (2003), Effective slip in pressure-driven Stokes flow, *Journal of Fluid Mechanics*, *489*(489), 55–77, doi:10.1017/S0022112003004695.

Lee, C., and C. J. Kim (2009), Maximizing the Giant Liquid Slip on Superhydrophobic Microstructures by Nanostructuring Their Sidewalls, *Langmuir*, *25*(21), 12,812–12,818, doi:10.1021/la901824d.

Lee, C., C. H. Choi, and C. J. Kim (2008), Structured surfaces for a giant liquid slip, *Physical Review Letters*, *101*(6), 64,501, doi:10.1103/PhysRevLett.101.064501.

Leonardi, S., and I. P. Castro (2010), Channel flow over large cube roughness: A direct numerical simulation study, *Journal of Fluid Mechanics*, *651*(1999), 519–539, doi:10.1017/S002211200999423X.

Leonardi, S., P. Orlandi, and R. A. Antonia (2007), Properties of d- and k-type roughness in a turbulent channel flow, *Physics of Fluids*, *19*(12), doi:10.1063/1.2821908.

Ling, H., S. Srinivasan, K. Golovin, G. H. McKinley, A. Tuteja, and J. Katz (2016), High-resolution velocity measurement in the inner part of turbulent boundary layers over super-hydrophobic surfaces, *Journal of Fluid Mechanics*, *801*, 670–703, doi:10.1017/jfm.2016.450.

Liu, Y., X. Chen, and J. H. Xin (2008), Hydrophobic duck feathers and their simulation on textile substrates for water repellent treatment, *Bioinspiration and Biomimetics*, *3*(4), 046,007, doi:10.1088/1748-3182/3/4/046007.

Ma, M., and R. M. Hill (2006), Superhydrophobic surfaces, doi:10.1016/j.cocis.2006.06.002.

Mabry, J. M., A. Vij, S. T. Iacono, and B. D. Viers (2008), Fluorinated polyhedral oligomeric silsesquioxanes (F-POSS), *Angewandte Chemie - International Edition*, *47*(22), 4137–4140, doi:10.1002/anie.200705355.

Mäkiharju, S. A., M. Perlin, and S. L. Ceccio (2012), On the energy economics of air lubrication drag reduction, *International Journal of Naval Architecture and Ocean Engineering*, *4*(4), 412–422, doi:10.3744/JNAOE.2012.4.4.412.

Mehta, R. D., and P. Bradshaw (1979), Design Rules for Small Low Speed Wind Tunnels, doi:10.1017/s0001924000031985.

Min, T., and J. Kim (2004), Effects of hydrophobic surface on skin-friction drag, *Physics of Fluids*, *16*(7), L55–L58, doi:10.1063/1.1755723.

Mockenhaupt, B., H. J. Ensikat, M. Spaeth, and W. Barthlott (2008), Superhydrophobicity of biological and technical surfaces under moisture condensation: Stability in relation to surface structure, *Langmuir*, *24*(23), 13,591–13,597, doi:10.1021/la802351h.

Monty, J. P. (2005), Developments in smooth wall turbulent duct flows, Book, University of Melbourne.

Morel, T. (1977), Design of Two-Dimensional Wind Tunnel Contractions, *Journal of Fluids Engineering*, pp. 371–377, doi:10.1115/1.3448764.

Nakajima, A., K. Hashimoto, and T. Watanabe (2001), Recent studies on super-hydrophobic films, in *Monatshefte fur Chemie*, vol. 132, pp. 31–41, doi:10.1007/s007060170142.

Navier, C. (1823), Memoire sur les lois du mouvement des fluides, *Mem Acad R Sci Paris.*, *6*, 389—-416.

Neinhuis, C., and W. Barthlott (1997), Characterization and distribution of water-repellent, self-cleaning plant surfaces, *Annals of Botany*, *79*(6), 667–677, doi:10.1006/anbo.1997.0400.

Neumann, D., and A. Kureck (2013), Composite structure of silken threads and a proteinaceous hydrogel which form the diving bell wall of the water spider Agyroneta aquatica, *SpringerPlus*, *2*(1), 223, doi:10.1186/2193-1801-2-223.

Nikuradse, J. (1933), Law of flow in rough pipes, *National Advisory Committee for Aeronautics - Technical Memorandums*, *NACA Techn*(Mem 1292), 62.

Onda, T., S. Shibuichi, N. Satoh, and K. Tsujii (1996), Super-Water-Repellent Fractal Surfaces, *Langmuir*, *12*(9), 2125–2127, doi:10.1021/la950418o.

Öner, D., and T. J. McCarthy (2000), Ultrahydrophobic surfaces. Effects of topography length scales on wettability, *Langmuir*, *16*(20), 7777–7782, doi:10.1021/la000598o.

Ou, J., and J. P. Rothstein (2005), Direct velocity measurements of the flow past drag-reducing ultrahydrophobic surfaces, *Physics of Fluids*, *17*(10), 103,606, doi:10.1063/1.2109867.

Ou, J., B. Perot, and J. P. Rothstein (2004), Laminar drag reduction in microchannels using ultrahydrophobic surfaces, *Physics of Fluids*, *16*(12), 4635–4643, doi:10.1063/1.1812011.

Park, H., G. Sun, and C.-J. Kim (2014), Superhydrophobic turbulent drag reduction as a function of surface grating parameters, *Journal of Fluid Mechanics*, *747*, 722–734, doi:10.1017/jfm.2014.151.

Peguero, C., and K. Breuer (2009), On Drag Reduction in Turbulent Channel Flow over Superhydrophobic Surfaces, in *Advances in Turbulence XII: Proceedings of the 12th EUROMECH European Turbulence Conference, Marburg, Germany*, edited by B. Eckhardt, pp. 233–236, Springer Berlin Heidelberg, Marburg, Germany, doi:10.1007/978-3-642-03085-757.

Perlin, M., and S. Ceccio (2014), *Mitigation of hydrodynamic resistance: Methods to reduce hydrodynamic drag*, xii, 152 pages pp., doi:10.1142/9789814612265.

Perlin, M., D. R. Dowling, and S. L. Ceccio (2016), Freeman Scholar Review: Passive and Active Skin-Friction Drag Reduction in Turbulent Boundary Layers, *Journal of Fluids Engineering*, *138*(9), 091,104, doi:10.1115/1.4033295.

Pope, S. B. (2000), *Turbulent Flows*, vol. 12, 2020–2021 pp., doi:10.1088/0957-0233/12/11/705.

Prince, J. F., D. Maynes, and J. Crockett (2014), Pressure Drop Measurements in Turbulent Channel Flow Over Superhydrophobic Surfaces With Riblets, doi:10.1115/ICNMM2014-21690.

Raffel, M., C. E. Willert, S. T. Wereley, and J. Kompenhans (2007), *Particle Image Velocimetry: A Practical Guide*, vol. 2nd, 448 pp., doi:10.1097/JTO.0b013e3182370e69.

Rothstein, J. P. (2010), Slip on Superhydrophobic Surfaces, *Annual Review of Fluid Mechanics*, *42*(1), 89–109, doi:10.1146/annurev-fluid-121108-145558.

Samaha, M. A., H. Vahedi Tafreshi, and M. Gad-el Hak (2011), Modeling drag reduction and meniscus stability of superhydrophobic surfaces comprised of random roughness, *Physics of Fluids*, *23*(1), 12,001, doi:10.1063/1.3537833.

Samaha, M. A., H. Vahedi Tafreshi, and M. Gad-el Hak (2012), Effects of hydrostatic pressure on the drag reduction of submerged aerogel-particle coatings, *Colloids and Surfaces A: Physicochemical and Engineering Aspects*, *399*, 62–70, doi: 10.1016/j.colsurfa.2012.02.025.

Schlichting, H., and K. Gersten (2003), *Boundary-Layer Theory*, Grenzschicht-Theorie.English, xxiii, 799 p. pp., Springer, New York, doi:10.1007/978-3-662-52919-5.

Schultz, M. P., and K. A. Flack (2007), The rough-wall turbulent boundary layer from the hydraulically smooth to the fully rough regime, *Journal of Fluid Mechanics*, *580*, 381–405, doi:10.1017/S0022112007005502.

Schultz, M. P., and K. A. Flack (2013), Reynolds-number scaling of turbulent channel flow, *Physics of Fluids*, *25*(2), doi:10.1063/1.4791606.

Seo, J., and A. Mani (2016), On the scaling of the slip velocity in turbulent flows over superhydrophobic surfaces, *Physics of Fluids*, *28*(2), 25,110, doi:10.1063/1.4941769.

Sovran, G., and E. Klomp (1967), Experimentally determined optimum geometries for rectilinear diffusers with rectangular, conical or annular cross-section, *Fluid mechanics of internal flow: Proceedings of the Symposium on the Fluid Mechanics of Internal Flow, General Motors Research Laboratories, Warren, Michigan, 1965*, *20*(21), 270–319.

Srinivasan, S., S. S. Chhatre, J. M. Mabry, R. E. Cohen, and G. H. McKinley (2011), Solution spraying of poly(methyl methacrylate) blends to fabricate microtextured, superoleophobic surfaces, *Polymer*, *52*(14), 3209–3218, doi: 10.1016/j.polymer.2011.05.008.

Srinivasan, S., W. Choi, K.-C. Park, S. S. Chhatre, R. E. Cohen, and G. H. McKinley (2013), Drag reduction for viscous laminar flow on spray-coated non-wetting surfaces, *Soft Matter*, *9*(24), 5691, doi:10.1039/c3sm50445j.

Srinivasan, S., S. S. Chhatre, J. O. Guardado, K.-C. Park, A. R. Parker, M. F. Rubner, G. H. McKinley, and R. E. Cohen (2014), Quantification of feather structure, wettability and resistance to liquid penetration, *Journal of The Royal Society Interface*, *11*(96), 20140,287–20140,287, doi:10.1098/rsif.2014.0287.

Srinivasan, S., J. A. Kleingartner, J. B. Gilbert, R. E. Cohen, A. J. Milne, and G. H. McKinley (2015), Sustainable drag reduction in turbulent Taylor-Couette flows by depositing sprayable superhydrophobic surfaces, *Physical Review Letters*, *114*(1), doi:10.1103/PhysRevLett.114.014501.

Tian, H., J. Zhang, E. Wang, Z. Yao, and N. Jiang (2015), Experimental investigation on drag reduction in turbulent boundary layer over superhydrophobic surface by TRPIV, *Theoretical and Applied Mechanics Letters*, *5*(1), 45–49, doi: 10.1016/j.taml.2015.01.003.

Truesdell, R., A. Mammoli, P. Vorobieff, F. Van Swol, and C. J. Brinker (2006), Drag reduction on a patterned superhydrophobic surface, *Physical Review Letters*, *97*(4), 44,504, doi:10.1103/PhysRevLett.97.044504.

Ünal, U. O., B. Ünal, and M. Atlar (2012), Turbulent boundary layer measurements over flat surfaces coated by nanostructured marine antifoulings, *Experiments in Fluids*, *52*(6), 1431–1448, doi:10.1007/s00348-012-1262-z.

Vajdi Hokmabad, B., and S. Ghaemi (2016), Turbulent flow over wetted and non-wetted superhydrophobic counterparts with random structure, *Physics of Fluids*, *28*(1), 15,112, doi:10.1063/1.4940325.

Watanabe, K., and H. Udagawa (2001), Drag reduction of non-Newtonian fluids in a circular pipe with a highly water-repellent wall, *AIChE Journal*, *47*(2), 256–262, doi:10.1002/aic.690470204.

Watanabe, K., Y. Udagawa, and H. Udagawa (1999), Drag reduction of Newtonian fluid in a circular pipe with a highly water-repellent wall, *Journal of Fluid Mechanics*, *381*(2), S0022112098003,747, doi:10.1017/S0022112098003747.

Wenzel, R. N. (1936), Resistance of solid surfaces to wetting by water, *Industrial and Engineering Chemistry*, *28*(8), 988–994, doi:10.1021/ie50320a024.

White, F. (2006), *Viscous fluid flow*, 3rd ed., McGraw-Hill Higher Education, New York, NY.

Woolford, B., J. Prince, D. Maynes, and B. W. Webb (2009), Particle image velocimetry characterization of turbulent channel flow with rib patterned superhydrophobic walls, *Physics of Fluids*, *21*(8), 5106, doi:10.1063/1.3213607.

Xie, Z., and I. P. Castro (2006), LES and RANS for turbulent flow over arrays of wall-mounted obstacles, *Flow, Turbulence and Combustion*, *76*(3), 291–312, doi:10.1007/s10494-006-9018-6.

Xie, Z. T., O. Coceal, and I. P. Castro (2008), Large-Eddy simulation of flows over random urban-like obstacles, *Boundary-Layer Meteorology*, *129*(1), 1–23, doi:10.1007/s10546-008-9290-1.

Yang, J., Z. Zhang, X. Xu, X. Men, X. Zhu, and X. Zhou (2011), Superoleophobic textured aluminum surfaces, *New Journal of Chemistry*, *35*(11), 2422, doi:10.1039/c1nj20401g.

Young, T. (1805), An Essay on the Cohesion of Fluids, *Philosophical Transactions of the Royal Society of London*, *95*(0), 65–87, doi:10.1098/rstl.1805.0005.

Zanoun, E. S., H. M. Nagib, and F. Durst (2009), Refined cf relation for turbulent channels and consequences for high Re experiments, *Fluid Dynamics Research*, *41*(2), 021,405, doi:10.1088/0169-5983/41/2/021405.

Zhang, J., H. Tian, Z. Yao, P. Hao, and N. Jiang (2015), Mechanisms of drag reduction of superhydrophobic surfaces in a turbulent boundary layer flow, *Experiments in Fluids*, *56*(9), 1–13, doi:10.1007/s00348-015-2047-y.

Zhao, J. P., X. D. Du, and X. H. Shi (2007), Experimental research on friction-reduction with super-hydrophobic surfaces, *Journal of Marine Science and Application*, *6*(3), 58–61, doi:10.1007/s11804-007-7007-3.